Electroproduction of η Mesons in the $S_{11}(1535)$ Resonance Region at High Momentum Transfer

Mark Macrae Dalton

A thesis submitted to the Faculty of Science,
University of the Witwatersrand, Johannesburg,
in fulfillment of the requirments for the
degree of Doctor of Philosophy.

Johannesburg, 2008

Candidate's Declaration

I declare that this thesis is my own, unaided work. It is being submitted for the degree of Doctor of Philosophy in the University of the Witwatersrand, Johannesburg. It has not been submitted before for any degree or examination at any other University.

____

Mark Dalton (candidate)

________________ day of ________________ 2008

Abstract

The differential cross-section for the exclusive process $p(e,e'p)\eta$ has been measured at $Q^2 \sim 5.7$ and 7.0 (GeV/c)^2, which represents the highest momentum transfer measurement of this to date, significantly higher than the previous highest at $Q^2 \sim 3.6$ (GeV/c)^2. Data was taken for centre-of-mass energies from threshold to ~1.8 GeV, encompassing the $S_{11}(1535)$ resonance, which dominates the $p\eta$ channel. The total cross section is obtained, from which is extracted the helicity-conserving transition amplitude $A_{1/2}$, for the production of the $S_{11}(1535)$ resonance. This quantity appears to begin scaling as Q^{-3}, a predicted signal of the dominance of perturbative QCD, within the Q^2 range of this measurement. No currently available theoretical predictions can account for the behaviour of this quantity over the full measured range of Q^2.

Acknowledgments

I must firstly acknowledge my mother, Carol Saunders. She has contributed more to my life and specifically my education than any other person. Her strong sense of principle and incredible work ethic are inspiring and have helped shape my views. I will probably never know how much she sacrificed for us. Thank you, mom. Thanks go to my father, David, for all that he has done for me. My younger brother, Grant, is a good man and friend to me, and has a fresh perspective. He is the driving force behind keeping our relationship strong and I appreciate all his efforts. I have come to learn so much from him.

My special thanks go to my cousin and PhD advisor, Simon Connell. For as long as I can remember he has spoken of the virtues and beauty of physics and science in general, and the amazing technologies used to study them, and in me he found someone eager to listen. It is primarily because of him that I have embarked upon a career in physics. It was also him that reminded me of the importance and fun of what I was doing, when as an undergraduate, I became disillusioned with the difficulty of physics and the dryness with which it was sometimes taught. If I have a fraction of his passion, I will be well set for a rewarding life path.

I must express much appreciation to Geraldine Connell, Bridgette, Raymond and again to Simon for being such good family and making me feel so

welcome at all times. Especially after my mom moved to Australia, theirs became my second home. I cannot express how much this has meant to me. I have so much other family who are very important to me. They have all contributed to my development and growth and have really fostered a sense of belonging in me: Iain, Aidee, Andrew and Rob; Merle; Lynn, Carol and Heather; Julia, Debbie, Theresa and Angela; my grandmother Bea; Frankie and Tony; Martin, Terry and Gabbi; Lucy, Paul, Johnnie and Ruthie; Rosie, Pete, Paul and Julie; Andy, Anne, Tara, William and Vincent; Luke, Liz, Hannah, Matthew and Nick; and other Nick.

As an undergraduate, I spent a lot of time at the then Schonland Research Centre. This facility had the most wonderful atmosphere where students, even young ones, were made to feel very welcome and part of the research enterprise. I did three summer internships there and had a great time, learning plenty, and most importantly becoming more enthused to continue with my studies. People who contributed generally to the place were Mike Butler, Richard Chirwa, Cynthia Dawood, Trevor Derry, Bryan Doyle, Johan Geyer, Cynthia Hlatshwayo, Roger Hart, Charlie Levitt, Ryan Maclear, Doris Monyamane, Agnes Mthembu, Mervin Naidoo, Tom Nam, Oleg Pekar, Mik Rebak, Eric Rood, Elias Sideras-Haddad, Balt Verhagen and John Watterson. Specifically significant for me there were Freidel Sellschop, Simon Connell and Roger Nilen. A victim of chronic underfunding, and ultimately taken over as a national lab, in my opinion the new entity is sterile and not a patch on the old.

Later I was privileged to discover the Jefferson Lab. This place too has a lovely atmosphere, just on a much larger scale. The people I have met there have been friendly and encouraging and the environment is collegiate. The Lab is an amazing facility and I must acknowledge the many people and funding agencies who built it up to what it is today and who keep it progressing. None of this science would be possible without their efforts.

My sincere thanks go to Peter Bosted, who is my other PhD advisor. His willingness to correspond with me on a daily basis, tirelessly review my work and suggest improvements, and to put up with my ignorance when I was still developing as a graduate student and finding my feet, is greatly appreciated. He is an amazing physicist and would regularly astound me with the depth of his knowledge and insight. Mark Jones deserves a special mention. It is him that I felt most comfortable asking potentially stupid questions, and there must have been many of those over the years. Thanks to Anthony Villano for being my companion, as the other PhD student on this experiment, and for being ready to help me with my analysis.

In the day-to-day analysis of the data, I received a huge amount of help from these people, the “core collaboration”, consisting of Peter Bosted, Simon Connell, Mark Jones, Paul Stoler and Anthony Villano. In the weekly telephone conferences, held for many years at 08:45 EST every Tuesday morning, any results or progress that had been made was presented to the group, via the Internet and the phone. These were discussed at length and many suggestions, checks and cross checks and pearls of wisdom were forthcoming from the group. It was here that I learned legions of lessons including the necessity of communicating results using a well conceptualised figure. I also learned to become quite adept at calculating time zones, factoring in daylight saving time, and determining what time in our South African afternoon the meeting was to start. :-)

Rolf Ent was my first contact at Jefferson Lab, and when I arrived, by myself and knowing no one, he greeted me with a smile and made me feel welcome from the word go. Eric Christy, Dave Gaskel, Thea Keppel, Gabriel

and Ioana Niculescu, Sarah Phillips, Greg Smith, Steve Wood, and a whole host of others helped to make my almost 8 months (in four trips) at the Lab both enjoyable and productive. A special mention goes to Claire Lee, my friend from our group. She did the pilgrimage to Jefferson with me twice. Her sense of fun and humour have been greatly appreciated over the years.

The experiment was conceived of and proposed while I was still an undergraduate student, and I only joined when the data was taken. Thanks to all those involved in that process. I would like to acknowledge the coauthors on the paper who are listed in Appendix A, who contributed to the successful running of the experiment. For the seven weeks that this experiment took data, it was required that three people were on shift in the Hall C "counting house" at all times. At 9 shifts a day, this is a total of about 450 eight-hour shifts that had to be done, night and day. These people were responsible for taking the data, starting and stopping runs and changing the spectrometer configurations, making sure that the detector and electronics were working and that the data looked reasonable, making sure that the cryogenic target remained within safe parameters and didn't explode, and keeping detailed logs of everything for the later analysis.

The analysis in the subsections titled Coincident Elastic Scattering Cross-Section and Inclusive Elastic and Inelastic Cross-Section, both in Section 3.4.5, were done by Mark Jones and Peter Bosted respectively. The text in these sections are summaries of unpublished reports by them, produced as part of the effort to analyse the exclusive inelastic data.

Thanks to John Arrington, Henk Blok, Tanja Horn, Garth Huber and Mark Paris who reviewed Chapter 3 and gave corrections and comments. John especially went above and beyond the call of duty here and inspired great improvements.

I would like to thank all those who have been members of our group while I have been around. They have contributed to the general atmosphere: George Amolo, Jupiter Chinyadza, Denson Dube, Dumisani Gxawu, Thulani Jili, Ian Korir, Claire Lee, Morgan Madhuku, Welheminah Mampe, Georgie Mbianda Njencheu, Amino Naran, Marothi Phoku, Rhyme Setshedi, Winile Sibande, Tjatji Tjebane and Doom-null Unwuchola. Specific acknowledgment goes to Sergio Ballestrero, who has become my friend over the past 3 years, and from whom I have learned much, specifically in the areas of computing and data analysis. He is particularly skilled in these areas and is a fantastic resource for the group and me personally. I would also like to thank him for giving me the opportunity to work on his project after my PhD, while I figure out what specific direction I would like to go in.

A very special thanks goes to Robert de Mello Koch. He is the most fantastic teacher, amazingly smart man and developed thinker. After being taught by him in my fourth year, I sought out and attended as much of his teaching as I could. Later we became friends and since then he has regularly taken me for coffee and a chat. We'd talk about life, love, politics and physics. He delights in telling people about his work which is always very exciting and which somehow he manages to make seem understandable. As a graduate student, when I was struggling with things, it was often Robert who helped to re-enthuse me with his passion, and he has made a lasting contribution to my self esteem.

I have the privilege to have many wonderful friends. An exhaustive list here would be prohibitively long and to mention only a few would be unfair. I would prefer to acknowledge them more privately, with a beer perhaps.

I have to give a grudging acknowledgment to the South African National Research Foundation (NRF) for funding me through their Grantholder Bursary scheme. When I first started, this was a paltry R 22,000 (roughly 3,000 US$) per anum. Now it is R 35,000 p/a, not enough to survive on by itself, but nevertheless without which I wouldn't have been able to survive. I would like to thank Simon for creating an environment in which students could earn extra money by assuming responsibility for laboratory equipment and services. In my case this was looking after the servers and other computing infrastructure, through which I learned many valuable skills. My trips overseas were paid for in part by the NRF Mobility Grant and by Simon's NRF Research Grant. My local expenses at Jefferson Lab were paid by Jefferson Lab's Hall-C.

Contents

List of Figures

List of Tables

Chapter 1

Introduction

1.1 Hadrons and Quantum Chromodynamics

Protons and neutrons are composed of lightweight, pointlike quarks and gluons. These constituents possess the “colour” charge and are described by the fundamental theory known as quantum chromodynamics (QCD). The colour charge is the source of the strong force, which not only binds the quarks and gluons into nucleons, but also binds nucleons together to form nuclei. A major goal of nuclear physics is to understand the structure and properties of nucleons in terms of the quarks and gluons and QCD.

The best understood process in nature, the electroweak interaction, is described by a quantum field theory (QFT) called quantum electrodynamics (QED). QCD is also a quantum field theory, but fundamental differences between the two leave QCD being much less well understood. In general, QFT’s cannot be solved, but by virtue of its small coupling strength QED is very amenable to approximation by perturbative techniques. On the other hand, QCD mostly has a strong coupling strength and so perturbative methods only work at very high energies, where the coupling strength is weak.

Unlike in QED, the basic constituents of QCD (the quarks and gluons), cannot appear in isolation. They are *confined* to within colour-neutral hadrons, including the nucleon, in a way that is only understood qualitatively. Essentially, it is the exceedingly strong interaction between these basic building blocks that binds them, causing them to lose their identities and the system to exhibit hadronic degrees of freedom.

At small distance scales, accessed with high energy probes, the quarks and gluons act as almost free particles. This is the regime of perturbative QCD (pQCD), where the coupling is small, and solutions can be found. Understanding the *transition* from the non-perturbative regime of long distance scales, strong interaction and hadron effective degrees of freedom to the perturbative regime of short distance scales, free quarks and QCD degrees of freedom is important for understanding the non-perturbative regime itself and the nature of confinement.

1.2 Research Methodologies

Various techniques in both theory and experiment are being used to make progress in our understanding of nucleonic structure. On the theoretical front, these include numerical (as opposed to analytical) solutions of QCD, effective field theories and models that invoke symmetries of QCD, and sophisticated aspects of perturbative QCD such as generalised parton distributions (GPDs). More detail is given to these endeavours in Sec. 2.2.4.

On the experimental side, the strategy is to make as many different measurements as possible. Using different probes, targets, and polarisations of both, different energy scales, higher precision, all with a view to testing the available models, exposing their weaknesses and choosing between them or providing data in previously unmeasured terrain. The process of developing our intuition is a slow one.

Much progress is being made with electron scattering on nuclear targets, and the measurement described in this thesis uses electrons as a probe. An electron, or any other charged lepton for that matter, interacts with the nucleus through the electro-weak interaction, which is well understood in QED. The interaction is very weak, allowing the electron to probe the entire target. The scattering mechanism, since it is well understood, can be cleanly separated from the structure of the target. This is especially true since, to a very good approximation (Born approximation), the interaction is mediated by a single force-carrying virtual photon.

What is actually probed by the scattering depends on kinematics and the target. For a proton target, the virtual photon may interact with the struck proton as a whole, either scattering elastically (conserving energy and momentum with the entire nucleon), or exciting the proton into a baryon resonance. As the energy and momentum increase, the "size" of the virtual photon shrinks, increasing the the resolution and making it more likely to probe the quark degrees of freedom. At high enough momentum transfer, the interaction is primarily scattering from an almost free quark.

1.3 The Experimental Measurement of the Thesis

The experiment "E01-002: Baryon Resonance Electroproduction at High Momentum Transfer" was run at Thomas Jefferson National Accelerator Facility (Jefferson Lab) from 29 April until 18 June 2003. An electron beam of 5.5 GeV was incident on a liquid hydrogen (proton) target. In the case of this experiment, the kinematics are chosen in order to excite the proton into the $S_{11}(1535)$ resonance at the highest momentum transfer possible with the equipment available. The resonance was identified and studied through its decay into a proton and η meson. In a similar data set, taken concurrently, the analysis of which is available in Ref. [1], the $\Delta(1232)$ resonance was created and detected as a decay into a proton and π_0.

These data are in a regime where no such measurement has been done before, at a momentum transfer high enough to possibly be in the realm of pQCD, certainly well within the region of transition to there. As such they are of great significance, as will be shown in the course of this thesis, in that they comment on our understanding of QCD through theoretical models inspired by QCD.

1.4 The Structure of the Thesis

This thesis is written around a long paper which has been submitted for publication in the journal Physical Review C (**Phys. Rev. C**), published by the American Physical Society. The paper itself is the heart of the thesis. Although it is long and detailed, it assumes familiarity with much that is happening in nuclear physics at the moment. This thesis then contextualises that work, and discusses the relevance and impact within the broader context.

Chapter 2 is an extended review of the field of nuclear physics paying particular attention to studies of nucleon structure. The aim of this chapter is to set the scene for the detailed treatment that is given to the specific measurement concerning this thesis in Chapter 3. The flow of Chapter 2 proceeds from the general to the specific, all the while contextualising the results that are presented later. The status of the field of nuclear science is briefly reviewed. From there, the focus moves to examining the structure of the nucleon, covering form factors, the excited state structure of nucleons and finally realm of hard scattering. The last part of the review is a more pedagogic treatment of the formalism that is briefly covered in Chapter 3.

Chapter 3 is the reproduction of the long, stand-alone paper, published with the author of this thesis as lead author, as an electronic preprint (arxiv:0804.3509 [hep-ex]) and in Phys. Rev. C. As is typical in this field of physics, there are many collaborators on this experiment, listed in Appendix A. The author of the thesis drafted the paper and managed the review process by the group. This chapter describes the necessary theory for understanding the problem and extracting meaningful results from the data. The experimental method and apparatus are given brief treatment along with comprehensive references to more detailed material. Extensive coverage is given to the data analysis and extraction of the differential cross section for η-electroproduction and the helicity amplitude for the production of the $S_{11}(1535)$ resonance.

It will be seen in Section 3.4 that the process of analysing the data, and especially minimising and quantifying the uncertainty in the results, is a long and technically demanding one. The author of the thesis was intimately involved in this process from the initial running of the experiment. Starting during the experiment itself the data was analysed continuously, in a preliminary fashion, to ensure that it was being acquired according to expectations. The experiment produced about 1.1 terabytes of data, consisting of about 2,800 raw signals (read out from the ADC and TDC electronics) for each triggered event, which was saved onto tape in the Jefferson Lab computer centre. This data was “replayed” numerous times in the early post-experimental analysis, and physics quantities calculated, until the calibrations were perfected. The data set had then been reduced to just more than 12 gigabytes of ntuples with 62 records per event.

From this point, the analysis was completed almost exclusively by the author of this thesis, the general idea to extract meaningful results by comparing the signals from the incredibly complicated detector configuration to an accurate Monte Carlo computer simulation of the detectors. Much effort was made to treat the major source of background, caused by interference from multiple pion production. These processes have not been measured at this high Q^2 and so had to be extrapolated using models. Several algorithms for removing the background were studied for integrity, reliability and stability. A model of the expected signal was created as input to the simulation and improved through an iterative procedure. The influence of possible systematic uncertainties were rigorously studied. These include uncertainties in the detector acceptances, trigger and detection efficiencies, the effect of the cuts, offsets and resolution, the measurement of target density and total charge and in the modelling of the multi-pion background

Section 3.5 details the fitting of the extracted cross-section to obtain angular parameters to compare with models. This fitting procedure was also done to the previous data to aid in comparison. The total cross-section was determined and fitted with a relativistic Breit-Wigner function to extract the helicity amplitude for the production of the S_{11} resonance. Trends in the Q^2 evolution of the angular dependence of the differential cross-section and in the magnitude of the helicity amplitude are identified and discussed. Comparison is made with previous data, which falls in a different kinematics, and with a broad section of theoretical models from the literature.

Chapter 4 is an extensive discussion on the new work presented in Chapter 3. This chapter pays particular attention to the analysis that the data will be put through by other groups. This chapter goes on to discuss the extension to this experiment that will be possible with the JLab 12 GeV upgrade.

Chapter 5 brings the thesis to a conclusion with a brief summary, followed by the appendices and bibliography. The collaborators on the experiment are listed in Appendix A. A publication list for the author of the thesis in Appendix B. Finally, the raw results of the experiment, the extracted differential cross sections for η-electroproduction are listed in Appendix C.

Chapter 2

Contextual Review

This chapter is intended to provide the background necessary to understand the central part of this thesis presented in Chapter 3. Both the requisite science for understanding the work and context within which it is a contribution to the field will be discussed.

2.1 The Breadth of Nuclear Physics

It is perhaps valuable to briefly discuss the status of nuclear physics as a whole and locate the specific quest to understand nucleon structure within that. Nuclear science is, of course, a very broad endeavor, with an already well established capacity for providing insights into and applications in our world. Nuclear physics overlaps with other sciences—for example, understanding the Big Bang and how matter emerged in the first moments of the universe requires an interplay of nuclear physics, high-energy physics and astrophysics. Explaining the nature of supernovae and the origin of elements in the cosmos are other examples. Nuclei can be used as laboratories to study the fundamental forces.

The impact and applications of nuclear science are felt in every aspect of our daily lives, from medical diagnostics and treatment, where radioisotopes, diagnostic imaging, and cancer radiation therapy are prime examples, to the detection of explosives using neutron scattering. Energy production, many and varied analytical techniques, environmental science, space exploration, and materials analysis and modification are all beneficiaries of knowledge from this field.

The endeavour of nuclear physics today can be divided into five main areas of activity, as suggested by Ref. [2], from which much of this section is inspired. The interested reader is advised to consult that for a more detailed review. These five areas cover fields of study from the structure of partons in the nucleon and nucleons in the nucleus to the nuclear physics of the Big Bang, the origin of the elements and the role of nuclear physics in understanding the fundamental forces of nature. A brief account of all five is presented here to help appraise the reader of the status and recent movement of the field as a whole.

2.1.1 The Structure of the Nucleon

As mentioned in the introduction, proton and neutrons are known to have internal structure which is described by QCD, but must still be adequately connected to the observed properties of the nucleons. The work in this thesis in primarily concerned with this problem, and the topic will be dealt with in greater depth in Sec. 2.2.

2.1.2 The Structure of Nucleonic Matter

The goal of nuclear structure physics is to obtain quantitative description of all nuclei within a single theoretical framework, a unified microscopic description. The structure and stability of nuclei changes significantly with proton and neutron number, excitation energy, angular momentum, and density. There are wide ranges of energy and momentum scales between the nuclei themselves, and correlations between nucleons that show single-particle and collective mode (such as rotation and vibration) behaviours. Such a theory would predict this variety. Another challenge is understanding how the traditional description of the nucleus as a system of nucleons and associated currents, relates to the fundamental theory of strong interactions, QCD. These goals are a long way off, and will require major theoretical advances and major new facilities.

Much progress is being made by studying exotic nuclei, where the ratio of protons to neutrons is very different from that in stable nuclei. These nuclei seem to demonstrate a shell structure different from stable nuclei. A new type of nucleon pairing and a new decay mode have been seen in these systems. Eventually we will establish the limits of nuclear existence, determining what combinations of protons and neutrons can exist, and what their properties are. This is important for studies of the origin of the elements from reactions in supernovae which traverse unknown regions of the nuclear chart, as well as other astrophysical processes.

Other exciting results abound, including observations of new collective modes, new super-deformed nuclei and new superheavy elements. Very heavy nuclei are seen to sustain unexpectedly rapid rotation. Nuclear phase change appears to occur, with sudden changes in mass between spherical and deformed systems, and evidence for liquid and gaseous forms of nuclear matter. Remarkable agreement can now be shown, for properties of light nuclei, between experimental measurements and numerical solutions of a free nucleon-nucleon interaction with a three-body force - although various approximations must still be invoked in describing heavy nuclei because of their inherent complexity.

Nuclei can also act as laboratories for other studies, such as studying the weak interaction and other fundamental aspects of nature (see Sec. 2.1.5). Nuclei may also act as analogues for other systems, such as studying the transition from order to chaos by analysing nuclei with increasing excitation energy, or the study of weakly bound quantum systems through the study of very neutron rich nuclei.

2.1.3 The Properties of Hot Nuclear Matter

The QCD “vacuum”, the configuration of free space in the absence of any colour charges, is a quark-gluon condensate. At low energies, particles are believed to acquire their mass through their interaction with the vacuum, breaking chiral symmetry in the process. This is how three ∼MeV bare quarks produce a ∼GeV proton. Collisions of relativistic heavy ions may allow us to observe the effects of the vacuum directly by creating a plasma of unbound quarks and gluons, which is equivalent to a very hot vacuum. Lattice QCD calculations suggest that at temperatures exceeding 1 GeV fm^{-3}, the vacuum will melt and QCD chiral symmetry will be restored. As temperature and/or pressure increase, it is expected that a phase change will occur in QCD. In fact, there are two possible phase changes which may not occur under the same conditions. Deconfinement, where the quarks and gluons are no longer bound as constituents of hadrons, and chiral symmetry restoration, in which the quarks are reduced to their bare masses.

The Relativistic Heavy Ion Collider (RHIC) at Brookhaven National Lab, with the ability to collide beams of nuclei up to $Au + Au$, with centre-of-mass energies (c.m.) of 200 GeV per nucleon pair, is the premier facility for doing this type of physics. Since experiments started there in 2000, a number of fundamental new discoveries have been made.

Firstly, within the medium created in the collision there is enormous collective motion, consistent with hydrodynamic behavior of almost zero viscosity. This implies a very fast thermalisation within the collision with very strong interactions and “perfect liquid” behaviour. Additionally, the particle composition is consistent with chemical equilibrium among the hadrons. Secondly, there is jet “quenching” in the dense matter. Jets are very high transverse momentum events, well described by pQCD, which appear to be reabsorbed in the collision medium. These data implies that the collision reaches densities up to 100 times cold nuclear matter and 15 times the critical density from lattice calculations. Thirdly, an anomalous overproduction of baryons relative to mesons has been observed. This is understood as evidence for hadron formation through constituent quark coalescence, since there is scaling of yields and collective motion with the number of valence quarks. Lastly, there are indications of possible gluon saturation in heavy nuclei, signalled by relatively low multiplicities in $Au + Au$ collisions and suppressed particle production in $d + Au$ collisions. This is not conclusive though, and multiple scattering, factorisation breaking, shadowing, parton recombination, and incident parton energy loss are all proposed as explanations for these effects.

Once the Large Hadron Collider (LHC) at the European Organisation for Nuclear Research (CERN) is complete, with up to 14 TeV of energy per nucleon pair in a collision, the focus of these kinds of experiments will move there.

2.1.4 The Nuclear Part of Astrophysics

The knowledge and understanding of nuclear physics phenomena has a fundamental role to play in the field of astrophysics. The wealth of new astrophysical data that is becoming available from ground and satellite based observatories, and will continue to do so, involve fundamental nuclear physics issues that must be studied in the laboratory. The true potential of new instruments will only be realised when the underlying nuclear process are understood.

Recently, beams of radioactive and stable nuclei have allowed direct measurement of key astrophysical nuclear reactions, including those driving enormous explosions in binary systems, the capture of an α particle by ^{12}C which is important in the evolution of massive stars and the capture of a proton by ^{7}Be, important in the core of the sun. The problem of missing solar neutrinos has been solved, Sec. 2.1.5 has more details. Measurement of the fusion rates of neutrons with heavy elements has shown that some meteorites originated in red giants.

In spite of these successes, much more nuclear physics properties remain to be learned before we gain a full understanding of astrophysics issues such as the origin of the elements; the structure and cooling of neutron stars; the origin, propagation, and interactions of the highest-energy cosmic radiation; the mechanism responsible for the collapse and explosion of stars (supernovae); and the search for the origin of galactic and extragalactic gamma-ray sources.

2.1.5 Physics Beyond the Standard Model

The aim of this area of physics is to determine a single framework describing all the forces of nature. Despite its enormous success in describing the electroweak and strong forces, it is known that our current Standard Model (SM) of particle physics is incomplete. The Standard Model predicts, and for a long time it was thought that, neutrinos are massless. The discovery that solar neutrinos change their flavour during their journey to the earth showed that in fact neutrinos do have mass, and that the neutrinos together have as much mass as all the visible mass in the universe, the stars. Since the Standard Model provides no mechanism for neutrino mass, it must be modified.

Even prior to the neutrino oscillation results, the Standard Model was already known to have a number of weaknesses. It fails to adequately explain the huge variation in particle masses (from the neutrinos at scales of eV to heavy quarks at 10^{11} eV), the symmetry breaking of the weak interaction, why the electric charge is quantised, and why our universe is matter dominated. This is not even to mention that gravity is completely absent from the theory.

The search for a "new" Standard Model is characterised by very precise measurements, because most theories for a new standard model will predict only very small differences to the current model. Measurements of the energy dependence of the weak mixing angle θ_W, the degree of mixing between the Z^0 boson and the photon, are now being done through parity violating e^-e^- and e^-p scattering. Deviations from the standard model prediction here could signal the presence of much heavier neutral bosons in an extended standard model.

The precision measurement of the magnetic moment of the muon shows that it differs from the standard model prediction by 1.5σ. This result places stringent constraints on the possible contributions of supersymmetric particles in a new Standard Model. Cosmologists have an interest here as the neutralino is a possible dark matter candidate. The appearance that the CKM quark mixing matrix might not be unitary, by more than 2σ, may imply the existence of a right-handed, charged guage boson, or virtual, supersymmetric particles amongst others. Finding a violation of lepton family number (L), baryon number (B) or time-reversal invariance (T) will give insight into the new standard model. A substantial neutron electric dipole moment (EDM) would imply violation of T in the light quark sector (violation of T is seen heavy quarks in kaon and B decays). Many other experiments, including measuring the long-distance component of the parity-violating NN interaction, the asymmetry in $n + p \rightarrow d + \gamma$, and a large amount of work with neutrinos are being done to test the boundaries of the Standard Model.

Careful, energy-dependent studies of oscillations in solar and atmospheric neutrinos are being done to measure neutrino mass differences and mixing angles. Precise measurement of the $\pi^+ \rightarrow \mu^+ + \nu_\mu$ and $^3H \rightarrow ^3He + e^- + \nu_e$ reactions is being done to directly measure the masses of the muon neutrino and electron anti-neutrino. Many sophisticated searches for neutrino-less double beta decay are taking place to test for the existence of a Majorana mass for the neutrino. This would be an important violation of the Standard Model with theoretical implications from matter-antimatter asymmetry to physics of the highest energy scales imaginable (10^{12} TeV) through the "see-saw mechanism."

The Higgs boson is a massive scalar elementary particle, needed by the SM to explain how elementary particles acquire mass. It has not yet been observed, presumably because it is too massive, expected to be more than 100 GeV. Supersymmetry (SUSY) is one of the leading candidates for the extension of the Standard Model. This theory postulates that bosons and fermions are equivalent, meaning that every particle we observe has a superpartner whose spin differs by $\frac{1}{2}$. This may be needed in order to combine quantum field theory with general relativity to get a unified theory expected to be valid at the Planck length 10^{-33} cm. SUSY may also be needed to explain why the Higgs mass is so light. The inclusion of the extra particles helps remove the mathematical inconsistencies, meaningless infinities, and negative probabilities that otherwise plague unification attempts.

The Tevatron at Fermilab, with collision energy of 2 TeV, is currently searching both for the Higgs boson and SUSY particles, although it is possible that this energy is too low to produce and detect these particles. The job will soon be taken up by the ATLAS and CMS experiments at CERN's LHC where a normal SM Higgs mass will be measurable with a precision of 0.1% up to masses of some 400 GeV. If SUSY exists at the electroweak scale, the LHC will discover it easily. As measurements along all of these avenues, and a host of others too numerous to mention, become more precise, the limits on possible new Standard Model physics become tighter.

2.2 Focussing on the Structure of the Nucleon

Following the broad, but rather brief overview of nuclear physics from the previous section, this section delves more deeply into the first of the five main areas of activity in nuclear physics, and the one relevant for this thesis, that of nucleon structure. This section draws on the following extensive references: the Whitepaper From DNP Town Meeting On Hadronic Physics [3], which is a recent of review of the status of field of hadronic physics; the review by Krusche and Schadmand [4] of baryon resonance study by meson photoproduction; and the review by Burkert and Lee [5] of baryon resonance study by meson electroproduction.

2.2.1 Overview

The proton is made up of fundamental, point-like constituents called partons. These are the *valence quarks* which determine the quantum numbers of the hadron, a sea of *virtual quark and anti-quark pairs* and the *gluons.* The challenge is to find out what the individual role of each of these constituents is in determining the structure of the nucleon.

It is clear that the gluons, and therefore the strong interaction regime, are vital to understanding the properties of nucleons. It is not certain how the constituents conspire to give the proton it's $\frac{1}{2}$ spin. For more than two decades we have known it is not all from the quark spins [6]. Numerical solutions of lattice QCD [7] and experiment [8] seem to agree that less than about 40% of the nucleon's spin is carried by the helicity of u and d quarks. It now appears that the missing spin is actually carried as orbital angular momentum, primarily by up and anti-up quarks [9]. Approximately half of a nucleon's mass and half of its momentum are due to the gluons, rather than the quarks. The largest uncertainty in parton distributions is in the distribution of the gluons.

Data from Fermilab [10] show that there is an asymmetry between the number of $\bar{u}$ and $\bar{d}$ quarks. If these particles came only from $q\bar{q}$ pairs in the sea, then they would be symmetrical, but this result suggests that the π^+-neutron Fock state of the proton is an important component. This has always been suggested by hadronic models of the nucleus, and now it is clear in the quark picture too. It shows that the anti-quark distributions need to be understood in the strong interaction regime.

Still other interesting new facets have come to light recently. There is an unexpected depletion of charge near the proton center. It is now clear that charge and current do not have the same distributions with the proton.

This has emerged from recent polarisation transfer measurements, described in more detail in Sec 2.3.1.

The objects that QCD describes are characterised by two regimes. At long distance scales there are the hadronic degrees of freedom. The baryons and mesons are surely the most natural basis in which to think about this regime. The fundamental QCD degrees of freedom, the quarks and gluons, are at this scale obscured by the complexity of their interactions. At short distance scales, the quark and gluon interactions become weaker, so that a perturbative approximation to the full QCD describes the data—only the most basic Feynman processes occur.

As was mentioned in the introduction, studying the transition from the hadronic degrees of freedom to the elementary quark and gluon degrees of freedom is an important part of finally getting a first-principles understanding of hadrons. A complete description must include both extremes of length scale. The data presented in Chapter 3 is taken in this transition region.

2.2.2 Short Distance Scales

Quark and gluon distributions within the nucleon are primarily studied with hard scattering, where the scattering is of a high enough energy that it probes the constituents without much dressing around them. This might occur when a high energy electron, muon or neutrino scatters off one of the partons within the nucleon. Hard scattering may also occur in the Drell-Yan process of hadron-hadron scattering, such as would occur at RHIC, where an anti-quark in one hadron annihilates with a quark in the other producing lepton pairs at high relative energy.

An important part of understanding the nucleon is measuring and explaining the parton distribution functions (PDF). Much of the work here is done in the spin sector, both in the longitudinal and transverse directions. Experimental results are being produced worldwide in numerous systems. Large transverse spin asymmetries measured in polarised pp [11] and in deep inelastic scattering (DIS) [12], are stimulating theoretical developments in transverse distributions structure, as they may allow us to probe parton orbital angular momenta and spatial distributions, transversity, correlations of quarks and gluons, and the color Lorentz force [13]. Comparing the transverse and longitudinal quark distributions gives a measure of the relativistic motion of quarks in the nucleon [14]. Measuring the Sivers [15] functions, which contribute with opposite signs in DIS and Drell-Yan, may help illuminate role of parton orbital angular momentum, and the Collins [16] asymmetries will give access to transversity distributions.

Complementary to spin measurements from DIS, gluon polarisation and determination of the flavor structure of the quark polarisation, are possible at RHIC with polarised proton-proton collisions. The first results show that for the glue, large positive polarisations are excluded and large negative polarisations are disfavored.

2.2.3 Long Distance Scales

Information on the charge and current distributions in the nucleon are obtained with elastic scattering. When combined with data of parity violation from the neutral weak current scattering, the individual quark flavour contributions can be extracted.

At long distance scales, our understanding of the nucleon is more related to effective constituent quarks than to the fundamental quark constituents of QCD. These constituent quarks and mesons appear to hide the complicated, strong effects of low energy valence quarks, sea quarks, and gluons in a massive, structured object with simple quantum numbers obeying the flavour symmetries of QCD. The relevant effective degrees-of-freedom for this picture must be identified, within the framework of constituent quark models of baryons. They will need to reflect the internal symmetries of the underlying fundamental interaction.

Typically a constituent quark model consists of three equivalent massive, extended constituent quarks located within a confining potential, interacting with each other via a short range residual interaction. This fine structure gives the spin-spin and spin orbit terms. There are however huge variations on this basic theme. For example, models which have a quark-diquark interaction [17], schematically shown in Fig. 2.1, where low level excitations of the nucleon do not excite the diquark, so that there are fewer degrees of freedom and less low-lying excited states of the nucleon are predicated. Alternative models are available for the behaviour of the constituents and

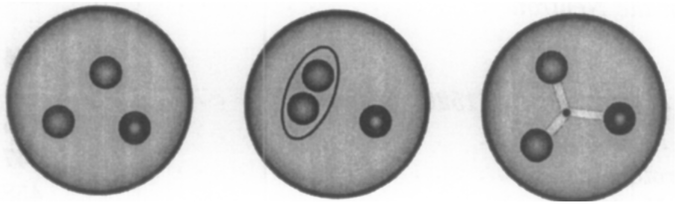

Figure 2.1: Possible effective degrees of freedom in quark models: three equivalent constituent quarks, quark-diquark structure, quarks and flux tubes. Figure from Ref. [4]

the residual interaction. A comprehensive review modern quark models is given by Capstick and Roberts [18].

Lattice QCD shows that a string-like chromoelectric (gluonic) flux tube forms between distant static quarks, which is what confines them to one another. At energies higher than about 2 GeV, it is expected that gluonic degrees of freedom may be excited in mesons allowing them to have quantum numbers not allowed in a $q\bar{q}$ system. The existence of these exotic hybrid mesons, their levels and their orderings will provide important information on the mechanism that produces the flux tube. There is already some evidence for exotic hybrids and gluonic excitations but real progress will be made with the high flux photon beams to be provided by 12 GeV JLab upgrade and the continuing advance of lattice calculations.

2.2.4 Available Theoretical Tools

Theoretical endeavours focus on the fundamental theory of QCD. The most promising directions are numerical simulations of lattice field theory, effective field theory at low energies, and perturbative QCD at high energies. The fragmentation of quarks and the excited states of hadrons are handled with phenomenological models.

Lattice QCD

While QCD cannot be solved analytically in the strong interaction regime, the equations can, in principle, be solved numerically on a four-dimensional lattice of space-time points. The impact of this numerical simulation of lattice field theory continues to increase as algorithms and computational power have improved. This method is currently the only way to calculate the QCD matrix elements for masses, form factors, quark and gluon distributions and polarisabilities—measurements of which are now being made in abundance. The lattice also allows the investigation of QCD aspects which cannot be measured, such as how the properties of the theory change with number of colours or flavours or with quark masses. Progress is made by combining "domain wall valence quarks" which have chiral symmetry on the lattice and a "staggered sea" which is more computationally economical. Lattice QCD calculations are done with with high pion (or light quark) mass and then analytic expressions from chiral perturbation theory are used to extrapolate to a physical pion mass.

There are now a substantial number of calculations performed on the lattice that can be compared with experiment, the highlights of which, taken from [3], are calculations of the nucleon axial charge [19], the isovector nucleon form factors [7], the quark helicity and orbital angular momentum contribution to the nucleon spin [20, 21, 7, 8], the spectra of glueballs and quenched nucleons [22, 23, 24], the mass of the Roper resonance [25], the radiative transition form factors and two-photon decays in charmonium [26, 27], meson-meson scattering lengths and amplitudes [28, 29], and nucleon-nucleon scattering [30, 31].

Effective Field Theories

The useful degrees of freedom at low energies are the mesons and nucleons. Effective field theory organises QFTs into physical scales, consistent with underlying symmetries. The physics at different scales can be systematically separated and solved one scale at a time. The best example is Chiral Perturbation Theory, an effective field theory that takes into account the chiral symmetry property of QCD. Effective field theories have been successful in describing interactions with pions, real and virtual Compton scattering and near-threshold pion photoproduction and electroproduction. They are also be used to extrapolate lattice calculations of parton distributions to the chiral limit.

Perturbative QCD

The asymptotic freedom of QCD allows perturbative methods to be used to describe quarks and gluons at short distances. pQCD is especially useful because of its relation to factorisation, where at high momentum transfer, short-distance and long-distance phenomena may be separated to leading power in the momentum transfer.

An example is *ep* scattering, which at high momentum transfer is factorised into a parton distribution function and a hard-scattering cross section. The latter, which is amenable to pQCD, can be approximated analytically and extracted, allowing a "measurement" of the former. This is the idea behind generalised parton distributions (GPD) [21, 32, 33] which contain information about quark and gluon orbital motion and correlations, providing insights into the spatial distributions of partons in the nucleon. They give us a rigorous map of the entire set of fundamental quantities of hadron structure, such as form factors, polarised and unpolarised parton distributions and the orbital motion contribution to the nucleon spin. Eventually they will map out the complete nucleon wavefunction at the amplitude level.

GPDs are connected to hard exclusive scattering processes such as deeply virtual Compton scattering or meson electroproduction at high momentum transfer, such as the scattering presented in this thesis and described in detail in Chapter 3. The same GPD, which contains information about the hadronic structure, is accessible in a variety of reactions, while the hard perturbative part is reaction specific and calculable—as illustrated schematically in Fig 2.2. Once the GPDs have been measured in enough kinematically diverse areas to constrain them, models of the GPDs will map out the nucleon structure in three dimensions.

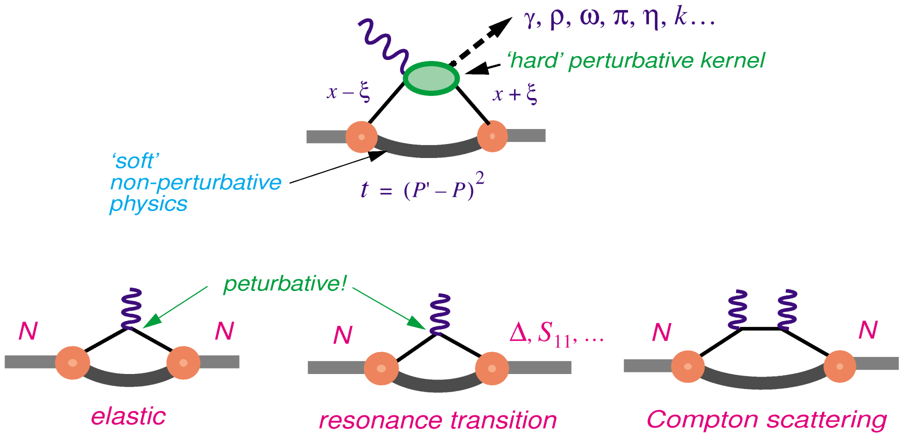

Figure 2.2: The "handbag" diagrams for deep exclusive processes which provide a new window on quark-gluon wavefunctions through their connection to GPDs. Figure from Ref. [34]

There now exist next-to-leading order (NLO) QCD corrections for many of the observables that are sensitive to GPDs, and detailed studies of higher-twist effects have been performed [35], making the extraction of GPDs from data more robust. Perturbative QCD is also used to learn about the polarization of gluons in the proton in hard hadron-hadron scattering in the RHIC Spin program. Here too there are NLO calculations now available [36], which can be sizable, improving the extraction of the soft component.

2.3 Baryon Excited States

In order to study the baryon excited states, we have to start with the ground state. This is an experimental reality, since we cannot make a target of resonances from which to scatter our probes. They are too short-lived, existing for a fleeting 10^{-24} seconds and before decay. When we do measure the structure of these excited states, we necessarily also probe the structure of the nucleon from which they were created, and the quantum operator (mechanism) of their creation. In some sense too, the very reason for studying the baryon excited states, is to learn more about the protons and neutrons of our world, the ground state.

2.3.1 The Ground State and Form Factors

A form factor parametrises our ignorance of the detailed structure of the nucleon. Mathematically, it is that factor which must be multiplied by the known electron scattering cross-section from a point charge

$$\frac{d\sigma}{d\Omega} = \left(\frac{d\sigma}{d\Omega^*}\right)_{\text{point}} |F(q)|^2. \tag{2.1}$$

If an object has structure, then that structure may depend on the resolution at which it is probed. In our case, of electron scattering, the resolution of the probe depends on the magnitude of the four-momentum $|q|$, transferred to the nucleon. For a target that does not recoil, the form factor is the Fourier transform of the charge distribution $\rho(x)$,

$$F(q) = \int \rho(x) e^{iq\cdot x} d^3x. \tag{2.2}$$

It can be shown [37] that if this charge distribution had an exponential form, then the form factor would have the "dipole form"

$$F \propto \left(1 + \frac{Q^2}{m_p^2}\right)^{-2}, \tag{2.3}$$

where $Q^2 = -|q|^2$, m_p is the mass of the proton and $\hbar = c = 1$.

The proton has a magnetisation (electric current) distribution as well as a charge distribution and must therefore be described by 2 form factors $G_E(Q^2)$ and $G_M(Q^2)$, called the electric and magnetic form factors respectively. These are separated by measuring $d\sigma/d\Omega$ as a function of Q^2 and θ.

In the non-relativistic case, for a momentum transfer much smaller than the proton mass $Q^2 \ll m_p^2$, the recoil of the proton can be neglected and the form factors G_E and G_M can be interpreted as the Fourier transforms of the charge and magnetic moment distributions respectively. Expanding Equation 2.2 to the first term in Q^2 allows the mean square radius of the proton to be determined

$$\langle r^2 \rangle = 6 \left(\frac{dG_E(Q^2)}{dQ^2} \right)_{Q^2=0} \sim (0.81 \times 10^{-13}\mathrm{cm})^2, \tag{2.4}$$

yielding a radius of just under a femtometer.

At high momentum transfer $Q^2 > m_p$, such as applicable in this work, there is no direct connection to the charge and magnetic distributions in coordinate space. Nonetheless, the dipole form remains a good model of the proton form factor. This make sense at very high Q^2 because the dipole approximates the Q^{-4} dependence of two gluon exchange in QCD, $(1 + Q^2/m_p^2)^{-2} \sim Q^{-4}$, which is covered in more detail in Section 2.3.3.

An accessible and more extensive introduction into the subject of form factors is given in Ref. [37].

The Nucleon (Elastic) Form Factors

The electromagnetic form factors of the proton and neutron describe the charge and magnetisation distributions of the nucleon, which are due almost entirely to up and down quarks. Originally these were determined from unpolarised electron scattering experiments using the Rosenbluth separation technique [38]. These form factors were measured over a number decades culminating in the high Q^2, high statistics SLAC data [39], shown in Fig. 2.3. At this point, it is important to note that the proton magnetic form factor G_M, is plotted multiplied by Q^4, so that where this quantity $Q^4 G_M^p/\mu_p$ flattens out, from about $Q^2 \sim 8$ GeV^2, is where the form factor is falling

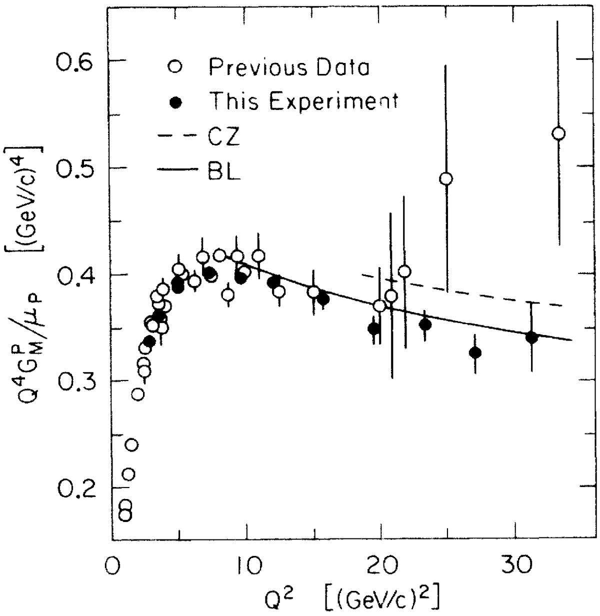

Figure 2.3: The proton magnetic form factor G_M, plotted multiplied by Q^4, as a function of Q^2, to expose the pQCD scaling. Figure from Ref. [39]

with a $1/Q^4$ dependence. This is the behaviour expected if leading order pQCD is sufficient to describe the data. The gently falling slope is due to the running of the strong coupling constant. Section 2.3.3 goes into more detail with regard to this.

Recently both the neutron and proton electric and magnetic form factors have been measured up to $Q^2 \sim 5.6$ GeV^2 using the polarisation transfer technique. The knowledge of both the neutron and proton form factors gives access to the flavour structure of the nucleon. The ratio of the electric and magnetic form factors of the proton G_E/G_M [40], as shown in Fig. 2.4 varies with Q^2, showing that the charge and current distributions withing the proton are not the same. This is a marked difference from the older Rosenbluth separation results, and this difference, which is explained by two photon effects, has given insight into the importance of the two-photon exchange contribution in electron scattering at certain kinematics.

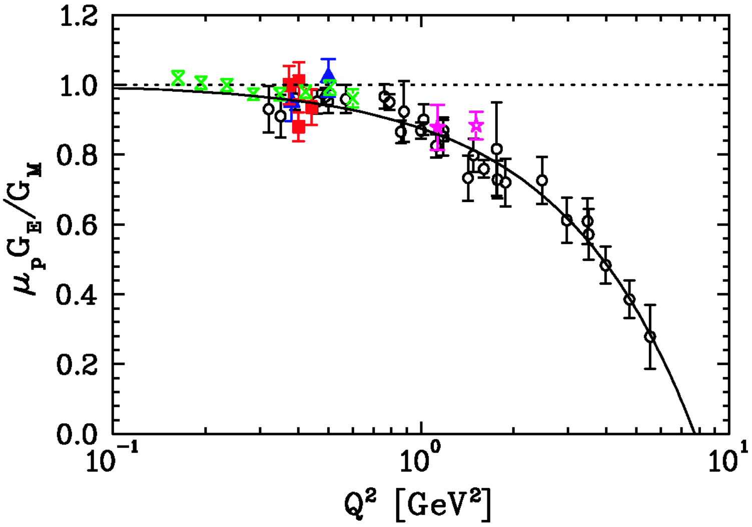

Figure 2.4: Ratio of electric to magnetic form factors for the proton $\mu_p G_E^p / G_M^p$, as determined from polarisation transfer experiments. The charge and current within the proton do not have the same distribution. Figure from Ref. [40]

Pion Form Factor

Measurements of the quark and gluon distributions of mesons, such as the pion and kaon, are comparatively far less advanced than those on the nucleon. On the other hand, since they are somewhat simpler objects, more theoretical progress has been made in this sector. Thus measurements of these form factors offer potential insight into hadron structure.

The electromagnetic structure of the spinless pion is determined by only one form factor. The lowest order diagrams in pQCD give this form factor as

$$F_\pi(Q^2) = 8\pi \frac{\alpha_s f_\pi}{Q^2}, \tag{2.5}$$

where f_π is the pion decay constant. The $1/Q^2$ dependence is due to the exchange of one hard gluon. The transition to hard physics is expected to occur at significantly lower values of Q^2 than for the nucleon.

Measuring the pion form factor is complicated by the lack of a pion target. It can be done up to low Q^2 with a pion beam on atomic electrons. At higher Q^2 it must be done with pion electroproduction off a proton target. Pions from the correct process must be identified, and account must be made for the pion being initially off-shell. Figure 2.5 shows the pion form factor, which has now been measured to $Q^2 = 2.45$ GeV^2 [41, 42], plotted as the quantity Q^2F_π. It appears that at these values of Q^2 that it is consistent with the Q^2-scaling prediction of pQCD.

2.3.2 Excited States

There are two main areas in the study of excited baryons. The first is to study the systematics of the baryon spectrum. This involves identifying the baryon resonances out of data from the many probes and decay channels available and extracting their properties. Eventually this must include solving the "missing baryons" problem and revealing more about the effective degrees of freedom in strong QCD.

Adding energy to a nucleon allows the quarks and gluons to change configurations into excited states. The spectrum of excited states of a system of bound particles exposes the underlying dynamics, which any reasonable model would need to describe. In fact QCD-inspired quark models predict more resonances than are observed, implying that the models have too many degrees of freedom, or that experiments have many more resonances

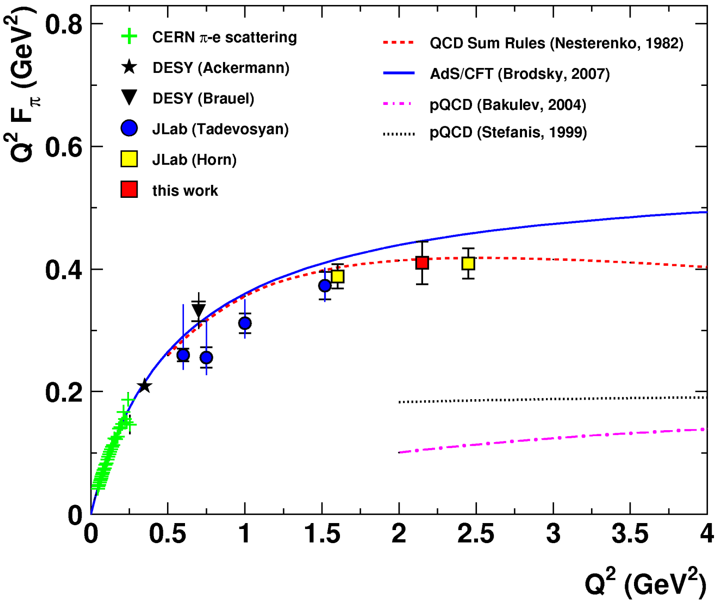

Figure 2.5: Plot of Q^2F_π vs. Q^2. The pion form factor F_π appears to approaching a pQCD scaling of $1/Q^2$ from $Q^2 \sim 3$ GeV^2. Figure from Ref. [41].

to detect. The experimental difficulty is that for the most part the individual resonances, since they are broad and overlapping and may couple only weakly to the commonly measured channels, are tricky to isolate and distinguish from one another. Also, there are some decay channels, ρN, $\Delta\pi$ and ωN, that are difficult to measure experimentally.

The problem of missing resonances can be attacked by a large scale survey investigating many different final states over a large energy range. Candidates for new baryon states have been found in various channels. These will need to be confirmed using polarised-target polarised-beam experiments, the sophistication of which is increasing rapidly, and which provide yet other angles from which to view these states. Extensive data are now becoming available from photoproduction and electroproduction of pseudo-scalar mesons ($\pi, 2\pi, \eta$ and K), vector mesons (ρ, ω, and ϕ), neutral final states ($\pi^0\pi^0$ and $\pi^0\eta$) and on threshold production of strange mesons. Methods of coupled-channel analysis, in which data from all the different channels are analysed simultaneously, will allow much more accurate extraction of resonance parameters, including for well established states.

Modern QCD-inspired models attempt to describe the spectrum of these excited states using a number of approaches. These are comprehensively described in Capstick and Roberts [18] and so here will only be mentioned. Models have for some time been able to describe the masses and strong and electromagnetic couplings of all baryons with reasonable success and with applicability to the meson sector. Available models include the nonrelativistic one-gluon exchange model [43], MIT bag model [44, 45], relativistic bag model [46, 47], cloudy bag model incorporating chiral invariance [48], chiral perturbation theory [49], and in large N_c QCD [50]. Nonrelativistic models need to properly consider the quark kinetic energy to be consistent. On the other hand, relativised models find it difficult to ensure that the dynamics of each of the constituents do not give the hadron state a centre of mass motion. Lattice gauge calculations give properties of the ground and some excited states [51, 52, 53, 54], but the prediction of the excitation spectrum of nucleons is still not possible.

The second area of study is to probe the internal structure of the excited states themselves. Using linearly and circularly polarised photon beams and polarised targets provides access to observables which are sensitive to specific resonances, allowing us to study low lying resonances in great detail, through photoproduction, and providing data for precision tests of models. However, the excitation energies and quantum numbers of baryon excited states are not the observables most sensitive to the model wave functions. The transitions between the states, which reflects their internal structure, are better. These are accessed by measuring the transition form factors through exclusive meson electroproduction as a function of momentum transfer.

The inclusive scattering cross-section as a function of invariant mass W, is plotted in Fig. 2.6 for various values of Q^2. The most significant feature in inclusive electron scattering off a proton, other than the elastic scattering

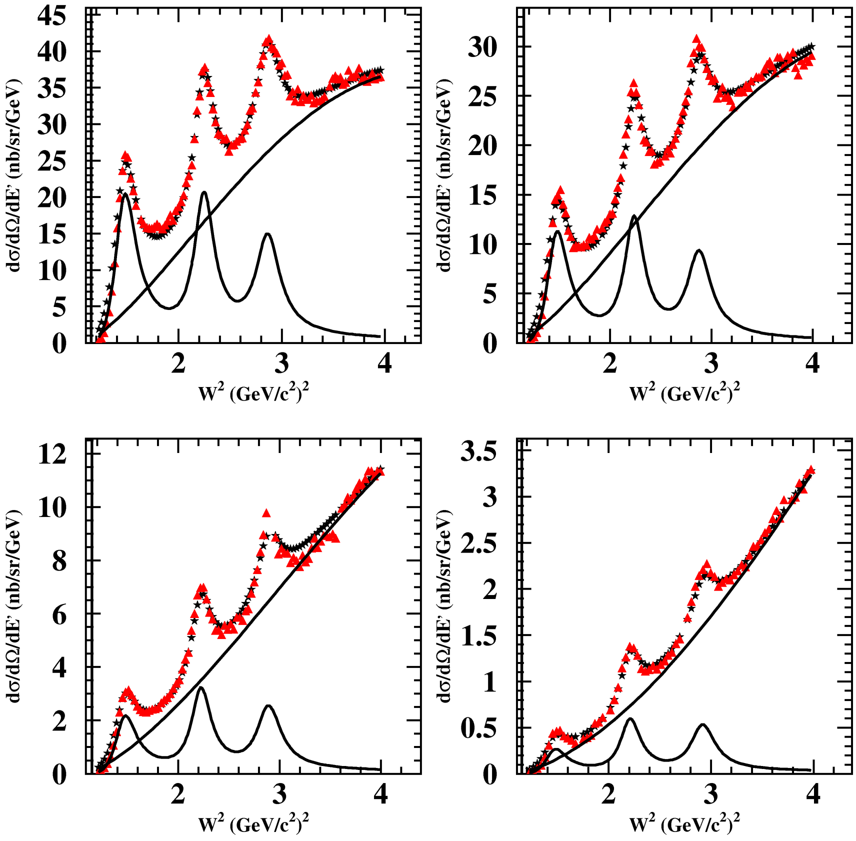

Figure 2.6: Data for ${}^1H(e,e')X$, inclusive electron scattering from the proton in the resonance region. Values of Q^2 are 1.3, 1.7, 2.2, and 3.1 GeV^2. The fit is from Ref. [55]. Figure from Ref. [56]

peak (which is not shown in the figure) are the three maxima in the resonance region, 1 GeV $< W <$ 2 GeV. These are called the first, second and third resonance regions, within which there are at least 20 known resonances. The first resonance region consists only of the $\Delta(1232)$ resonance. The second resonance region is dominated by the negative parity states $D_{13}(1520)$ and $S_{11}(1535)$. These two resonances have different Q^2 dependence, so that for $Q^2 < 1$ GeV^2 the $D_{13}(1520)$ dominates and for $Q^2 > 3$ GeV^2 the $S_{11}(1535)$ dominates [57]. The strongest resonance, at low Q^2, in the third region is the $F_{15}(1680)$.

2.3.3 Transition Form Factors for Excited Baryons

For deep inelastic scattering (DIS), it has been established that pQCD is the correct description to Q^2 as low as a few GeV^2 [58]. In this situation, the interaction is with an asymptotically free quark which is expelled and hadronises, the original proton is destroyed. This is in contrast to the case where the proton stays intact, and is excited into a resonance. The probability of this is process relative to DIS decreases quickly with Q^2, since the incident momentum must be shared among the constituents such that the recoiling system remains in the ground or excited state.

Helicity Amplitude

The helicity amplitude is the matrix element for the absorption of a photon and production of resonance of certain helicity. This quantity contains the information about the charge and current structure of the baryon in the initial and final states and the transition operator. The various possible ways of interacting a virtual photon with a proton and producing a resonance of certain helicity are shown in Fig. 2.7. It can be seen that the $A_{1/2}$ amplitude

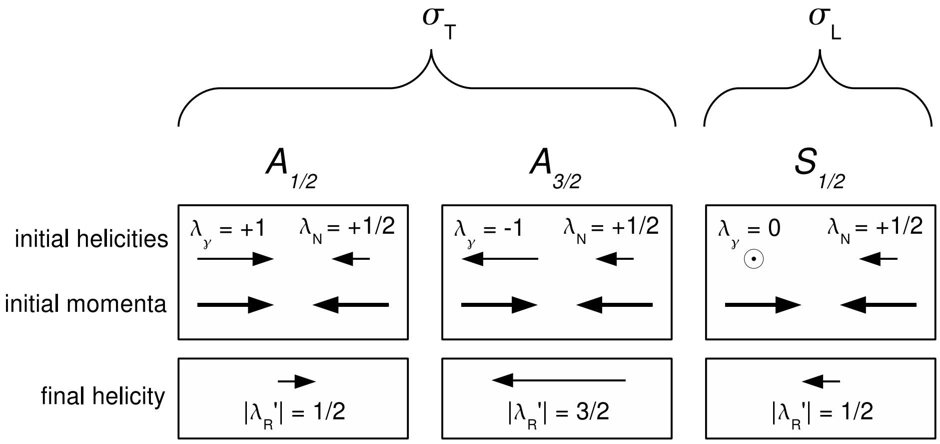

Figure 2.7: Possible helicity configurations for producing a baryon resonance from a nucleon N and virtual photon γ. Since the $S_{11}(1535)$ resonance is a spin-$\frac{1}{2}$ object, only the $A_{1/2}$ and $S_{1/2}$ amplitudes apply to this work. The $A_{1/2}$ amplitude is helicity conserving. Figure similar to one in Ref. [56]

is helicity conserving. The transverse helicity amplitudes are related to the transverse cross section at the resonance position by

$$\sigma_T(W_R, Q^2) = \frac{2m_N}{W_R\Gamma_R}|A_H(Q^2)|^2, \tag{2.6}$$

where $|A_H(Q^2)|^2 = |A_{1/2}(Q^2)|^2 + |A_{3/2}(Q^2)|^2$. Section 3.2.3 goes into detail obtaining Equation 2.6 and determining the helicity amplitude in the case of the $S_{11}(1535)$ resonance of this measurement.

pQCD predicts that at high Q^2, for photons interacting with spin-1/2 quarks, the helicity amplitudes scale as

$$A_{1/2} \propto Q^2 A_{3/2}. \tag{2.7}$$

Thus in the high Q^2 limit, only the helicity conserving amplitude $A_{1/2}$ contributes [59].

In order to compare the Q^2 dependence of resonances with that of the nucleon elastic form factors, a dimensionless transition form factor $F(Q^2)$ is defined in terms of the helicity amplitudes [60]

$$|F(Q^2)|^2 = \frac{1}{4\pi\alpha}\frac{2m_N}{Q^2}(W_R^2 - m_N^2)|A_H(Q^2)|^2. \tag{2.8}$$

The two are equivalent conceptually, but differ by some constants and a factor of $1/Q$.

High Q^2 calculations are commonly carried out in the light-cone frame and may be factorised [59], into a hard scattering operator T_H, a sum of the leading order perturbative terms, and a distribution amplitude Φ, containing the non-perturbative parts of the form factor, as

$$F(Q^2) = \int dxdy\Phi^*(x)T_H\Phi(y), \tag{2.9}$$

where the x and y are the initial and final longitudinal fractional momentum fraction respectively. In the leading order, two gluons are exchanged between three quarks, as in Fig. 2.8. If the transition operator only depends on the leading order diagrams, it takes the form [62, 59]

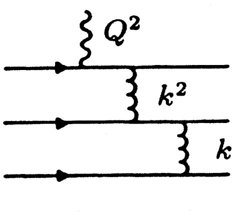

Figure 2.8: Leading order pQCD diagram for calculating transition amplitudes of elastic scattering or inelastic resonance scattering. Figure from Ref. [61]

$$T_H = \frac{\alpha_s^2(Q^2)}{Q^4}f(x,y). \tag{2.10}$$

This constituent scaling or quark counting, results in the well know scaling behaviour $F \propto 1/Q^4$ or $A_{1/2} \propto 1/Q^3$. In addition to the leading order pQCD decrease, there is also a logarithmic decrease with Q^2 due to running of the coupling constant α_s. This "ideal" behaviour is perfectly demonstrated by the elastic form factor, Fig. 2.3. An analysis by Stoler [61] showed that the integral of the second or third resonance regions, as determined by inclusive scattering, scales according to leading order in pQCD from about $Q^2 \sim 5$ GeV^2 until the data ends at $Q^2 \sim 20$ GeV^2. If each of these resonance regions is dominated by a single resonance, which is a good approximation for the $S_{11}(1535)$ in the second resonance region at high Q^2 [63], then these resonances show the "correct" pQCD scaling behaviour. On the other hand, the $\Delta(1232)$ resonance, which *is* the first resonance region all by itself, drops faster than $1/Q^4$.

Separating the contributing electromagnetic multipoles requires measurements of exclusive reactions such as $e(p, e'p)\pi^0$ and $e(p, e'p)\eta$. Historically, these measurements were difficult because the resonance form factors drop quickly with Q^2 and there is significant non-resonant contribution. These measurements are now possible with very high luminosity, continuous, high energy electron beams. The data presented in this thesis is one such measurement of the $e(p, e'p)\eta$ reaction at a Q^2 of ~ 5.8 and 7.0 GeV^2. This will be covered in great detail in Chapter 3.

The $\Delta(1232)$ Resonance

The baryon resonance that is most studied is the $\Delta(1232)$. This is the lightest resonance, and since there are no others in its mass range, it is well separated. Using data taken concurrently with the data presented in this thesis, the magnetic form factor for the $\Delta(1232)$ resonance G_M, has been extracted from the exclusive channel $e(p, e'p)\pi^0$. This was done at $Q^2 = 6.3$ and 7.7 GeV^2, the highest ever momentum transfer for this reaction, see the PhD thesis of Villano [1]. The fit was magnetic dipole dominated with all other multipoles assumed to be small. This data are plotted in Fig 2.9, and show that the form factor for the $\Delta(1232)$ resonance continues to fall far quicker than that of the nucleon, represented here by the dipole form factor, G_D. This is also much quicker than $1/Q^4$.

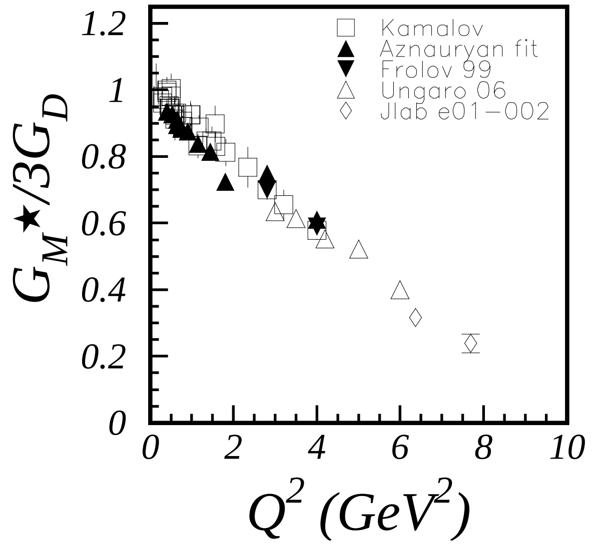

Figure 2.9: Plot of $G_M/3G_D$ for the $\Delta(1232)$ resonance. The magnetic form factor of this resonance decreases with Q^2 much faster than the proton electric form factor. Figure from Ref. [1]

It is suggested [60, 64] that the rapid falloff of the $\Delta(1232)$ is due to a cancellation of the leading terms of the matrix elements connecting the symmetric $\Delta(1232)$ distribution function with the symmetric and antisymmetric proton distribution function, $\langle\phi_\Delta|T_H|\phi_p^S\rangle$ cancels with $\langle\phi_\Delta|T_H|\phi_p^A\rangle$. This would leave $A_{3/2}$ as the dominant amplitude, which does fall faster than Q^{-4} at high Q^2, Equation 2.7.

The $P_{11}(1440)$ (Roper) Resonance

The Roper resonance is somewhat of an enigma because it has a radial excitation of $N = 2$ and yet its mass is less than resonances with $N = 1$. The transition form factors for the Roper resonance, shown in Fig 2.10, has been measured up to $Q^2 = 4$ GeV^2. The data are well described with relativistic quark model calculations of Capstick and Keister [65] and Aznauryan [66] showing that at small distances there is a quark substructure rather than some kind of hybrid-baryon or meson-baryon-molecule behaviour, as previously thought. However, these approaches do not reproduce the transverse amplitude $A_{1/2}$, at $Q^2 = 0$, possibly due to a large pion cloud contribution [67].

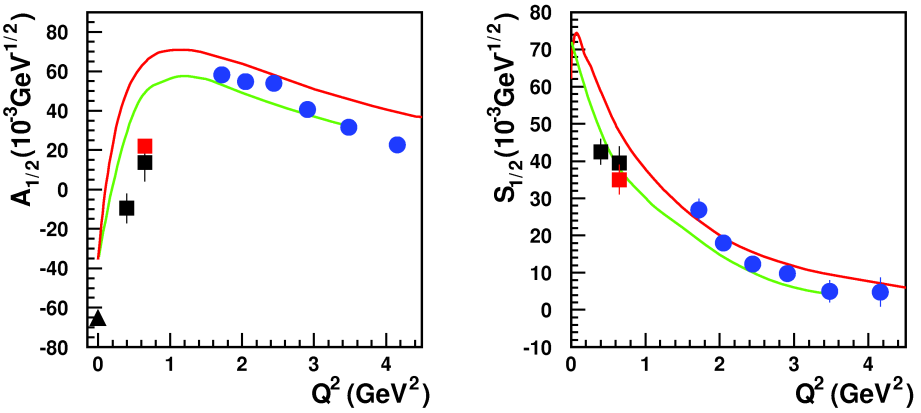

Figure 2.10: The transition form factors for the Roper resonance $P_{11}(1440)$, well described with relativistic quark model calculations of Capstick and Keister [65], the red curve, and Aznauryan [66], the green curve. Data from Refs. [67, 68, 69]. Figure from Ref. [3]

The $S_{11}(1535)$ Resonance

Determining the helicity conserving amplitude for the $S_{11}(1535)$ resonance, at high Q^2, is the subject of Chapter 3. The experiment is described in detail there, culminating in the extraction of this amplitude, shown in Fig 3.27, and comparison with theoretical predictions from CQM to pQCD, none of which can explain the full Q^2 dependence of this quantity. These new data represent a clear challenge to theorists to explain the Q^2 dependence of this quantity.

2.4 Summary

Nuclear physics is a vibrant and active field in which there remain many mysteries and much to be done. Our understanding of nuclear structure is advancing rapidly both on the experimental and theoretical front, and surprising results seem to occur regularly. Studying baryon resonances, and their production from the ground state nucleons, offers an opportunity to test models at a series of distance scales, by varying the momentum transfer. The long distance scale behaviour is quite well described by constituent quark models and at short enough distance scales pQCD is a good description. By studying the transition from one regime to the other we can check the range of validity of the models and thereby the underlying assumptions. The next chapter describes the the measurement of the helicity amplitude for production of the $S_{11}(1535)$ resonance at the highest ever momentum transfer. The data significantly extends our knowledge of this resonance's production strength to what appears to be the beginning of the pQCD region.

Chapter 3

Electroproduction of η Mesons in the $S_{11}(1535)$ Resonance Region at High Momentum Transfer

3.1 Introduction

The goal of strong interaction physics is to understand hadrons in terms of their fundamental constituents, the quarks and gluons. Although these constituents are described by Quantum Chromodynamics (QCD), and perturbative methods work well where applicable, mostly the complexity of the theory precludes a description of hadrons in terms of QCD. Various techniques are used to make progress, such as numerical simulation of QCD and hadron models with effective QCD degrees of freedom. In this sense, the role of experiment is to make measurements which test the predictions of QCD-inspired quark models. Most models can describe the static nucleon properties and the baryon spectrum, and so other measurements, such as electromagnetic transition form factors and strong decay amplitudes, are required.

A baryon's quark substructure can be excited into a resonance—an excited state of the quarks with well-defined baryon quantum numbers. The transition form factor is the coupling (amplitude for the transition) from one baryon state to another, as a function of the squared invariant momentum transferred to the baryon Q^2. The measurements of couplings between baryon states and the dependence of these on Q^2, can be used as stringent tests of quark models. These couplings can be expressed in terms of the transition matrix elements between states of definite helicity.

The difficulty in measuring baryon transition form factors lies in isolating any of the multitude of wide and overlapping resonant states. The $S_{11}(1535)$ is a baryon resonance that can be accessed relatively easily. Although there are many overlapping states in its mass region, it is very strongly excited over the accessible Q^2 range and is the only resonance with a large branching fraction to η mesons [70], causing it to dominate the $p(e, e'p)\eta$ channel. This dominance is partly due to isospin conservation, since the proton has isospin=$\frac{1}{2}$ and the η has isospin=0, only the $N^*(I = \frac{1}{2})$ resonances can decay to a proton-η final state—$N^*(I = \frac{3}{2})$ resonances are forbidden.

As well as being accessible, the S_{11} is an interesting resonant state. It is the negative parity partner of the nucleon, they are both spin-half and isospin-half particles. The transition form factor for the production of the S_{11} falls more slowly with Q^2 than the dipole form factor $G_D = (1 + Q^2/0.71)^{-2}$, at least up to $Q^2 = 3.6$ GeV^2 [63], and more slowly than the form factor for typical baryons. An example is the $D_{13}(1520)$ [71], which is from the same $SU(6) \bigotimes O(3)$ multiplet and mass region as the $S_{11}(1535)$.

The $S_{11}(1535)$ branching fraction to $p\eta$, at $b_\eta \sim 50\%$, is anomalously high when compared to that of the other N^* resonances, a phenomenon which is not well understood.

It is expected from helicity conservation in perturbative QCD (pQCD) that at sufficiently high Q^2 the photocoupling amplitude $A_{1/2}$ will begin to scale as $1/Q^3$ [60], or equivalently the quantity $Q^3 A_{1/2}$ will flatten. The observation of such scaling is thus a possible signal of the transition to the dominance of hard processes. This motivates the present experiment which studies exclusive η production, allowing access to the amplitude $A_{1/2}$ for the S_{11} resonance, at the highest ever Q^2 yet measured.

The first measurement of η production at substantial Q^2 was published by Brasse *et al.* [57] in 1984 based on work at DESY that went to $Q^2 = 2.0$ and 3.0 GeV^2. This was the first indication that the $S_{11}(1535)$ falls far slower with Q^2 than the $D_{13}(1520)$, and hence dominates the channel at high Q^2.

In 1999, Armstrong *et al.* [63] published data obtained in Hall C at Jefferson Lab at $Q^2 = 2.4$ and 3.6 GeV^2, the highest Q^2 until this work. The cross-section was found to be about 30% lower than the DESY data and the full width of the $S_{11}(1535)$ about twice as wide. By comparing with inclusive data, a lower bound was put on the branching fraction $S_{11} \rightarrow \eta p$ of $b_\eta > 0.45$.

A recent paper by the CLAS collaboration from Hall B at Jefferson Lab [72], published data for this process, at centre-of-mass (c.m.) energy $W = 1.5 - 2.3$ GeV and $Q^2 = 0.13 - 3.3$ GeV^2. The photocoupling amplitude $A_{1/2}$ of the proton to $S_{11}(1535)$ transition was extracted, and the anisotropies in the differential cross-section were more precisely determined. The results for the magnitude and width of the S_{11} resonance favoured the

Armstrong data over the older Brasse result. Evidence was shown for a significant contribution to η electroproduction due to a P-wave resonance with a mass around 1.7 GeV.

This thesis describes an experiment where electrons were scattered off free protons at high momentum transfer and both electron and proton were detected in coincidence. In Sec. 3.2 the kinematics of the reaction are discussed along with the formalities of the cross section and helicity amplitude for $S_{11}(1535)$ production. Sec. 3.3 describes the apparatus and methods used to acquire the data. Sec. 3.4 then goes on to present the processing of the data including corrections, calibration, cuts, Monte Carlo simulation, backgrounds and ultimately the cross section extraction and error analysis. In Sec. 3.5 the η production differential cross section is plotted and fit with an angular dependence. A Breit-Wigner form is fitted to the data and the S_{11} helicity amplitude and resonance parameters are extracted. A brief summary is given in Sec. 3.6. The appendix tabulates the extracted η production differential cross section.

3.2 Formalism

3.2.1 Kinematics

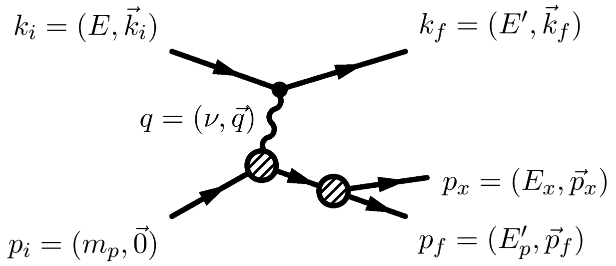

Figure 3.1: The one-photon exchange diagram of the resonance electroproduction process, where, for example, k_i is the four-momentum vector of the incoming electron composed of energy E and momentum $\vec{k}_i$.

Figure 3.1 shows the one-photon exchange (Born) diagram for the resonance electroproduction process. The incident electron k_i scatters off the stationary proton p_i with mass m_p. We detect the scattered electron k_f and proton p_f and reconstruct the undetected particle p_x using the missing mass technique, evaluated from four-momentum conservation

$$m_x^2 = (p_i + k_i - p_f - k_f)^2. \tag{3.1}$$

Using the symbols from the diagram and neglecting the electron mass, the positive square of the four-momentum transferred from the lepton to hadron system is $Q^2 \equiv -q^2 = 4EE'\sin^2(\theta_e/2)$. The mass of the resonant state is $W^2 = (q + p_i)^2 = q^2 + m_p^2 + 2m_p\nu$.

Figure 3.2 shows the scattering and reaction plane coordinate systems: θ_e is the scattering angle of the electron; θ_{pq} the angle between the outgoing proton and the momentum vector of the virtual photon, $\boldsymbol{q}$; the polar and azimuthal angles of the missing momentum are θ_x^* and ϕ_x respectively, defined with respect to $\boldsymbol{q}$ and the electron scattering plane. A super-scripted * denotes measurement in the $p\eta$ centre-of-momentum frame.

3.2.2 Cross Section

The five-fold differential cross-section for the reaction may be expressed, following the standard convention [73, 74, 75], as the product of the transverse virtual photon flux Γ_T and the centre-of-mass cross-section for the electroproduction of the $p\eta$ pair

$$\frac{d^4\sigma}{dW dQ^2 d\phi_e d\Omega_\eta^*} = \Gamma_T(W, Q^2)\frac{d\sigma}{d\Omega_\eta^*}(\gamma_v p \to p\eta), \tag{3.2}$$

where the flux of transverse virtual photons in the Hand convention [76] is

$$\Gamma_T(W, Q^2) = \frac{\alpha}{4\pi^2}\frac{W}{m_p E^2}\frac{K}{Q^2}\frac{1}{1-\epsilon}, \tag{3.3}$$

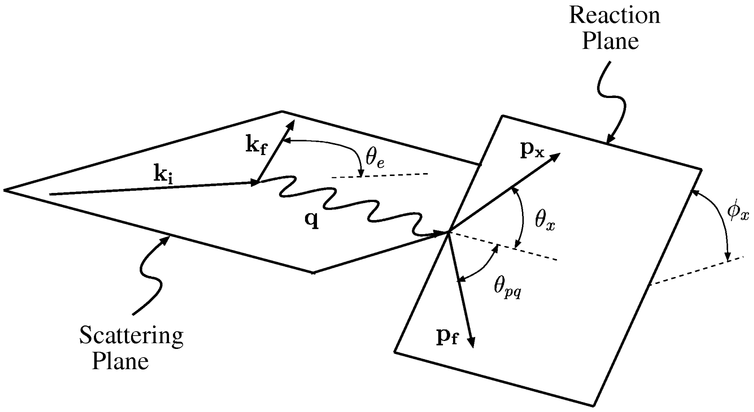

Figure 3.2: The scattering and reaction plane coordinate systems. Figure from Ref. [63].

the longitudinal polarisation of the virtual photon is given by

$$\epsilon = \frac{1}{1 + 2\frac{|\boldsymbol{q}|^2}{Q^2}\tan^2(\theta_e/2)}, \tag{3.4}$$

and the energy required by a real photon to excite a proton to a resonance of mass W is

$$K = \frac{W^2 - m_p^2}{2m_p}. \tag{3.5}$$

The unpolarised virtual photon cross-section is written in terms of the transverse polarised virtual photon $d\sigma_T/d\Omega^*_\eta$, longitudinal polarised virtual photon $d\sigma_L/d\Omega^*_\eta$ and interference contributions, $d\sigma_{LT}/d\Omega^*_\eta$ and $d\sigma_{TT}/d\Omega^*_\eta$ as

$$\begin{aligned}\frac{d\sigma}{d\Omega^*_\eta}(\gamma_v p \to p\eta) &= \frac{d\sigma_T}{d\Omega^*_\eta} + \epsilon\frac{d\sigma_L}{d\Omega^*_\eta} + \sqrt{2\epsilon(1+\epsilon)}\frac{d\sigma_{LT}}{d\Omega^*_\eta}\cos\phi^*_\eta \\ &\quad + \epsilon\frac{d\sigma_{TT}}{d\Omega^*_\eta}\cos 2\phi^*_\eta. \end{aligned} \tag{3.6}$$

Each of these four individual components are expressed in terms of multipoles [77, 78], where $E_{l\pm}$, $M_{l\pm}$ and $S_{l\pm}$ are the electric, magnetic and scalar multipoles respectively; l is the orbital angular momentum, and ± indicates the total angular momentum via $j = l \pm \frac{1}{2}$. Retinaing only terms with $l \leq 2$ and either of the dominant isotropic multipoles, E_{0+} or S_{0+}, gives [79]

$$\begin{aligned}
\frac{d\sigma_T}{d\Omega^*_\eta} &= \frac{|\mathbf{p}^*_\eta|W}{m_pK}\Big\{|E_{0+}|^2 - \mathrm{Re}\Big[E^*_{0+}\{2\mathrm{cos}\theta^*_\eta M_{1-} \\
&\quad -(3\mathrm{cos}^2\theta^*_\eta - 1)(E_{2-} - 3M_{2-})\}\Big]\Big\}, \\
\frac{d\sigma_L}{d\Omega^*_\eta} &= \frac{Q^2}{|\mathbf{q}^*|^2}\frac{|\mathbf{p}^*_\eta|W}{m_pK}\Big\{|S_{0+}|^2 + 2\mathrm{Re}\Big[S^*_{0+}\{2\mathrm{cos}\theta^*_\eta S_{1-} \\
&\quad -2(1 - 3\mathrm{cos}^2\theta^*_\eta)S_{2-}\}\Big]\Big\}, \\
\frac{d\sigma_{LT}}{d\Omega^*_\eta} &= \sqrt{\frac{Q^2}{|\mathbf{q}^*|^2}}\frac{|\mathbf{p}^*_\eta|W}{m_pK}\Big\{ - \mathrm{sin}\theta^*_\eta\mathrm{Re}\Big[E^*_{0+}(S_{1-} + 6\mathrm{cos}\theta^*_\eta S_{2-}) \\
&\quad +S^*_{0+}\{M_{1-} + 3\mathrm{cos}\theta^*_\eta(M_{2-} - E_{2-})\}\Big]\Big\}, \\
\frac{d\sigma_{TT}}{d\Omega^*_\eta} &= \frac{|\mathbf{p}^*_\eta|W}{m_pK}\Big\{ - 3\mathrm{sin}\theta^*_\eta\mathrm{Re}\Big[E^*_{0+}(M_{2-} + E_{2-})\Big]\Big\}. \qquad (3.7)
\end{aligned}$$

If the unpolarised virtual photon cross-section is parametrised in terms of its angular dependence as [56]

$$\begin{aligned}
\frac{d\sigma}{d\Omega^*} &= A + B\ \mathrm{cos}\theta^* + C\ \mathrm{cos}^2\theta^* + D\ \mathrm{sin}\theta^*\mathrm{cos}\phi^* \\
&\quad +E\ \mathrm{cos}\theta^*\mathrm{sin}\theta^*\mathrm{cos}\phi^* + F\ \mathrm{sin}^2\theta^*\mathrm{cos}2\phi^*, \qquad (3.8)
\end{aligned}$$

then the parameters $A-F$ are then given in terms of the truncated multipole expansion by

$$\begin{aligned}
A &= \frac{|\mathbf{p}^*_\eta|W}{m_pK}\Big\{|E_{0+}|^2 + \epsilon\frac{Q^2}{|\mathbf{q}^*|^2}|S_{0+}|^2 \\
&\quad -\Big(\mathrm{Re}[E^*_{0+}(E_{2-} - 3M_{2-})] + 4\epsilon\frac{Q^2}{|\mathbf{q}^*|^2}\mathrm{Re}[S^*_{0+}S_{2-}]\Big)\Big\}, \\
B &= \frac{|\mathbf{p}^*_\eta|W}{m_pK}\Big\{ - 2\mathrm{Re}[E^*_{0+}M_{1-}] + 2\epsilon\frac{Q^2}{|\mathbf{q}^*|^2}\mathrm{Re}[S^*_{0+}S_{1-}]\Big\}, \\
C &= \frac{|\mathbf{p}^*_\eta|W}{m_pK}\Big\{3\Big(\mathrm{Re}[E^*_{0+}(E_{2-} - 3M_{2-})] \\
&\quad +4\epsilon\frac{Q^2}{|\mathbf{q}^*|^2}\mathrm{Re}[S^*_{0+}S_{2-}]\Big)\Big\},
\end{aligned}$$

$$
\begin{aligned}
D &= \frac{|\mathbf{p}^*_\eta|W}{m_pK}\Big\{-\sqrt{2\epsilon(\epsilon+1)}\sqrt{\frac{Q^2}{|\mathbf{q}^*|^2}}\mathrm{Re}[E^*_{0+}S_{1-} \\
&\quad +S^*_{0+}M_{1-}]\Big\}, \\
E &= \frac{|\mathbf{p}^*_\eta|W}{m_pK}\Big\{-3\sqrt{2\epsilon(\epsilon+1)}\sqrt{\frac{Q^2}{|\mathbf{q}^*|^2}}\mathrm{Re}[2E^*_{0+}S_{2-} \\
&\quad +S^*_{0+}(M_{2-}-E_{2-})]\Big\}, \\
F &= \frac{|\mathbf{p}^*_\eta|W}{m_pK}\Big\{-3\epsilon\mathrm{Re}[E^*_{0+}(E_{2-}+M_{2-})]\Big\}.
\end{aligned} \tag{3.9}
$$

3.2.3 Helicity Amplitude

The helicity amplitude is the matrix element that connects states of definite (the same or different) helicity. As such, it is a convenient measure of the coupling strength between states and can be used to fundamentally test quark models. The amplitudes are labeled by the virtual photon polarisation (either transverse A or longitudinal S) and the total γN helicity ($\frac{1}{2}$ or $\frac{3}{2}$). Spin-$\frac{1}{2}$ resonances are therefore described only by $A_{1/2}$ and $S_{1/2}$.

The helicity amplitude $A_{1/2}$, for the process $\gamma_v p \to S_{11}(1535)$, can be obtained from the contribution of the $S_{11}(1535)$ to the E_{0+} multipole at the resonant mass $W = W_R$, using [80, 81]

$$
A_{1/2} = \left[2\pi\frac{|\boldsymbol{p}^*_\eta|_R W_R}{m_pK}\frac{W_R}{m_p}\frac{\Gamma_R}{b_\eta}\right]^{1/2}|E_{0+}(W_R)|. \tag{3.10}
$$

This requires, not only isolating the $S_{11}(1535)$ from the other resonances and the non-resonant background, but further isolating the E_{0+} multipole from the other multipoles. In this case, for $\gamma_v p \to \eta p$ at the $S_{11}(1535)$ resonance mass, such an isolation is almost implicit in the measurement due to the dominance of the $S_{11}(1535)$. Being an S-wave resonance, implies a dominance of the isotropic multipoles—which has previously been seen in the data [63, 82, 57, 72]. So too, among the isotropic contributions it appears that the transverse multipole E_{0+}, dwarfs the longitudinal part S_{0+} [71, 83, 72].

Doing a longitudinal/transverse (LT) separation requires measuring the cross-section for at least two values of ϵ at the same Q^2, which was not done in this experiment. Such separations performed in the late 1970's [71, 83] are consistent with no longitudinal component, although this is with large uncertainties and the data only extends up to $Q^2 \sim 1$ GeV^2. Recent data [72], shows $d\sigma_{\mathrm{LT}}/d\Omega^*$ consistent with zero, suggesting that the longitudinal component is small—but since $d\sigma_{\mathrm{LT}}/d\Omega^*$ is a sum of terms with possibly different signs, it is possible that S_{0+} is in fact comparable to E_{0+}. In this thesis it is assumed that the longitudinal amplitudes are not significant for this reaction. The validity of this will become clear in the future when LT separations are done at high Q^2.

The cross-section can thus be written as depending only on the dominant E_{0+} multipole in the simple form

$$\frac{d\sigma}{d\Omega^*_\eta} \approx \frac{|\boldsymbol{p}^*_\eta|W}{m_p K}|E_{0+}|^2. \tag{3.11}$$

The combination of Eqs. (3.11) and (3.10) yields

$$A_{1/2}(Q^2) = \sqrt{\frac{W_R \Gamma_R}{2 m_p b_\eta}\sigma_R(Q^2)}, \tag{3.12}$$

the helicity amplitude as a function of $\sigma_R \equiv \sigma(W_R)$ [the total cross-section of the $S_{11}(1535)$ resonance, measured at the resonance mass W_R.]

The E_{0+} multipole can be more reliably extracted from a fit to the angular dependence. Parameters A and C in Eqs. (3.9) share some common terms, and a simple cancellation yields Eq. (3.13)—although in the absence of an LT separation, it still must be assumed that S_{0+} is negligible:

$$A + \frac{1}{3}C = \frac{|\mathbf{p}^*_\eta|W}{m_p K}\left\{ |E_{0+}|^2 + \epsilon \frac{Q^2}{|\mathbf{q}^*|^2}|S_{0+}|^2 \right\}$$

$$\approx \frac{|\mathbf{p}_\eta^*|W}{m_p K}|E_{0+}|^2. \tag{3.13}$$

Where possible in this work, the E_{0+} multipole is extracted using both methods, but for consistency with previous analyses the final result is quoted from the method assuming isotropy.

3.3 The Experiment

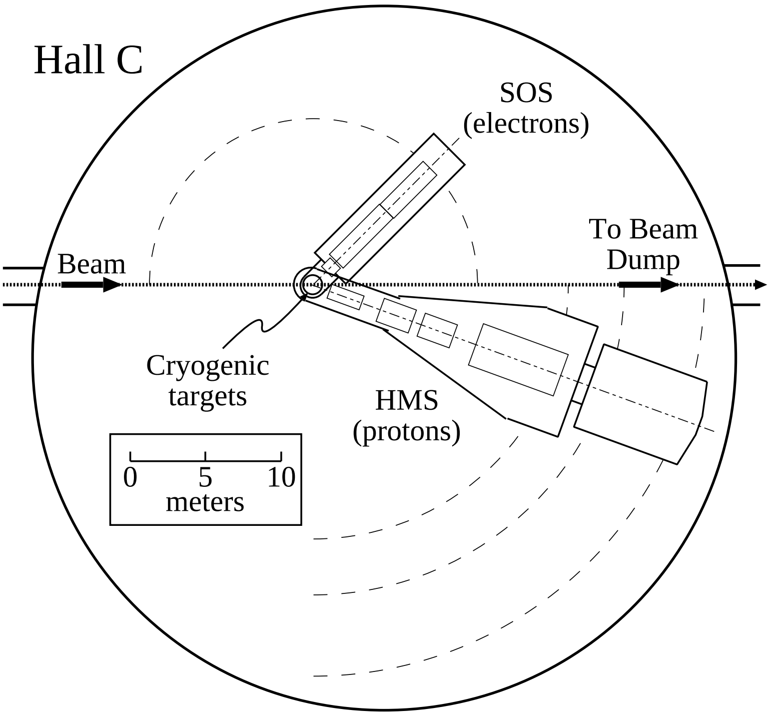

Figure 3.3: A plan view of Hall C showing the beamline, target and the SOS and HMS spectrometers which detected electrons and protons respectively. Figure from Ref. [63].

The experiment, measuring the unpolarised differential cross-section for the process $p(e, e'p)\eta$, was performed in Hall C (Fig. 3.3) of the Thomas Jefferson National Accelerator Facility, during May and June of 2003. The

Short Orbit Spectrometer (SOS) [84], a resistive $QD\overline{D}$ (quadrupole, dispersive dipole, anti-dispersive dipole) spectrometer, was used to detect scattered electrons. The High Momentum Spectrometer (HMS) [85], with a superconducting $QQQD$ configuration, detected the recoil protons. The η particles were identified using the missing mass method.

Both spectrometers have a similar detector ensemble, including drift chambers for determining the track, scintillator arrays for triggering, an electromagnetic calorimeter for particle identification (PID) and a threshold gas Čerenkov also for PID and tuned to differentiate between pions and electrons in the SOS. Figure 3.4, showing the detector components, is representative of either detector stack.

The Jefferson Laboratory's superconducting radiofrequency Continuous Electron Beam Accelerator Facility (CEBAF) provides multi-GeV continuous-wave beams for experiments at the nuclear and particle physics interface [86]. The accelerator consists of two anti-parallel linacs linked by nine recirculation beam lines in the shape of a racetrack, for up to five passes. Beam energies up to nearly 6 GeV at 100 μA and $> 75\%$ polarization are possible. For this experiment, the incident electrons had the maximum available energy: $E_e = 5.500$ GeV for most of the experiment and $E_e = 5.491$ GeV for an 11 day period near the beginning.

The target was liquid hydrogen maintained at a temperature of 19 K. The beam passes through 3.941 cm of liquid and through 0.12 mm of aluminium target cell walls on entrance and exit. The beam was rastered within a square of ± 1 mm to minimise density changes due to target boiling. A dummy target consisting of two aluminium plates was used to simulate reactions within the target walls.

The trigger for the experiment was a coincidence between pre-triggers

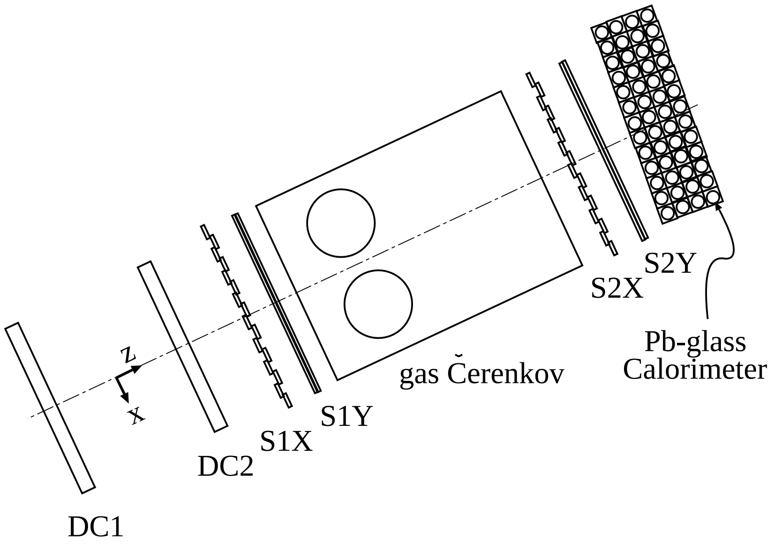

Figure 3.4: A side view of the HMS detector stack, which is also representative of the SOS. The detected particles travel from left to right, encountering first the two drift chambers (DC) then the first two arrays of scintillators (S1) oriented in the X and Y directions, then the gas Čerenkov detector, the third and fourth scintillator arrays and finally the calorimeter. Figure from Ref. [63]

(or singles triggers) from both of the spectrometers. Both of the spectrometer pre-triggers were the requirement of a signal in three out of the four scintillator planes (SCIN). In addition to the coincidence trigger, data were taken for singles triggers from both of the two spectrometers. This was pre-scaled according to the rate so as not to interfere with the coincidence trigger. This singles data allowed the monitoring of the luminosity and the electron detection efficiency. The elastic scattering events within the SOS were used to monitor the beam energy and the performance of the SOS magnets.

Blok *et. al* [87] is descriptive of the accelerator, beam monitoring equipment and current monitors, target rastering system, beam energy measurement and cryogenic target. More detailed discussions are made of the two spectrometers, their detector packages, the trigger logic and data acquisition. Further references are provided for all covered topics and the interested reader is advised to consult that work.

The electron spectrometer was fixed in angle and momentum, thereby defining a central three-momentum transfer vector $\vec{q}$ for the virtual photon which mediates the reaction. Around this $\vec{q}$ vector is a cone of reaction products including the protons from the resonance decay of interest in this measurement. The "kinematic focusing" caused by the high momentum transfer of the reaction makes it possible to capture a large fraction of centre of mass decay solid angle in a spectrometer, as it comes out as a "narrow" cone in the lab. The proton spectrometer was stepped in overlapping angle and momentum steps to capture as much of this decay cone as possible.

The exact choice of kinematics was based on a compromise between maximising the Q^2 for the available beam energy and detecting the full centre-of-mass decay cone for the $p(e, e'p)\pi^0$ reaction to the highest possible W. This reaction, which was measured concurrently is reported on by Villano [1]. The maximum central momentum of the SOS, 1.74 GeV, required increasing θ_{SOS} to increase the Q^2, while the minimum HMS angle of 10.5 degrees required decreasing θ_{SOS} to extend the full angular coverage to higher W. At $\theta_{\mathrm{SOS}} = 47.5$ degrees and the maximum SOS momentum, it was found that the kinematic region from pion threshold to above the S_{11} mass fell nicely within the best resolution region of the SOS spectrometer and full $\cos\theta^*$ coverage was possible for the $p\pi^0$ up to $W = 1.4$ GeV and $p\eta$ up to $W = 1.6$ GeV, as shown in Fig. 3.5. These SOS central parameters correspond to a virtual photon with momentum 4.51 GeV and angle

16.5 degrees and $Q^2 \sim 5.8$ (GeV/c)^2 at the S_{11} resonance mass.

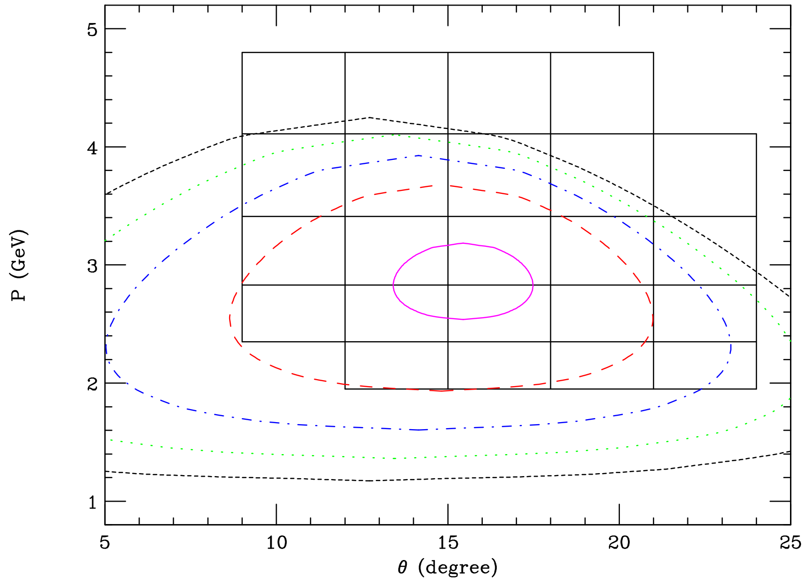

Figure 3.5: The W acceptance of the detector pair for the $e(p, e'p)\eta$ reaction, in the lower-Q^2 configuration, as a function of the laboratory scattering angle and momentum of the proton. The contours are constant W of the hadronic system, for an electron at 47.5 degrees and momentum of 1.74 GeV/c, for the full range of θ^* and $\phi = 0$ and 180 degrees. The solid central contour is $W = 1.5$ GeV, from which they increase in steps of 100 MeV to the outermost at $W = 1.9$ GeV. In practice, the angle and momentum bite of the SOS causes the contours to be much broader. Each black box is the acceptance of a particular HMS setting (†Table 3.1). The alternate settings are offset by 1.5° and are a 4.7% increase in momentum, so that they are approximately centred on the points where the boxes join.

In addition to data taken with these kinematics, it was decided to take a smaller set of data at even higher Q^2, although the angular coverage would be incomplete. In this configuration the SOS was set with central momentum of 1.04 GeV and angle of 70 degrees, which gives a central virtual photon with $|\vec{q}| = 5.24$ GeV and angle 10.8 degrees and $Q^2 \sim 7.0$ (GeV/c)^2 at the S_{11} resonance mass. For the purposes of this thesis, the first data set will be called the 'lower-Q^2' configuration and the second data set, the 'higher-Q^2'. The kinematic settings for the experiment are summarised in Table 3.1.

Electron Arm		Proton Arm	
p_{SOS} GeV	θ_{SOS} degrees	p_{HMS} GeV	θ_{HMS} degrees
1.74	47.5	4.70	18.0, 15.0
		$4.50^{\dagger}$	19.5, 16.5, 13.5, 11.2
		3.90	21.0, 18.0, 15.0, 12.0
		$3.73^{\dagger}$	22.5, 19.5, 16.5, 13.5, 11.2
		3.24	24.0, 21.0, 18.0, 15.0, 12.0
		$3.10^{\dagger}$	22.5, 19.5, 16.5, 13.5, 11.2
		2.69	24.0, 21.0, 18.0, 15.0, 12.0
		$2.57^{\dagger}$	22.5, 19.5, 16.5, 13.5, 11.2
		2.23	21.0, 18.0, 15.0, 12.0
		$2.13^{\dagger}$	22.5, 19.5, 16.5, 13.5
1.04	70.0	4.70	11.2
		4.50	14.2
		3.90	11.2
		3.73	14.2, 11.2
		3.24	11.2

Table 3.1: The kinematic settings of the two spectrometers.

Data were taken at a mean beam current of 92 μA. The lower-Q^2 configuration was run for 6 weeks, totaling 127 C of electrons through the target from which about 50,000 η particles were identified from proton-electron coincidences, by missing mass reconstruction. Due to improved accelerator operation, the one week of running for the higher-Q^2 setting received 29 C of charge, but only about 2,000 η particles were reconstructed.

3.4 Data Analysis

The raw data as recorded by the electronics were replayed offline to produce PAW or ROOT ntuples of calibrated physics quantities. Corrections were made to the data for inefficiencies, dead times and accidental coincidences. The detector response was simulated using the Monte Carlo technique (including multiple scattering in the detector and nuclear reactions in the target walls) with one input model cross-section for the η production signal and another model for the multipion background processes, described in detail in Sec. 3.4.3. Using an iterative procedure, a linear combination of the signal and background simulations was fitted to the data and the result used to refine the simulation input model, until the simulation in each bin matched the data with a multiplicative factor of close to unity.

3.4.1 Raw Data to Physical Quantities

The raw data from each trigger was stored onto tape. These data were "replayed" offline a number of times during the analysis, using the Hall C data reduction code, as the calibration of the detectors was improved. For each event, a list of calibrated event properties including position and angles of the track, timing and energy deposition information were determined. So too were quantities for the scattering including the centre-of-mass angles, invariant hadronic mass and the missing mass. For each run an ntuple of these event parameters was produced along with a file containing scaler information and calculated efficiencies and dead times for that run.

The data were corrected on a run-by-run basis for these inefficiencies and dead times during the filling procedure—each event passing the cuts was filled into the histogram weighted by a run dependent correction factor. This included track reconstruction inefficiencies in the HMS and SOS spectrometers and computer and electronic dead times. A summary of all the corrections applied to the data is given in Table 3.2.

Effect	lower-Q^2	higher-Q^2
Proton absorption	$+4 \pm 1\%$	
†Computer DT	$+(1.0 - 19.1)\%$	$+(1.8 - 10.9)\%$
†HMS tracking	$+(2.3 - 14.3)\%$	$+(3.3 - 7.4)\%$
†SOS tracking	$+(0.3 - 0.9)\%$	$+(0.2 - 0.8)\%$
†Electronics DT	$+(0.0 - 2.4)\%$	$+(0.0 - 0.6)\%$
‡Random coincidence	$-(0.0 - 7.6)\%$	$-(0.0 - 1.2)\%$

Table 3.2: Corrections applied to the data. For corrections applied †run-by-run or ‡bin-by-bin, the range of the size is indicated in parentheses.

The pion form factor (F_π) experiment [42] was conducted in the same suite of experiments as the current experiment and this work makes reference to some analyses reported there. A detailed description of the fitting of the reconstruction matrix elements for the spectrometers is included there. A number of offsets and corrections were determined by analysing singles elastic scattering and coincident $^1H(e, e'p)$ events. From these kinematically overdetermined reactions, it was possible to check the momentum p and angles θ and ϕ (in-plane and out-of-plane relative to the spectrometer central axis respectively) for both spectrometers, and the beam energy E. A fit was done to determine what offsets to these quantities most accurately produced the required values for the invariant hadronic mass, and missing mass and energy for the elastic scattering. In the case of SOS momentum (equivalently the dipole field), there is a saturation as the current is increased due to the resistive nature of the magnets. A field dependent correction was thus determined. These offsets, summarised in Table 3.3, were used in the replay of the present data.

Quantity	HMS	SOS
θ	0.0 ± 0.5 mrad	0.0 ± 0.5 mrad
ϕ	$+1.1 \pm 0.5$ mrad	$+3.2 \pm 0.5$ mrad
p (lower-Q^2)	$-0.13 \pm 0.05\%$	$-1.36 \pm 0.05\%$
p (higher-Q^2)		$0.00 \pm 0.05\%$
E_e	$0.00 \pm 0.05\%$	

Table 3.3: Nominal 2003 spectrometer offsets [42] applied to the data during the replay phase.

Trigger Efficiency

The HMS trigger was a three out of four coincidence between the four scintillator planes. A trigger inefficiency for proton detection in the HMS is produced by protons which are not detected in their interaction with the scintillator, and by protons that do not make it through all the scintillators due to absorption.

A previous study of general HMS trigger efficiency [42] showed a strong dependence on relative particle momentum δ_{HMS}. The momentum in the spectrometers is measured relative to the central momentum p_{set}, so that particles with the same $\delta = (p - p_{\text{set}})/p_{\text{set}}$ are dispersed by the same amount. The trigger efficiency was mostly very high at 0.995 but dropped rapidly for momenta lower than $\delta \sim -6\%$. The data was analysed with a cut of $\delta > -6$ resulting in an average increase in extracted cross-section of 1.4%. No correction for this effect was made, but this figure was used as an estimate of the error due to the trigger efficiency.

The trigger requires hits in scintillator planes S1 and S2, so another source of inefficiency is absorption, through nuclear reactions, of the proton in target or detector materials before the S2 plane. The total *pp* collision cross-section, σ_{pp}, varies slightly from 47 to 42 mb for proton lab momenta between 2 to 5 GeV/c [70] which is the momentum range of this experiment. Therefore for this experiment, the trigger efficiency due to absorption is relatively independent of kinematic setting.

The primary sources of interacting material are the S1 scintillator planes which had a thickness of 1 cm each and the Aluminum windows of the gas Čerenkov and aerogel detectors which had a total thickness of 0.51 cm. The proton-nuclear cross-section was estimated as $A^{0.7}\sigma_{pp}$. Combining interactions in all material, the trigger efficiency due to proton absorption is estimated to be 0.95.

To calculate the correction used in the experiment for the trigger efficiency due to proton absorption, a study of *ep* elastic events was done. The SOS was set for electrons at central angle = 50° and central momentum of 1.74 GeV/c and the HMS was set for protons at central angle of 18° and central momentum of 4.34 GeV/c at a beam energy of 5.247 GeV. For a point target, the SOS has an out-of-plane angular acceptance of ±37 mr and an in-plane angular acceptance of ±57 mr (the in and out-of-plane angles are relative to the central axis of the spectrometer), while the HMS has an out-of-plane angular acceptance of ±70 mr and an in-plane angular acceptance of ±27 mr. The ratio of electron to proton momentum is 0.4, so for the maximum SOS out-of-plane angle, the corresponding HMS out-of-plane angle is 15 mr. The maximum SOS in-plane angle gives a corresponding HMS in-plane angle of 23 mr. The data acquisition is set-up to accept singles triggers from the SOS and HMS individually in addition to coincidence triggers between the HMS and SOS.

In offline analysis, the cuts described in Sec. 3.4.2 were used to identify electrons in the SOS. A good elastic event in the SOS was identified by a cut of $0.9 < W < 1.0$ GeV and a cut on the SOS in-plane angle of ± 50 mr which ensured that the proton would be within the HMS angular acceptance. The proton was selected by the time-of-flight between electron and the particle detected in the HMS. The raw number of coincident *ep* events was 2009 and the number of single events was 205.

Some data were taken with an aluminium "dummy" target, which is intended to model an empty target cell, but is 7.78 times thicker in order to increase the count rate. Analysis of this data determined that the target endcaps would contribute 12 ± 3 events to the raw coincidence events and 123.0 ± 12 events to the raw single events. Therefore the proton trigger efficiency due to absorption is 0.96 ± 0.01, in good agreement with the prediction. A 4% correction was applied to the data for this effect.

Calibration of Simulation Resolution

The elastic scattering of electrons into the SOS and protons into the HMS was compared to SIMC Monte Carlo simulations of the same. The invariant mass determined from elastic scattering must be the proton mass, but is broadened due to resolution effects and radiative tails—which are included in the simulation. In both detectors it was found that the width of this peak predicted by the simulation was narrower than for the data. These resolution differences were taken into account by altering the drift chamber resolutions in each spectrometer, from the nominal value of 300 μm.

The resolution was varied, and the simulation repeated, until a Gaussian fitted to the simulated spectrum had the same width as a Gaussian (and polynomial background) fitted to the data. It was found that the HMS needed a drift chamber resolution of 570 μm to match the data width of 17.2 MeV, while in the SOS, the 30.1 MeV width was achieved with a 350 μm resolution.

This method had the effect of degrading the optics of the simulation slightly to match the experimental transport matrix elements of the data, in a logical yet simple manner. Importantly, it was found that this procedure brought the missing mass distribution predicted for the coincident measurement of the $e(p, e'p)\eta$ process into better agreement with the data. During the systematic error analysis process, the drift chamber resolutions were varied by 10% in order to determine the effect that this would have on the extracted differential cross-sections and amplitudes, Section 3.4.6.

Collimator Punch Through

A source of background is due to particles that interact with the edges of the HMS collimator aperture, located just before the first quadrupole magnet, whose kinematics are thus changed. The collimator is made from 6.35 cm thick HEAVYMET (machinable Tungsten with 10% CuNi; density=17 g/cm^3.) For practical purposes electrons are stopped by the SOS collimator, but protons have the possibility of "punching" through the collimator, undergoing multiple scattering and energy loss in the material, and still making it through the spectrometer to the detectors. This process is modelled in the simulation of the experiment and additionally a loose cut, 3 centimeters outside the collimator edge, is used to eliminate unphysical reconstructions.

Data Cuts

The 'standard' cuts are listed in Table 3.4. The cuts on relative electron momentum δ_{SOS}, and relative proton momentum δ_{HMS}, are made to ensure that only particles within the well understood region of the spectrometer momentum acceptance are used. The momentum in the spectrometers is measured relative to the central momentum p_{set}, so that particles with the same $\delta = (p - p_{\mathrm{set}})/p_{\mathrm{set}}$ are dispersed by the same amount.

Some parts of the SOS spectrometer acceptance, due to an ambiguity in the solution of the optics equations, do not reconstruct reliable tracks. The cuts on the SOS focal plane position in the magnet dispersion direction, $X_{\mathrm{SOS,f.p.}}$, are to eliminate these regions. The particle identification cuts are described in Section 3.4.2.

Binning

The data were binned in W, $\cos\theta^*_\eta$, ϕ^*_η and m_x^2, where W is the invariant mass of the hadronic system, θ^*_η is the polar angle between the direction of the η and the three-momentum transfer vector $\vec{q}$ in the centre-of-mass of the resonance, ϕ^*_η is the azimuthal angle of the η with respect to the electron scattering plane, and m_x^2 is the square of the missing mass for $p(e, e'p)x$.

For the lower-Q^2 data, this was done in 12 $\cos\theta^*_\eta$-bins and 8 ϕ^*_η-bins, to maximise the angular resolution for partial-wave analyses, necessitating m_x^2-bins of 0.1 GeV^2 and W-bins of 30 MeV near the resonance and 40 MeV at higher W. The higher Q^2 data, with far fewer detected particles, was binned with W-bins of 30 MeV, 6 $\cos\theta^*_\eta$-bins, 5 ϕ^*_η-bins and m_x^2-bins of 0.15 GeV^2.

Quantity	Variable		Cut
Electron momentum	δ_{SOS}	$<$	$+20\%$
		$>$	-15%
Proton momentum	δ_{HMS}	$<$	$+9\%$
		$>$	-9%
SOS focal plane position	$X_{\mathrm{SOS,f.p.}}$	$>$	-20 cm
dispersive direction		$<$	$+22$ cm
†Coincidence time	$\lvert t_{\mathrm{coin}} - t_{\mathrm{cent}} \rvert$	$<$	1.5 ns
†SOS Čerenkov	$N_{\mathrm{p.e.}}$	$>$	0.5
†SOS calorimeter	E_{norm}	$>$	0.7

Table 3.4: The set of 'standard' cuts applied to the data and to the simulations where applicable. †The Particle Identification cuts are not applied to the simulation.

Bins in (W, cosθ^*_η, ϕ^*_η) were retained for the analysis if they passed the following three criteria. Firstly, in the region of the η missing mass peak, the simulation was required to predict a signal to background ratio of at least 0.25. Secondly, the simulation needed to have predicted a minimum average number of η events in the peak of 1.5 per missing mass squared channel. This criterion was used instead of requiring a total number of predicted η particles because the resolution of the missing mass peak changes substantially with cosθ^*_η. The third criterion for acceptance was, following the subtraction of the all the backgrounds, the sum of the data in the region of the missing mass peak was required to have a statistical uncertainty of less than 50%.

3.4.2 Particle Identification

Electron Identification

In the SOS spectrometer, the Čerenkov detector and the electromagnetic calorimeter were used to identify electrons and reject pions. The Čerenkov detector was filled with Freon-13 at 1 atmosphere, yielding a velocity threshold of $\beta_t = 1/n = 0.9992$. The highest momenta detected by the SOS in this experiment was about 2.09 GeV/c, corresponding to $\beta = 0.9978$ for pions, which is below the threshold for detection while all electrons are well above the threshold. Some pions make small signals in the Čerenkov due to scintillation or "knock-on" electrons from atomic scattering. The detected signal was calibrated into units of the number of photo-electrons, $N_{\text{p.e.}}$.

For each event, the signals from each of the 44 lead-glass blocks in the calorimeter were summed to obtain the total energy deposited, E_{tot}. This energy was then normalised by the momentum of the particle as determined by the tracking, p_{track}, to obtain $E_{\text{norm}} = E_{\text{tot}}/p_{\text{track}}$. The 16 radiation lengths of lead-glass bring electrons to a stop, resulting in a peak at $E_{\text{norm}} \sim 1$ due to electrons. The pions peak at about $E_{\text{norm}} \sim 0.25$, but have a long tail to higher E_{norm} due to the charge exchange nuclear interaction $\pi^- p \to \pi^0 n x$, and subsequent decay $\pi^0 \to \gamma\gamma$.

Figure 3.6 shows the correlation between E_{norm} and $N_{\text{p.e.}}$ for the lower-Q^2 data. The electrons are clearly well separated from the pions by these two detectors. In the analysis, electrons are identified using two simple cuts, $N_{\text{p.e.}} > 0.5$ and $E_{\text{norm}} > 0.7$, shown in the figure.

Proton Identification and Accidental Coincidence Subtraction

Protons were separated from pions using time of flight considerations. The raw difference in arrival times, t_{diff}, between the electron in the SOS and the

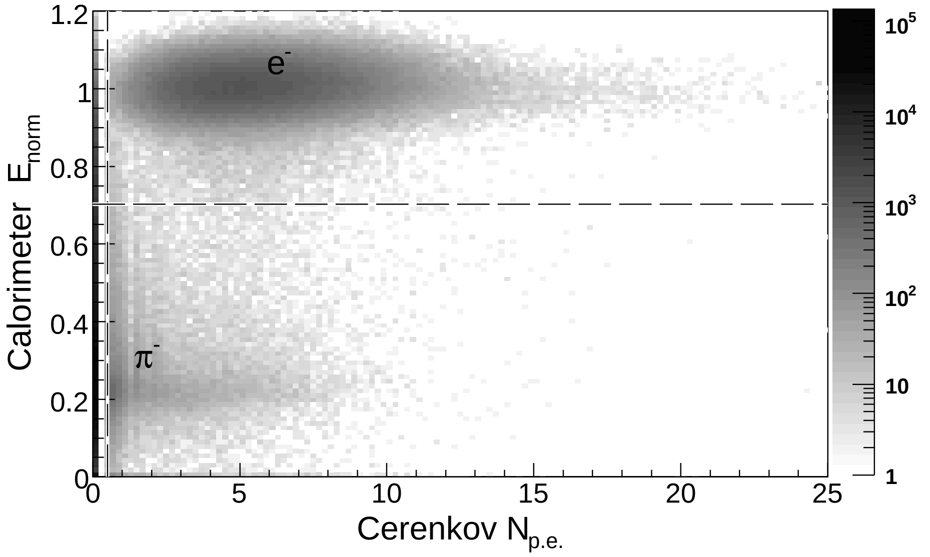

Figure 3.6: The correlation between E_{norm} and $N_{\text{p.e.}}$ for all the lower-Q^2 data. The particle ID cuts to select electrons, $N_{\text{p.e.}} > 0.5$ and $E_{\text{norm}} > 0.7$, are visible as dashed lines in the figure. All other cuts listed in Table 3.4 have already been applied to the data.

positive particle in the HMS, were corrected event-by-event for differences in path length of both particles through the detectors and the variation in velocity β of the positive particle (all electrons having essentially the same velocity.) This corrected coincidence time, t_{coin}, is plotted in Fig. 3.7 and shows peaks due to protons and π^+ particles and a background of accidental (or random) coincidences.

The path taken is determined by the tracking algorithm from drift chamber hit positions while the velocity $\beta = (p^2/(m_p^2 + p^2))^{1/2}$ is calculated from the measured momentum p assuming the proton mass m_p. For protons the corrected coincidence time depends only on the actual difference in starting times of the particles in the target, causing a peak of real coincidences, which has been shifted to zero in the figure. Particles with a different mass, such as pions, have their coincidence time peak shifted relative to the protons since for the same momentum, they have a different velocity. The π^+ peak is broader than the proton peak because t_{coin} is calculated to remove the momentum dependence of the protons but the pion locus remains momentum dependent. A much smaller number of kaons are detected and form a locus between the pions and protons, but remain distinctly separable. It was then possible to select the proton events and reject the pion and kaon events and most of the accidental coincidences using one simple cut.

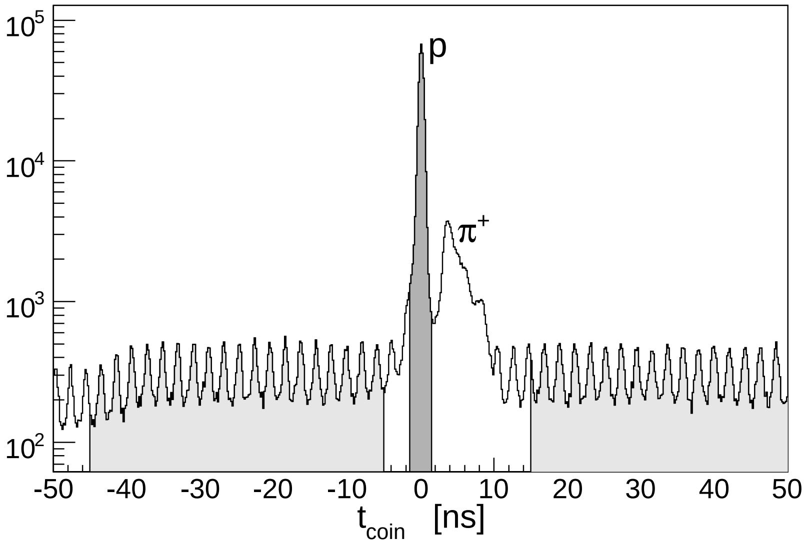

Figure 3.7: Coincidence time spectrum for the lower-Q^2 data with all of the ‘standard’ cuts except the coincidence time cut. The dark grey shaded region represents the 3 ns wide proton cut. The 2 ns beam structure is clear in the accidental background. Data from the light grey shaded regions was used to estimate the amount of accidentals in each (W, cosθ^*_η, ϕ^*_η and m^2_x) bin under the proton peak.

Accidental coincidences occur when both detectors are triggered within the 100 ns coincidence time window, but the detected particles originate in different scattering events. In the coincidence time spectrum of Fig. 3.7, the accidentals are the continuous background under the two main peaks. The 2 ns beam structure can clearly be seen in the spectrum. A 3 ns particle identification window was used to select protons, but within this cut there is still some background due to accidental coincidences which must be subtracted.

For each bin in 4 dimensions (W, $\cos\theta^*_\eta$, ϕ^*_η and m^2_x), the number of accidental coincidences inside the proton cut was estimated by determining the average number of accidentals in the "wings" of the spectrum, -45 ns $< t_{\mathrm{coin}} < -5$ ns and 15 ns $< t_{\mathrm{coin}} < 50$ ns, away from loci for actual coincidences. This value was then normalised for the width of the proton cut and subtracted from the data. The accidental correction is small for our kinematics and rates, the weighted mean correction was 1.5% and the largest correction in any (W, $\cos\theta^*_\eta$, ϕ^*_η) bin was 7.6%.

η Identification

In the case of inelastic scattering, the detection of the scattered electron and recoil proton is not an exclusive measurement—there will be at least one other emitted particle. If there is only one undetected particle it is possible to fully reconstruct the kinematics of that particle. The data corresponding to such a channel, the $p(e,e'p)\eta$ in this case, is isolated by constructing the square of the missing mass m^2_x, as given in Eq. (3.1). Figure 3.8 shows the m^2_x distribution for the lower-Q^2 data, with the π^0, η and ω products are visible as peaks. The actual extraction of the η particles is done by applying a cut on m^2_x around the η peak and subtracting the background.

The resolution of this peak varies as a function of cosθ^*_η and therefore so does the cut, which is listed in Table 3.5 for the lower-Q^2 data. The higher-Q^2 data has very little coverage above cos$\theta^*_\eta = 0$ at any W, and larger m_x^2 bins, so the cut was kept at a constant 0.255 GeV$^2 < m_x^2 < 0.36$ GeV^2.

The continuous background, seen in Fig. 3.8, is due to events with more than one undetected particle. In this case, the missing mass does not correspond to any physical mass because the magnitude of the missing momentum is smaller than the sum of the magnitudes of the individual momenta of the undetected particles. This effect, predominantly due to the production of multiple pions, is the principle background in this experiment, and is treated in Section 3.4.3.

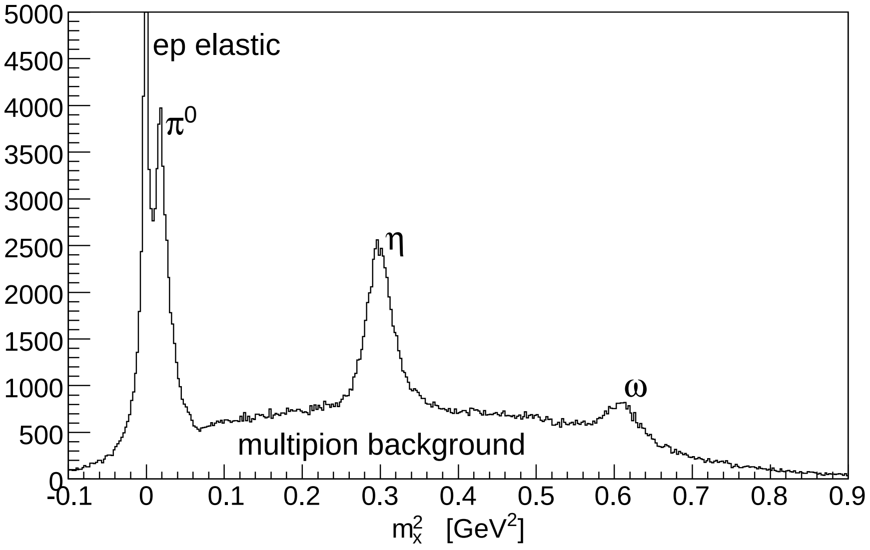

Figure 3.8: Missing mass squared m_x^2, from Eq. (3.1), for all the lower-Q^2 data.

$\cos\theta^*_\eta$	-0.917	-0.750	-0.583	-0.417	-0.250	-0.083
m_x^2 min (GeV^2)	0.27	0.27	0.27	0.26	0.26	0.25
m_x^2 max (GeV^2)	0.34	0.35	0.35	0.36	0.36	0.37

$\cos\theta^*_\eta$	0.083	0.250	0.417	0.583	0.750	0.917
m_x^2 min (GeV^2)	0.25	0.25	0.25	0.25	0.25	0.25
m_x^2 max (GeV^2)	0.37	0.38	0.38	0.39	0.39	0.39

Table 3.5: The m_x^2 cuts used in each $\cos\theta^*_\eta$ bin for the lower-Q^2 data.

3.4.3 Monte Carlo Simulation of the Experiment

The Monte Carlo simulation of the experiment was done with SIMC [88], the Jefferson Lab Hall C in-house detector simulation package. The simulation includes detailed models of both magnetic spectrometers and simulated the effects of radiative processes, multiple scattering, and ionisation energy loss (due to material in the target and spectrometers). It was used to obtain the experimental acceptance and radiative corrections for the resonance process under study, to simulate the multipion background to the resonance production and to study a number of other processes serving to verify our understanding of the apparatus.

SIMC as a package consists of an event generator, which is able to produce events from a variety of physical scattering processes common in Hall C or from phase space, and two ‘single arm’ spectrometer models, one for each detector, to track the particles and determine whether they are accepted by the detector. In each spectrometer model, the particle is propagated from its initial position in its initial direction with transport maps produced by COSY Infinity [89], an arbitrary-order, beam dynamics simulation and analysis code, using the results of a field map of the magnetic elements. At points where there are apertures in the spectrometer such as collimators or the magnets themselves, the positions of the particles are checked against these. For the magnets this is done at the entrance, exit and at the maximum beam envelope within the object. Particles making it into the detector hut underwent multiple scattering and energy loss in the air and other materials. Particles that did not conform to the experimental trigger, such as passing through three of the scintillator hodoscopes, and for electrons the Čerenkov and calorimeter, were considered undetected. Detected events were reconstructed back to the target using the COSY optics matrix.

SIMC was not used ‘out of the box’ for the present analysis, as it did not have physics models for either the p(e,e’p)η process or for multiple pion production. For η production, a simple model of the S_{11} resonance was added to SIMC, which was then run to simulate the signal part of the experiment. In the case of the multi-pions, another event generator was used and the resulting electron and proton pairs were propagated through the SIMC detector models to simulate their detection.

For both of the two Q^2 configurations, the data are taken in “settings” for which the HMS spectrometer angle and momentum is fixed. To limit file sizes and aid in online checking of the data, the data in each setting is taken in a number of “runs”. The simulation is performed on a run-by-run basis to match the data. The data and simulation are then binned into identical four-dimensional histograms.

Model for p(e,e'p)η

The model for η production used in the simulation and extraction of the cross-section is a single relativistic Breit-Wigner shape as a function of W multiplied by a exponential form factor depending on Q^2. The form used for the Breit-Wigner resonance shape (from Christy and Bosted [90]) is given by

$$\begin{aligned} \mathrm{BW}(W) &= \frac{K_R K_R^{cm}}{K(W)K^{cm}(W)} \cdot \\ &\quad \cdot \frac{\Gamma^{\mathrm{tot}}\Gamma^{\gamma}}{\Gamma\left[(W^2 - W_R^2)^2 + (W_R\Gamma^{\mathrm{tot}})^2\right]}, \end{aligned} \tag{3.14}$$

where the equivalent photon energy in the lab frame is

$$K(W) = \frac{(W^2 - m_p^2)}{2m_p},$$

the equivalent photon energy in the center of mass (CM) frame is

$$K^{cm}(W) = \frac{(W^2 - m_p^2)}{2W},$$

and K_R and K_R^{cm} represent the same quantities evaluated at the mass of the S_{11} resonance, W_R. Γ^{tot} is the full decay width defined by

$$\Gamma^{\mathrm{tot}} = \sum_j \beta_j \Gamma_j, \tag{3.15}$$

with β_j the branching fraction to the j$^{\mathrm{th}}$ decay mode and Γ_j the partial width for this decay mode. The partial widths are determined from the intrinsic widths Γ, using

$$\Gamma_j = \Gamma \left[\frac{p_j^{cm}}{p_j^{cm}|_{W_R}}\right]^{2L+1} \cdot \left[\frac{(p_j^{cm})|_{W_R}^2 + X^2}{(p_j^{cm})^2 + X^2}\right]^L, \tag{3.16}$$

where the p_j^{cm} are meson momenta in the center of mass, L is the angular momentum of the resonance, and X is a damping parameter. The model as used in the simulation is then given by

$$\frac{d\sigma}{d\Omega_\eta^*} = \frac{1}{4\pi} a e^{-bQ^2} \cdot \mathrm{BW}(W). \tag{3.17}$$

Although simplistic, the model describes the data well. The parameters a and b were obtained by fitting the form ae^{-bQ^2} to the cross-section at the S_{11} resonance mass, σ_R, of data taken by Armstrong *et al.* [63] and both of the present Q^2 data sets. The parameters W_R and Γ_R were refined using an iterative procedure in which the Breit-Wigner form was fitted to the angle-integrated lower-Q^2 data, used to extract a new cross-section and then refitted. There was no explicit $\cos\theta^*_\eta$ or ϕ^*_η dependence in the input model since the data showed very little anisotropy. The final model parameters are given in Table 3.6.

Parameter	Value
a	9.02 nb
b	-0.479 (GeV/c)$^{-2}$
W_R	1525 MeV
Γ_R	133 MeV
X	0.165 GeV

Table 3.6: The parameters of the S_{11} resonance-dominated cross section model used for the final data extraction.

Model for Multipion Production

The multipion background was simulated using an event generator from the Jefferson Lab Hall B (CLAS detector) simulation package, which takes as input the Q^2 and W^2 ranges of the generation region and the reactions, chosen from a list of possibilities, from which the events should be generated. Depending on the reaction, the events are then sampled from interpolated data tables or according to a cross-section model—in contrast to SIMC behaviour which throws events uniformly and weights them event-by-event.

The generator itself extrapolates the cross-section from where data exists to higher Q^2 using the square of the dipole form, $(1 + Q^2/0.71)^{-4}$. The reactions included in our simulation of the multipion background are given by Eqs. (3.18) and (3.19).

$$e + p \rightarrow \quad e' + p + \pi^+\pi^- \qquad \text{(model)} \tag{3.18}$$

$$\begin{aligned} e + p \rightarrow &\quad e' + p + \pi^+\pi^-\pi^0 \\ e + p \rightarrow &\quad e' + p + \pi^+\pi^-\pi^+\pi^- \qquad \text{(tables)} \\ e + p \rightarrow &\quad e' + p + \pi^+\pi^-\pi^+\pi^-\pi^0 \end{aligned} \tag{3.19}$$

The event generator was developed from an initial version for real photons [91]. In that version, for performance reasons, the cross-section is drawn from tabulated data—either measured or generated from models in unmeasured regions. In the current version, the $p\pi^+\pi^-$ exit channel, Eq. (3.18), is now generated according to a phenomenological model [92], with parameters that have been fit to recent CLAS data [93] which measured the process $ep \rightarrow e'p\pi^+\pi^-$ for $1.4 < W < 2.1$ GeV and $0.5 < Q^2 < 1.5$ GeV$^2/c^2$. The model is calculated for the three intermediate channels $\pi^-\Delta^{++}$, $\pi^+\Delta^0$ and ρp. The amplitude is defined in the meson-baryon degrees of freedom, and is therefore not necessarily valid at this high momentum transfer $Q^2 \lesssim 7$ (GeV$/c)^2$, where quark-gluon degrees of freedom may be the most appropriate. Radiative corrections are not implemented for the multipion model. Despite these last two points, the results obtained are good enough to justify our implementation here. The properties of the generated pions are not used, just the electron and proton pairs are propagated through SIMC.

Multipion Background Subtraction

As can be seen in Fig. 3.8, the peak at $m_x^2 \sim 0.3$ GeV^2, corresponding to missing η particles, lies on a continuous background described in Sec. 3.4.2. This background was treated by simulating the m_x^2 spectra of the background using SIMC with a model of the largest contributing reactions, described in the previous section, and then subtracting the simulation from the data.

The output of the simulation was a large set of multipion events that are accepted into our detectors. These events are then filled into histograms of the same structure as those of the data, yielding our approximation to the shape of the multipion background, without an absolute normalisation. Since an absolute multipion cross-section is not being extracted, the shape is sufficient to subtract it from the data

The simplest way to normalise the background to the data is with a two-parameter fit in each (W, cosθ^*_η, ϕ^*_η) bin. The m_x^2 spectra of the multipion background simulation and the η production simulation would have been normalised to minimise the χ^2 difference between their sum and data m_x^2 spectrum. In practice, due to diminishing acceptance, the out-of-plane ϕ^*_η bins demonstrate a phenomenon where the multipion background simulation and the η production simulation can have m_x^2 spectra similar enough to make a two-parameter fit unreliable. This is typically the case for mid to large cosθ^*_η and worsens as W increases. An example of such a case is illustrated in Fig. 3.9.

For this reason, the fit was constrained to have the multipion normalisation parameter constant over ϕ^*_η, as expected physically. For each and all of the (W, cosθ^*_η) bins, the fit had 9 parameters: one for the single multipion normalisation over all the ϕ^*_η bins and one for η production in each of the

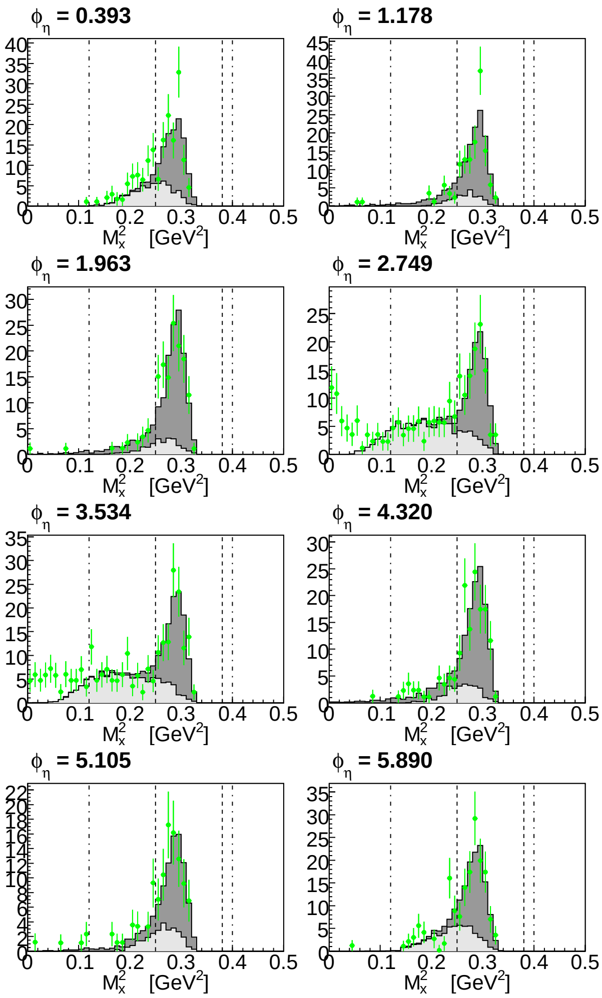

Figure 3.9: (Colour online) The ϕ_η dependence of missing mass squared distributions for $W = 1.5$ GeV and $\cos\theta^*_\eta = 0.416$. The (green) points are the data, while the simulation of the multipion background is the light grey filled histogram and η production simulation has the darker grey fill. The dot-dashed lines shows the region within which the background fit is done while the dashed lines show the region within which the η cross-section is extracted. Panels with $\phi_\eta = 1.178$, 1.963, 4.320, and 5.105 are the out-of-plane ϕ bins where the simulations of the signal and background are sufficiently similar to make a two-parameter bin-by-bin fit unreliable.

eight ϕ^*_η bins. The production of π^0 particles, seen as a peak at $m_x^2 \sim 0.02$ GeV^2 in some panels of Figs. 3.9 and 3.11, produces a radiative tail which, in principle, extends under the η peak. The size of this effect is smaller than the uncertainty in the multi-pion background, and so was neglected.

This approach does a good job of reproducing the shape of the measured m_x^2 spectra. By eye, the sum of the normalised simulations seem to match the data well and in 94% of bins have a reduced χ^2 of less than 2. A few representative spectra showing the W and cosθ^*_η dependence of the m_x^2 distributions are shown in Figs. 3.10 and 3.11 respectively. The uncertainty in the normalised background simulation was determined by adding the small Monte Carlo statistical uncertainty to the Minuit [94] fit uncertainty on the normalisation parameter in quadrature.

It should be noted that some structure is seen within the normalisation parameters of the background model in W and cosθ^*, illustrated in Figs. 3.12 and 3.13 respectively. The extracted fit parameters seem to rise smoothly and approximately linearly with both increasing W and increasing cosθ^*. This is understandable since the multipion background model is produced from data with much lower Q^2. Overall, the variation in the parameters is about a factor of 4.

Target Window Background

No explicit subtraction for scattering off the aluminium walls of the target was performed. The data taken with the dummy target in this experiment has too low statistics to be used for subtraction, and it was not taken at all of the experimental settings, but it is adequate for estimating the yield from the target walls and demonstrating the shape of the missing mass distribution.

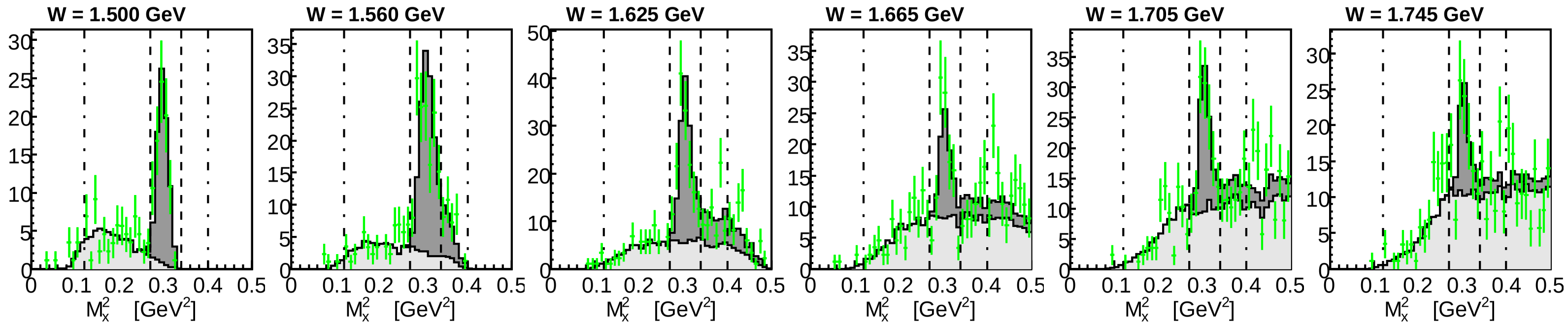

Figure 3.10: (Colour online) The W dependence of missing mass squared distributions for $\cos\theta^*_\eta = -0.916$ and $\phi = 3.534$ radians. Symbols as in Fig. 3.9.

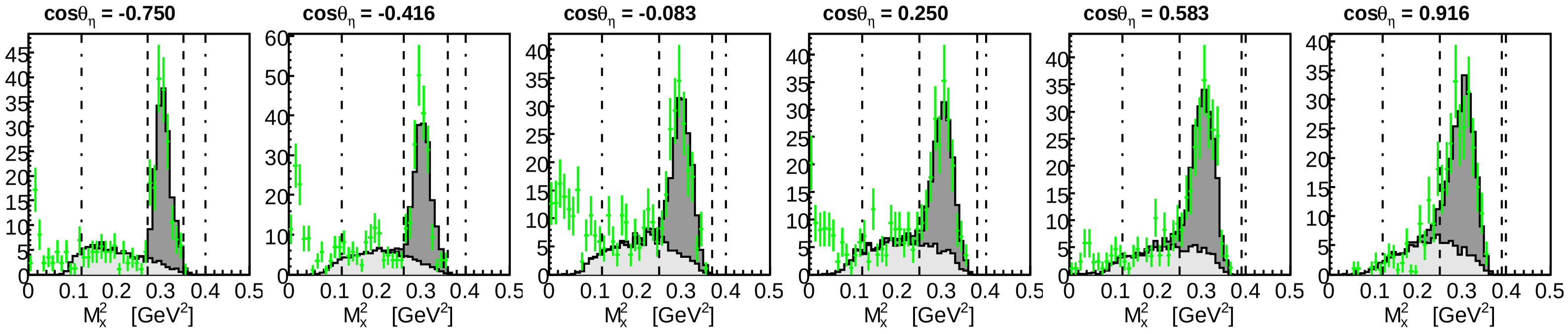

Figure 3.11: (Colour online) The $\cos\theta_\eta^*$ dependence of missing mass squared distributions for $W = 1.5$ GeV and $\phi = 3.534$ radians. Symbols as in Fig. 3.9. The vertical dashed lines, which show the region within which the η cross-section is extracted, vary with $\cos\theta_\eta^*$ to accommodate the changing resolution.

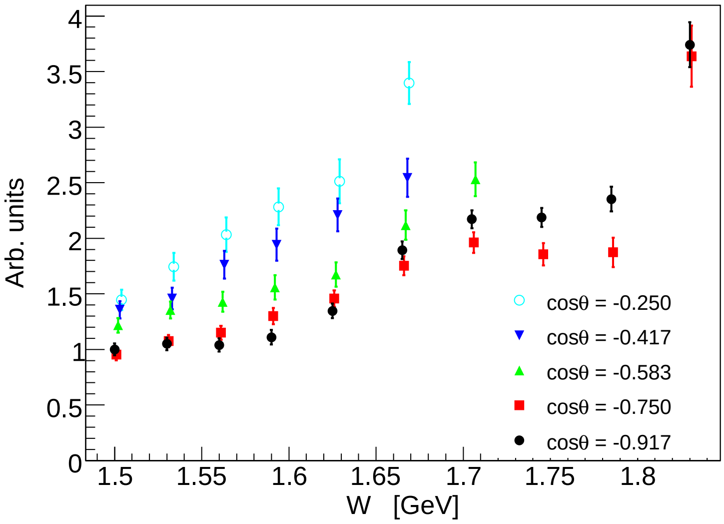

Figure 3.12: (Colour online) The W dependence of the normalisation coefficient of the multipion background simulation.

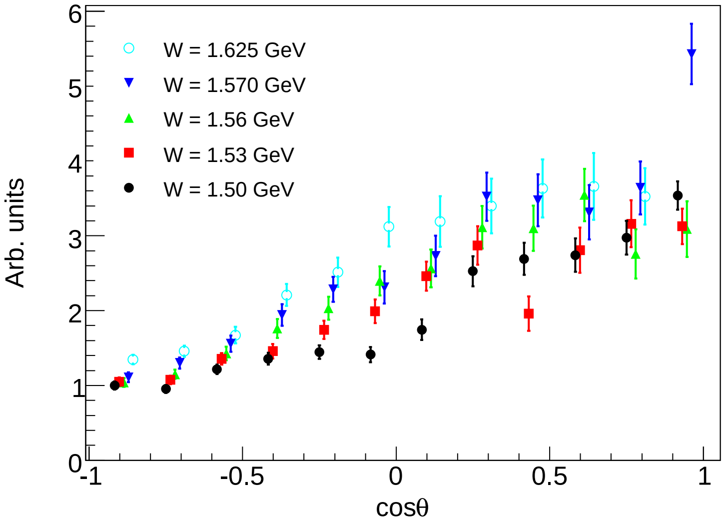

Figure 3.13: (Colour online) The $\cos\theta^{*}$ dependence of the normalisation coefficient of the multipion background simulation.

The size of the target wall effect is small and it has a very similar shape to the multipion background, so it is therefore adequately accounted for in that background subtraction procedure. To first order, a nucleus is a bag of nucleons, and as such the multipion production from the aluminium target window has the same broad kinematic distribution as from a free proton—the following analysis confirms this.

The dummy target produced 430 coincidences from a beam charge of 1.97 C giving an average yield, integrated over all angles and W up to 1.7 GeV, of about 0.2 counts per mC. The hydrogen target's 64,000 multipion coincidences, estimated from the background subtraction procedure, came at about 0.6 counts per mC, or three times as fast. Taking into account the differences in thickness between the dummy and the actual target walls, the multipion background is expected to have produced at least 20 times more background events than the target walls. Figure 3.14 shows the similarity between missing mass spectra of the dummy data and the multipion background simulation in three W bins.

Radiative Corrections

Radiative effects occur because photons are emitted in the interaction of the incoming and outgoing charged particles of the scattering. These real photons are either produced within the field of the scattering nucleus itself, called internal radiation, or from the fields of other nuclei in the propagation medium, called external radiation. This radiation causes there to be a difference between the actual momenta of the particles at the scattering vertex and the detected momenta, leading to measured values of W, Q^2 and the c.m. angles $\cos\theta^*_\eta$ and ϕ, different from that of the actual scattering. In order to extract meaningful information from the detected particles, this

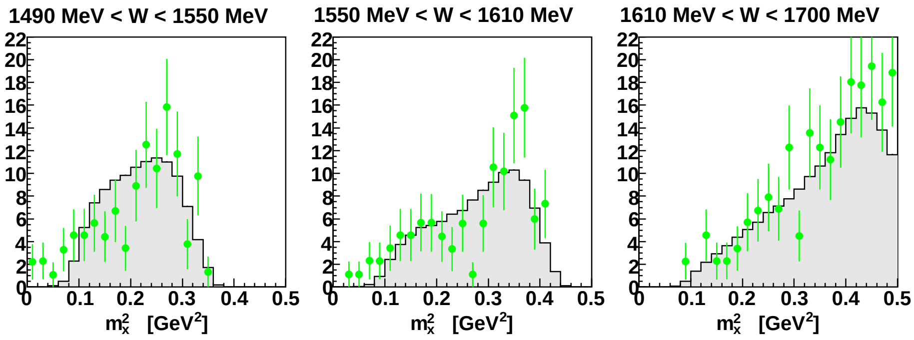

Figure 3.14: (Colour online) The (green) points are the m_x^2 distribution of the full set of data off the "dummy" target cell, and the grey filled histogram is the simulation of multipion background from Hydrogen. The simulation is arbitrarily normalised to match the data, with the same factor in all three panels. Note the similarity in shape.

radiative contribution must be corrected for.

External radiation is small for the proton due to its high mass and can be handled essentially exactly for the electron, both pre and post-scattering. Dealing with internal radiation requires a knowledge of the coupling of the photon to the electron, which is well known, and to the proton, which is not known analytically since it depends on its QCD structure. It is then further complicated by interference of the amplitudes for radiation from each of the particles of the scattering. The radiative corrections for this experiment are done within SIMC, with the formalism of Ref. [95], which is a general framework for applying radiative corrections in $(e, e'p)$ coincidence reactions at GeV energies. This approach uses the angle peaking approximation and takes into account higher-order bremsstrahlung effects, multiple soft photon emission and radiation from the scattered hadron. External radiation is also included in the model.

The size of the radiative corrections implemented by SIMC is determined by running the full simulation with and without including radiative effects. In each bin, the ratio of the number of events predicted by these two simulations, after the 'standard' cuts of Table 3.4 and the missing mass cuts of Sec. 3.4.2, gives a number equivalent to the correction factor required to take account of the radiative effects. This radiative correction factor is listed for each bin in Tables C.1 and C.2 along with the extracted cross-sections. Using these values and the size of the missing mass cuts given in Sec. 3.4.2 one can remove the effect of the radiative corrections on the cross-sections.

The correction factor is plotted for the lower-Q^2 configuration as a function of ϕ for different W bins and three cosθ^*_η ranges in Figs. 3.15, 3.16 and 3.17. The points are plotted for the kinematic bins where the data are sufficient to extract a cross section. Much of the large kinematic dependence in these plots comes about due to the limited acceptance, which decreases with increasing W and cosθ^*_η.

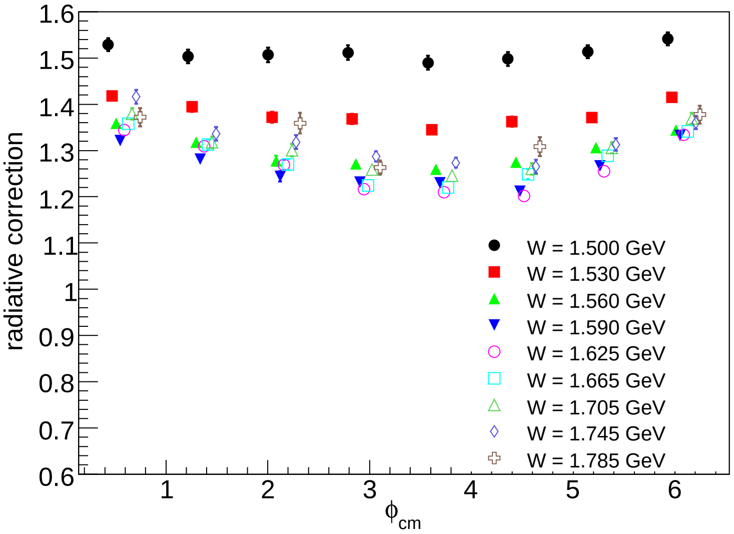

Figure 3.15: (Colour online) Radiative corrections for -1 < cosθ_η < -$\frac{1}{3}$. Uncertainty is due to Monte Carlo statistics only.

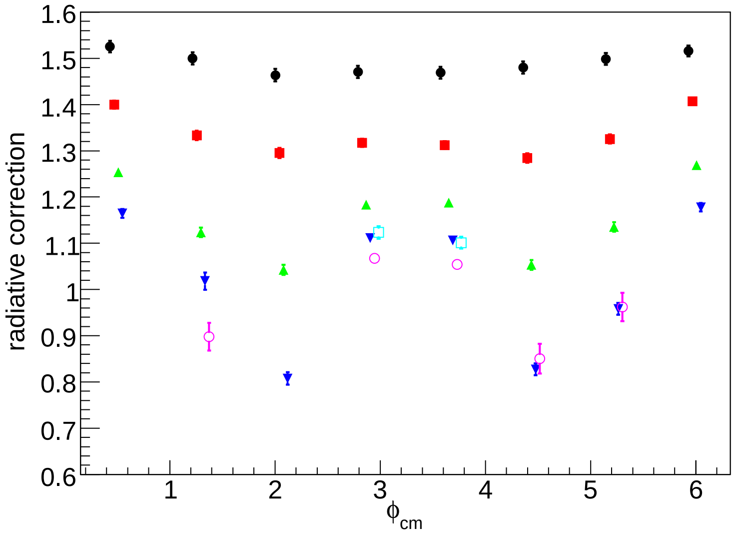

Figure 3.16: (Colour online) Radiative corrections for -$\frac{1}{3}$ < cosθ_η < $\frac{1}{3}$. Uncertainty is due to Monte Carlo statistics only. Symbols as in Fig. 3.15.

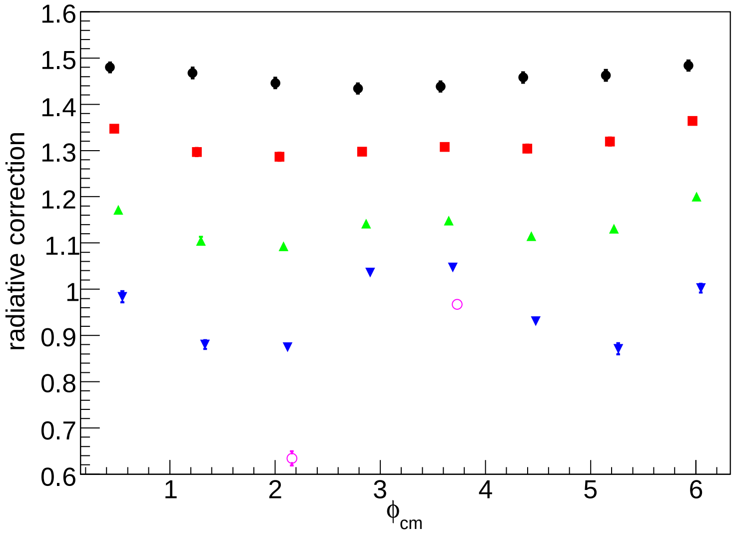

Figure 3.17: (Colour online) Radiative corrections for $\frac{1}{3}$ < cosθ_η < 1. Uncertainty is due to Monte Carlo statistics only. Symbols as in Fig. 3.15.

This approach does neglect 2-photon radiation, which is expected to be about a factor of $\alpha = 1/137$ smaller, and makes the "extended peaking" approximation, the "soft photon" approximation and neglects contributions from excited hadronic states. The uncertainty in the radiative corrections was estimated to be 2%.

3.4.4 Extraction of the η Differential Cross-Section

The actual η cross-section extraction is done by comparing the data, having had the randoms and multi-pion background already subtracted, with a Monte Carlo simulation of the experiment, produced using SIMC and the η production model described previously. The comparison is done for each (W, cosθ^*_η, ϕ^*_η) bin. The m_x^2 dependence of both the subtracted data and the simulation is integrated out between two tight limits in m_x^2 that contain the missing η particle peak

$$N^i = \sum_{j_{\mathrm{low}}}^{j_{\mathrm{high}}} N^{ij},$$

where i labels the $(W, \mathrm{cos}\theta^*_\eta, \phi^*_\eta)$ bins and j labels the m_x^2 bins so that N^{ij} is the content of a certain $(W, \mathrm{cos}\theta^*_\eta, \phi^*_\eta, m_x^2)$ bin. The number of simulation events, N^i_{MC}, is obtained by multiplying the yield output of SIMC, in counts per mC, by the integrated beam current and then using the same filling procedure.

As can be seen in Fig. 3.11, the resolution of the experiment, and therefore the width of the η peak, depends on cosθ^*_η. The integration limits, j_{low} and j_{high}—the dashed lines in the figure, are also functions of cosθ^*_η. The dependence of the extracted cross-sections on these integration limits is accounted for in the next section. The experimental cross-section is then obtained, from the model cross-section at the centre of the bin σ^i_{MC}, using

$$\sigma^i_{\text{data}} = \frac{N^i_{\text{data}}}{N^i_{\text{MC}}}\sigma^i_{\text{MC}}. \tag{3.20}$$

As with any measurement in which the events are histogrammed, each bin represents a mean quantity, weighted by the distribution of the events within that bin. In this experiment the cross-section changes rapidly and non-linearly with W, especially going from threshold to maximum within just 50 MeV, and our W bins are rather large at 30 MeV.

The bin centering in W was done implicitly during the cross-section extraction, under the assumption that the relativistic Breit-Wigner model and SIMC are accurate representations of the physics and detector response. If the simulation experimental acceptance model is accurate, the kinematic distribution of simulated particles in each bin will mimic the population of data events within that bin. So too if the physics model is good, then nonlinearities in the actual cross-section will be correctly reproduced by the simulation. To the extent that both of these are true, the ratio of the data and Monte Carlo yields in each bin, $N^i_{\text{data}}/N^i_{\text{MC}}$, directly connects the number of detected particles with the input Monte Carlo model, σ^i_{MC}. The bin centring is then done by evaluating the simulation input model at the bin centre.

The bins in $\cos\theta^*_\eta$ and ϕ^*_η are quite small, and where there is full coverage, the extracted differential cross-sections are largely flat. It was decided not to attempt to incorporate nonlinear variation of the angular cross-section into the input model, and thus no implicit bin centering takes place.

The results are not quoted at fixed Q^2. Since the events in every bin have a Q^2 distribution, the cross-section results are an average over the Q^2 distribution of the bin. The weighted average Q^2 of events in each bin $\langle Q^2_{\text{bin}}\rangle$, is therefore quoted along with the extracted cross-section in Tables C.1 and

C.2. In order to quote all the data at a single value of Q^2, a model dependent correction would have to be applied to the data, which can be done at a later stage.

3.4.5 Check of SOS acceptance

Coincident Elastic Scattering Cross-Section

For the SOS central momentum and angle setting of $\theta_{SOS} = 47.5°$ and $P_{SOS} = 1.74$ GeV/c, the scattered protons from elastic *ep* events will have a momentum of 4.44 GeV/c and angle of 18.3°. The elastic electrons cover an electron momentum range of 2.08 to 1.73 GeV/c and angular range of 44° to 51° which corresponds to a proton momentum range of 4.25 to 4.61 GeV/c and angular range of 19.8° to 17.0°. The Q^2 range is from 6.4 to 7.1 (GeV/c)^2.

During the experiment, the HMS was set at three combinations of θ_{HMS} and P_{HMS} at which elastic *ep* coincidence events were detected. At $\theta_{HMS} = 18°$ and $P_{HMS} = 4.7$ GeV/c, the acceptance for elastic *ep* events is best matched. At $\theta_{HMS} = 19.5°$ and $P_{HMS} = 4.5$ GeV/c, the HMS in-plane angular acceptance reduces the SOS in-plane angular range to 44° to 47.5°. While for $\theta_{HMS} = 16.5°$ and $P_{HMS} = 4.5$ GeV/c, the HMS in-plane angular acceptance reduces the SOS in-plane angular range to 49° to 51°.

To extract measured elastic *ep* yields, the same data cuts listed in Table 3.4 were used with an additional cut of $0.8 < W < 1.07$ GeV to isolate elastic events. The data were also corrected for tracking efficiency, trigger inefficiency, computer and electronic deadtime. The same SIMC Monte Carlo was used with *ep* elastic cross section calculated using the electric and magnetic form factors from the fit of Bosted [96]. At this $Q^2 = 6.76$ (GeV/c)^2, the proton magnetic form factor is the dominant contribution to the elastic cross section and a conservative estimated error on the predicted cross section is 4%. In Fig. 3.18, the ratio of data yield to predicted Monte Carlo yield is plotted as a function of electron scattering angle for all three settings. Between scattered electron angle of 45.5° to 49.5°, the ratio is reasonably constant with an average value of 0.97 ± 0.01 which indicate good agreement with previous measurements. Below 45.5°, the agreement falls off sharply and above 49.5° the ratio jumps to an average of 1.08 which demonstrate problems in understanding the SOS acceptance. But these regions of SOS momentum and angle are not used in the extraction of the $p(e, ep)\eta$ cross sections and therefore the single arm comparison is best for checking the SOS acceptance. The *ep* coincidence comparison is useful as a check on the understanding of the experimental luminosity and efficiency corrections.

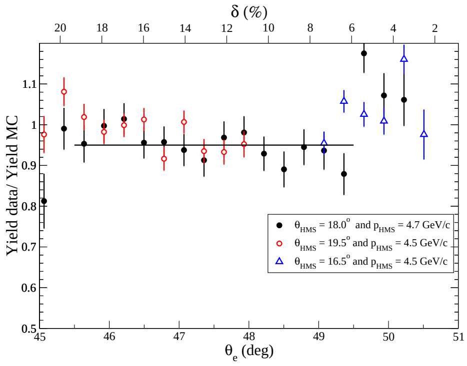

Figure 3.18: (Colour online) Ratio of yield of elastic *ep* coincidence events to predicted yield from Monte Carlo (Yield Data/Yield MC) plotted versus θ_e for $\theta_{SOS} = 47.5°$ and three different combinations of θ_{HMS} and p_{HMS}. The solid line is the average ratio $= 0.97 \pm 0.01$, of all points between $\theta_e = 45.5°$ to $49.5°$. The corresponding value of electron δ for a given θ_e is given by the upper x-axis.

Inclusive Elastic and Inelastic Cross-Section

In order to determine how accurately the SIMC simulation package models the acceptance of the SOS spectrometer, we extracted single-arm elastic and inelastic cross-sections from hydrogen and compared them with a fit to previous data. This inclusive analysis had the same set of data runs, the same correction factors whenever applicable, the same acceptance simulation code and the same electron identification cuts, as the coincidence analysis.

In the inclusive case, corrections for the target endcaps were much larger than in the coincidence case, and an additional correction for pair-symmetric backgrounds was needed (up to 10% at the highest W). These were determined using interpolated positron cross sections measured in a previous experiment [97] with the same target and beam energy, but slightly different scattering angles at 45, 55, and 70 degrees. This correction is negligible for the coincidence analysis due to the imposition of missing mass cuts.

Another difference is that radiative corrections were done analytically, rather than in the Monte Carlo simulation. For both elastic and inelastic scattering these were calculated using the formalism of Mo and Tsai [98]. For the required elastic scattering cross-section model, we used the form factor parametrisation of Bosted [96], while for the inelastic cross-section model we used the May 2007 fit of Christy and Bosted [90].

To obtain final radiated cross-section for a proton target, the cross-sections from the Al dummy target were subtracted with the appropriate scale factor to match the thickness of the endcaps. The small difference in radiative corrections between the endcaps and dummy was not taken into account.

The W dependence of the extracted inelastic cross-section, taken from the central region of the SOS spectrometer is plotted in Fig. 3.19 along with the Christy model. Generally, the W-dependence is in quite good agreement

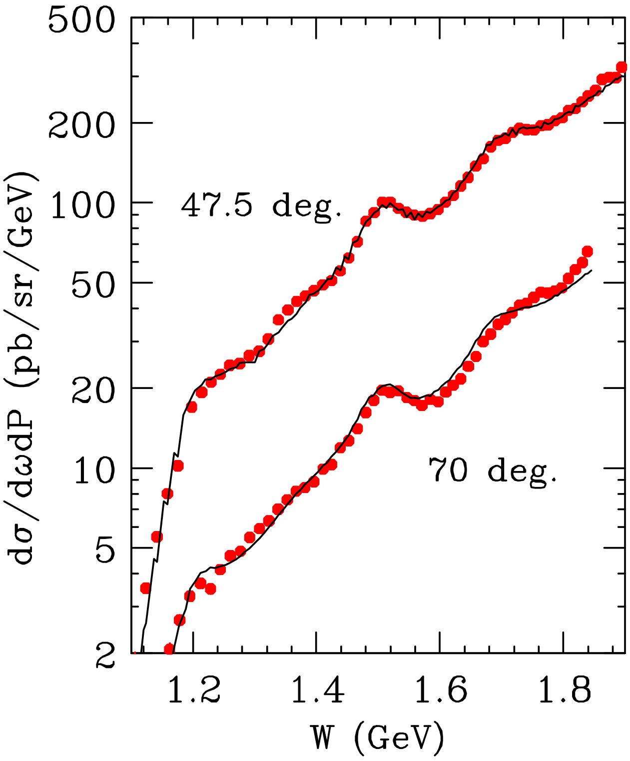

Figure 3.19: (Colour online) Inclusive inelastic differential cross-sections as measured by the SOS spectrometer centered at 47.5 and 70 degrees, as a function of W, with the angular cut $-30 < dy/dz < 30$ mr. The curves are from a fit to world data [90].

with Christy fit, especially for $1.5 < W < 1.6$ GeV, which is the main focus of this thesis. Based on this analysis, a systematic uncertainty of 3% was assigned to the acceptance of the SOS spectrometer.

3.4.6 Systematic Error Analysis

Depending on the source of error, one of two different methods was used to account for it. Those errors that were independent of the kinematic variables of the extracted data, W, cosθ^*_η and ϕ^*_η, were treated globally and applied to the data overall. The sources of this kind of error are summarised in Table 3.7.

The pion contamination through the PID cut for electrons was calculated by Villano [1], using the data of this experiment, to be 1.6%. Most of these pions are from random coincidences and are effectively removed by the coincidence time cut—an analysis for the F_π experiment [42] shows the residual contamination to be about 0.1%. The systemstic error in the target density and charge measurement were also determined by the F_π analysis [42]. The error in the HMS acceptance is the quadrature sum of the 0.5% point-to-point error and 0.8% normalisation error determined by Christy [99]. The overall error is dominated by the uncertainty in the SOS acceptance.

Parameter	Uncertainty	Reference
SOS acceptance	3.0%	Sec. 3.4.5
Radiative Corrections	2.0%	Sec. 3.4.3
Trigger efficiency	1.4%	Sec. 3.4.1
Proton absorption	1.0%	Sec. 3.4.1
HMS acceptance	1.0%	Ref. [99]
Target density	0.6%	Ref. [87]
Charge measurement	0.5%	Ref. [87]
Electron PID cut	0.1%	Ref. [1, 87]
TOTAL	4.2%	

Table 3.7: The sources of global systematic error and their estimated sizes.

If a source of error was expected to be dependent on kinematics, then it was treated on a bin-by-bin basis. The Monte Carlo simulation was run with altered parameters to mimic the uncertainty, and the subsequent analysis was done to compare to the extracted cross-section and quantify the effect bin-by-bin. The parameters that were altered, listed in Table 3.8, were those considered imprecisely known or that affect the determination of the cross-section. The best choice set of parameters were used for the standard analysis from which the final differential cross-section was calculated. Each parameter was then varied and the complete analysis repeated, up to the point of attaining the differential cross-section. The parameters were not varied together, as would be done in a fit, since it was assumed that to first order they acted independently and thus the prohibitive extra effort was unnecessary.

The drift chamber resolutions, r_{DC}, for the HMS and SOS spectrometers were calibrated as described in Section 3.4.1. In order to completely account for any error, these parameters were arbitrarily increased by 10% for the variation procedure. The exact position of the target in the beam direction, z_{targ}, was only known to within 3 mm. For the standard analysis, the middle position of this uncertainty window, an offset of 1.5 mm from the nominal centre, was chosen. The variation used for this parameter was the maximum possible extent of the motion, 1.5 mm in either direction.

The SOS spectrometer was found to be somewhat out-of-plane, but the exact amount is uncertain. A survey of the hall produced a value of $x'_{\mathrm{SOS}} = 2.62$ mr, which was used in this extraction, while an analysis of ep coincidence data by the F_π experiment [42] yielded $x'_{\mathrm{SOS}} = 3.2$ mr. The spectrometer offset was thus varied in both directions, to 1.5 mr and 3.5 mr, for the systematic analysis.

The cut on missing mass squared m_x^2, is described in Sec. 3.4.2. The effect of this cut was taken into account by including it as one of the parameters varied in the systematic analysis. The variation chosen was to widen this cut on both ends by 0.1 GeV^2 and then subsequently to narrow it by the same amount.

If x_i was the value of the differential cross-section in bin i for the standard analysis and y_i^v was for the analysis of a certain variation v, then the systematic error for that variation in that bin was taken as half the difference, $\delta_i^v = |x_i - y_i^v|/2$.

For the purposes of conveying the size of each of the systematic errors in Table 3.8, a measure of the average size $\langle \delta^v \rangle$ is used. This is the mean systematic error for all bins, weighted by the statistical error of the measurement in each bin

$$\langle \delta^v \rangle = \frac{\sum_i \delta_i^v / \sigma_i^2}{\sum_i 1/\sigma_i^2},$$

where σ_i is the statistical error of the differential cross-section in bin i.

Parameter		p_{std}	p_{var}	$\langle \delta^v \rangle$
HMS r_{DC}	(mm)	0.57	0.66	3.1%
SOS r_{DC}	(mm)	0.35	0.39	3.7%
x'_{SOS} offset	(mr)	2.62	1.5	3.1%
		2.62	3.5	2.8%
z_{targ} offset	(mm)	1.5	0.0	3.0%
		1.5	3.0	2.9%
m_x^2 cut	(GeV^2)	$f(\cos\theta^*)$	$f_{\mathrm{min}-0.1}^{\mathrm{max}+0.1}$	3.5%
		$f(\cos\theta^*)$	$f_{\mathrm{min}+0.1}^{\mathrm{max}-0.1}$	2.8%

Table 3.8: The various sources of kinematic dependent systematic errors considered in the analysis, the standard simulation values p_{std}, the systematic variation p_{var}, and the weighted mean systematic error for all bins, $\langle \delta^v \rangle$.

The total bin i systematic error, δ_i^{tot}, was determined by adding in quadrature the systematic error for each variation, δ_i^v, and the global systematic errors, δ_{glo}, to give $\delta_i^{\text{tot}} = \sqrt{\sum_v (\delta_i^v)^2 + \sum \delta_{\text{glo}}^2}$.

3.5 Results

3.5.1 Differential Cross-Section $p(e, e'p)\eta$

The differential cross-sections for the centre-of-mass scattering angles of the η are extracted in the bins described in Section 3.4.1, with large W bins to allow more angular bins. Figure 3.20 shows these data for the lower-Q^2 setting. The diminishing experimental acceptance as W increases, especially in out-of-plane ϕ_η^* bins, is evident. As seen in previous data [63, 82, 57, 72], a dominant isotropic, or S-wave, component is seen at W from threshold to the S_{11} resonance peak.

Equation (3.8) is the parametrisation of the virtual photon cross-section in terms of its angular dependence. The extracted differential cross-section was fitted with Eq. (3.8), for the lower W bins where there is sufficient angular acceptance for a fit, and is plotted in Fig. 3.20. The parameters extracted from the fit are plotted in Fig. 3.21 and listed in Table 3.9. Using the results of the fit, the anisotropy in the threshold to resonance region is shown to be at most about 15% for the lower-Q^2 setting.

The results of this fit can be compared to similar studies of the angular dependence of η production data. The recent CLAS data [72] was also fit with Eq. (3.8). The term linear in $\cos\theta_\eta^*$ shows definite structure at all measured Q^2. It was observed that as W increases above where the $S_{11}(1535)$ is expected to be dominant, the $\cos\theta_\eta^*$ dependence changes dramatically. At $W = 1.66$ GeV it decreases monotonically with $\cos\theta_\eta^*$, but by $W = 1.72$ GeV the forward backward-asymmetry is reversed. Previous experiments, at pho-

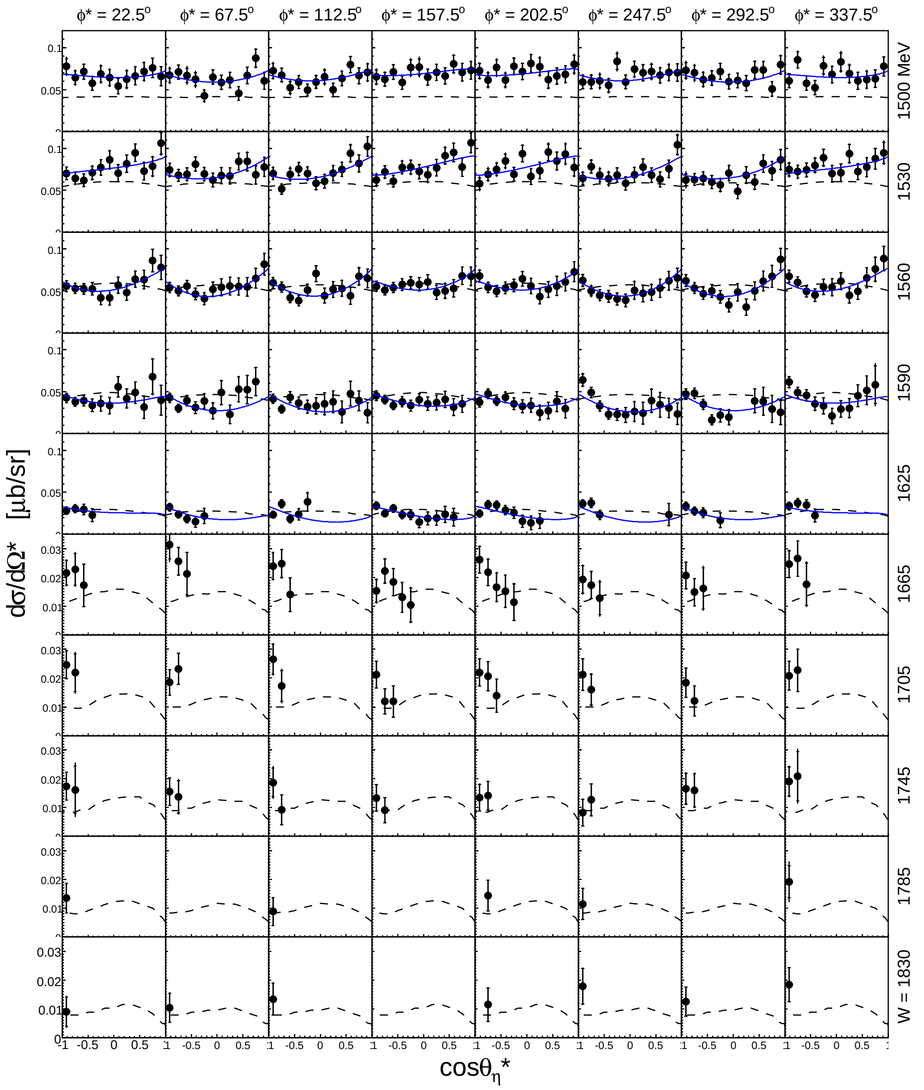

Figure 3.20: (Colour online) Extracted $ep \rightarrow ep\eta$ differential cross-sections for the lower-Q^2 setting. The solid (blue) curve is a fit of Eq. (3.8) to each W bin. The dashed curve is the ETA-MAID [100] isobar model for η-electroproduction from the nucleon at $Q^2 = 5$ GeV^2, projected to the appropriate Q^2 for each W bin by the factor $(5\ \text{GeV}^2/Q^2(W))^3$. The inner error bars are statistical and the outer error bars, the quadrature sum of the statistical and systematic errors.

	W = 1500 MeV	W = 1530 MeV	W = 1560 MeV	W = 1590 MeV	W = 1625 MeV
A	63.34 ± 1.59	71.25 ± 1.53	47.75 ± 1.41	30.65 ± 1.50	19.84 ± 3.42
B	2.70 ± 1.89	10.95 ± 1.88	7.54 ± 1.79	-1.74 ± 2.18	-5.53 ± 7.81
C	7.27 ± 3.71	8.17 ± 3.62	21.37 ± 3.37	14.63 ± 3.66	7.88 ± 6.58
D	-2.53 ± 1.89	-0.57 ± 1.83	0.10 ± 1.66	1.67 ± 1.83	2.80 ± 5.06
E	-3.83 ± 4.16	-3.67 ± 4.04	4.11 ± 3.59	3.47 ± 3.83	4.01 ± 8.16
F	4.86 ± 2.04	8.17 ± 1.96	5.06 ± 1.78	5.73 ± 1.86	4.53 ± 2.65

Table 3.9: The extracted angular parameters from a fit of Eq. (3.8) to the lower-Q^2 extracted differential cross-section.

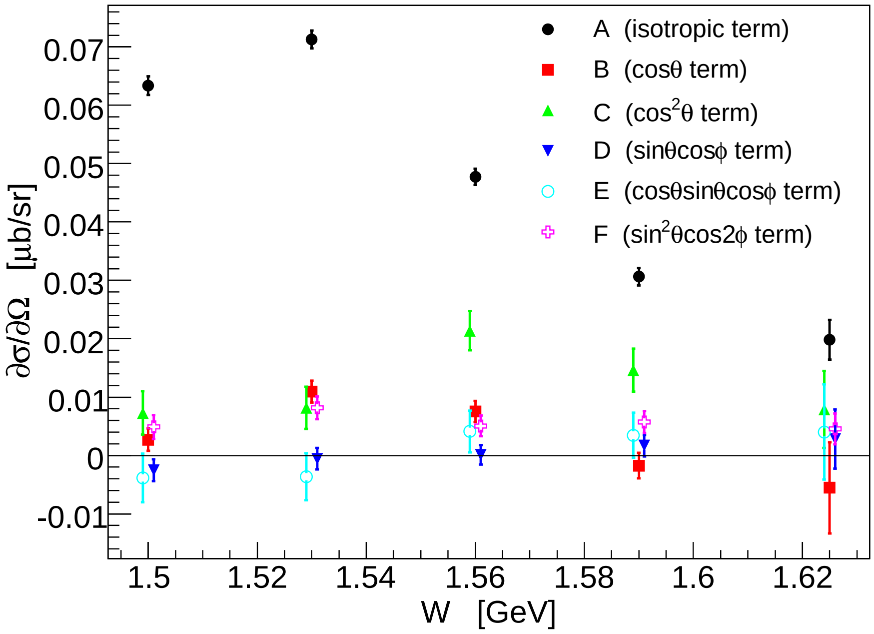

Figure 3.21: (Colour online) Extracted parameters from fits of Eq. (3.8) to the lower-Q^2 differential cross-section, shown as curves in Fig. 3.20.

toproduction [101] and at higher Q^2 [57], have shown the same structure in the W dependence of B, with B/A appearing to be roughly independent of Q^2 up to $Q^2 = 2.5$ GeV^2 [72].

The quantity B/A for the present work and previously published data [72, 57, 63] is plotted in Fig. 3.22. Due to diminishing angular acceptance the present work does not extend above $W \sim 1.65$ GeV where the ratio reaches its minimum and begins to make a rapid change from negative to positive. For W near the S_{11} resonance mass (black dotted line in figure), the B/A structure shows some difference between the CLAS data [72] which remains negative and data from the present work and others [57, 63] which do go positive, but the *trend* is the same and continues to be approximately independent of Q^2 up to ∼5.8 GeV^2.

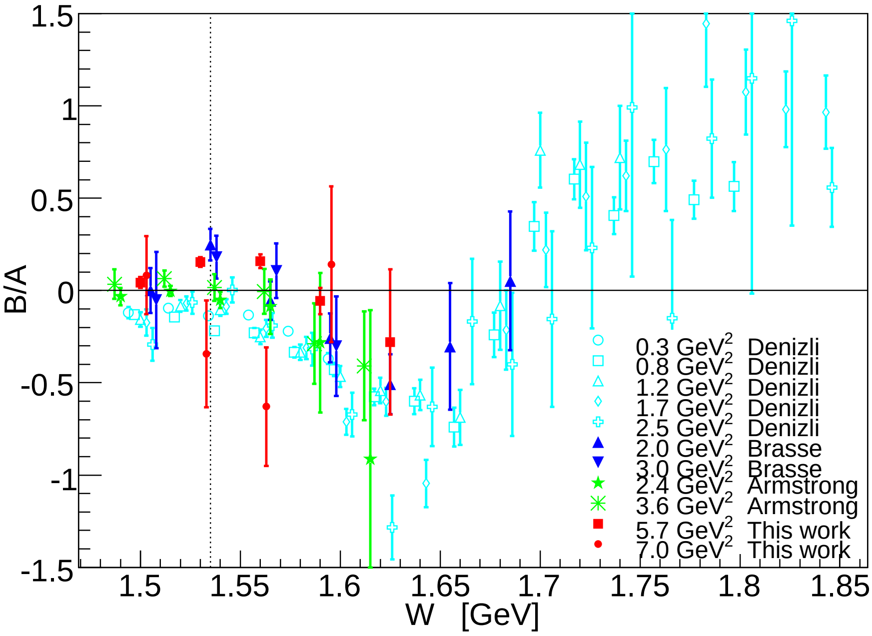

Figure 3.22: (Colour online) The result of fits to the differential cross-section, plotted as the ratio of the linear cosθ^*_η term to the isotropic component, for the present work and other η-electroproduction data [57, 63, 72]. The black dotted line is drawn at $W = 1.535$ GeV, the nominal mass for the S_{11} resonance.

The higher-Q^2 setting data were not amenable to the full angular fit, as can be seen in Fig. 3.23, so the fit function was truncated to $d\sigma/d\Omega^* = A + B\ \cos\theta^*$ and fitted to the data. There is large uncertainty on the extraction of B/A for these data, and the results are consistent with no structure, as can be seen in Fig. 3.22.

Denizli *et al.* [72] show that the rapid change in sign of B could be due to a P wave resonance at $W \approx 1.7$ GeV. Specifically, a simple resonance model incorporating the $P_{11}(1710)$ could describe their data, but they do acknowledge that the $P_{13}(1720)$ is also a candidate. The approximate Q^2

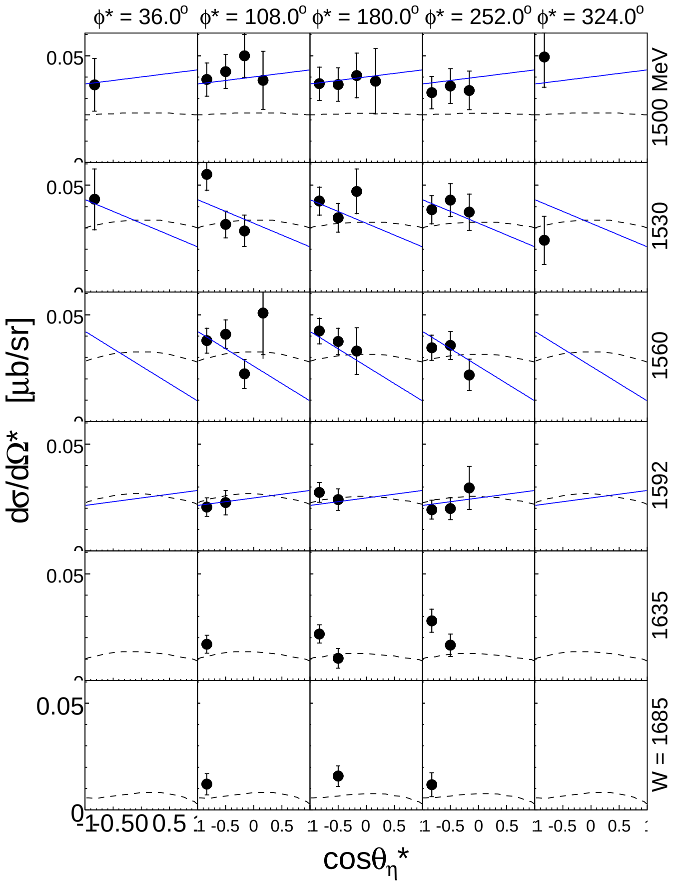

Figure 3.23: (Colour online) Extracted $ep \to ep\eta$ differential cross-sections for the higher-Q^2 setting. The (blue) solid curve is a fit to the data of the form $d\sigma/d\Omega^* = A + B \cos\theta^*$. The dashed curve is the ETA-MAID model [100] at $Q^2 = 5$ GeV^2, projected to the appropriate Q^2 for each W bin by the factor $(5 \text{ GeV}^2/Q^2(W))^3$. The inner error bars are statistical and the outer error bars, the quadrature sum of the statistical and systematic errors.

independence of the magnitude of this feature would imply that such a P wave falls similarly slowly with Q^2 as the $S_{11}(1535)$.

As can be seen in Fig. 3.21, the $\cos^2\theta_\eta^*$ term in the angular fit to the lower-Q^2 data is also quite significant for W above the resonance mass. In this case, the agreement with [72] is not good, as can be seen in Fig. 3.24. This disagreement can also clearly be seen qualitatively in Fig. 3.20 where the ETA-MAID [100] curves are concave down while the new data are concave up.

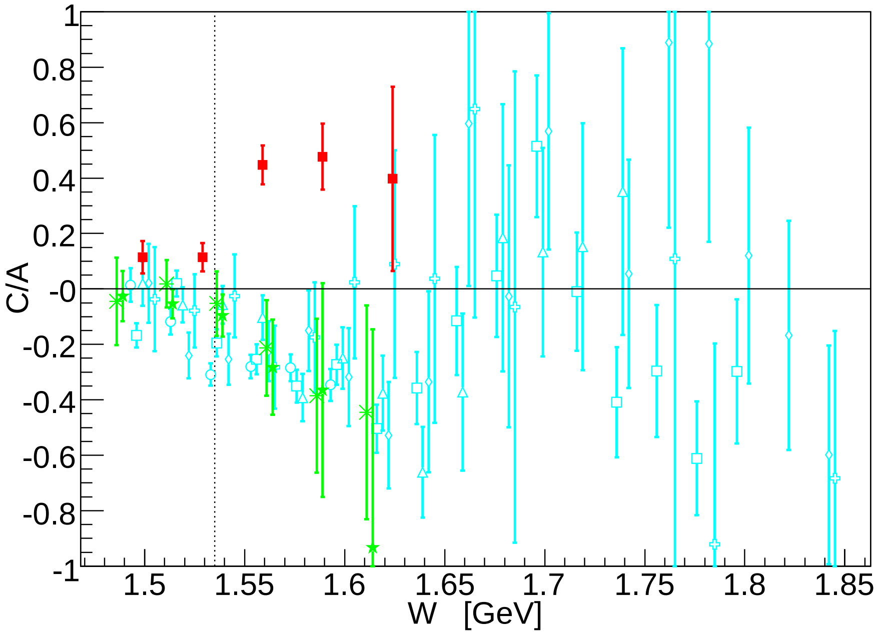

Figure 3.24: (Colour online) The ratio of the quadratic $\cos^2\theta^*_\eta$ term to the isotropic component for fits to the η-electroproduction differential cross-section, for the present work and other data [63, 72]. Symbols are the same as Fig. 3.22.

3.5.2 Total Cross-Section $p(e, e'p)\eta$

The total cross-section was determined from the differential cross-section in two ways. Firstly, the total cross-section was obtained by taking the weighted mean of the differential cross-section in each W bin and multiplying it by 4π, where the uncertainty in the mean is the quadrature sum of the statistical and systematic errors from all the bins. In W bins where there is full coverage, this is equivalent to integrating the differential cross-section. The total cross-section found using this method is listed in Table 3.10, along with the weighted average Q^2 in each W bin and the percentage of the 4π c.m. angular range accepted in each W bin. Secondly, the fitted angular dependence, Eq. (3.8) with parameters given in Table 3.9, was integrated in each W bin. Here, the uncertainty was determined by fixing each of the six parameters to the high and low one-sigma Minuit fit values and then fitting the remaining five parameters and determining the integral. The maximum and minimum values of the integral so determined were used to estimate the error. This second procedure couldn't be applied to the higher-Q^2 setting because the sparsity of the data precluded the fitting of the full angular dependence. The total cross sections determined in this way for each of the settings still have a Q^2 which varies with W.

The value of σ_R was obtained by fitting a relativistic Breit-Wigner to the total cross-section and evaluating it at the resonance mass. The Breit-Wigner is given by Eq. 3.17 and described in Section 3.4.3 and the non-resonant background is modeled as $A_{\rm nr}\sqrt{W - W_{\rm thr}} + B_{\rm nr}(W - W_{\rm thr})$. During the fit, the mean Q^2 value for that W bin was used. Due to strong correlations between the parameters, especially b_η and W_R, the branching fraction to η was fixed at $b_\eta = 0.5$ for the fits. The uncertainty in σ_R was estimated by individually fixing each of the Breit-Wigner parameters W_R and Γ_R to their Minuit uncertainties, redoing the fit and reevaluating σ_R. The maximum and minimum values of σ_R so determined were used to estimate the error.

This method worked well for the lowerQ^2 data, with good agreement of a single Breit-Wigner to the data. For the averaged differential cross-section a

$\langle Q^2\rangle$ [$\frac{\mathrm{GeV}^2}{\mathrm{c}^2}$]	W [GeV]	σ [nb]	$\sum\Omega^*_\eta/4\pi$
5.802	1.50	831.9 ± 19.7	100.0%
5.764	1.53	926.5 ± 20.9	100.0%
5.704	1.56	681.5 ± 17.1	100.0%
5.636	1.59	461.0 ± 15.0	93.8%
5.554	1.62	336.1 ± 14.4	45.8%
5.456	1.67	247.8 ± 14.7	29.2%
5.353	1.71	239.0 ± 17.1	18.8%
5.248	1.75	175.6 ± 17.8	16.7%
5.136	1.78	160.3 ± 31.7	5.2%
5.022	1.83	162.9 ± 27.2	7.3%
7.064	1.50	482.1 ± 33.3	43.3%
7.011	1.53	482.4 ± 30.5	36.7%
6.943	1.56	437.4 ± 28.5	33.3%
6.857	1.59	282.6 ± 25.0	23.3%
6.746	1.64	228.9 ± 26.9	16.7%
6.602	1.69	168.1 ± 37.5	10.0%
6.462	1.74	230.3 ± 60.3	3.3%

Table 3.10: Table of the total cross section, determined from the weighted average of extracted differential cross section. The weighted average Q^2 and the percentage of angular coverage for each W bin are also indicated. The errors are statistical and systematic added in quadrature, and do not take into account the angular acceptance.

small background contribution, less than 0.5%, was admitted under the resonance peak, while the fit to the integrated angular dependence model did not admit any background contribution. The higher-Q^2 data were amenable to such a fit since the large error bars and poor angular coverage make the parameters unreliable. For this reason, a simultaneous fit to both settings was thus done, yielding a single set of resonance parameters. The background was constrained to have the same Q^2 dependence as the data, essentially requiring it to have the same relative size. Figure 3.25 shows the results of this fit, which are listed in Table 3.11 along with the results of the fits to the lower-Q^2 data. The shape of the fitted function is dominated by the lower-Q^2 data, with a background of 1.2% at the resonance mass. The values from this simultaneous fit are used in the further analysis.

Both the simultaneous and the individual fits were repeated for $b_\eta = 0.45$ and 0.55. The results of these additional fits are plotted as correlation contours in Fig. 3.26. The σ_R extracted from each of these additional fits was at all times well within the error quoted in Table 3.11. It can be seen that there are correlations between b_η and W_R and also between W_R and Γ_R. The resonance parameters from the simultaneous fit are dominated by the lower-Q^2 data, as expected.

3.5.3 Helicity Amplitude $A_{1/2}$ for the $S_{11}(1535)$ Resonance

The amplitude $A_{1/2}$ is determined from the total cross-section at the $S_{11}(1535)$ resonance mass σ_R, by Eq. (3.12), which assumes $A_{1/2} \gg S_{1/2}$. Using the σ_R values obtained from the Breit-Wigner fit to the total cross-section, and those obtained in previous experiments [63, 57, 72], $A_{1/2}$ is determined consistently for all data with $\Gamma_R = 150$ MeV, $b_\eta = 0.55$ and $W_R = 1535$ MeV, chosen to coincide with those used previously [63, 72]. The uncertainties in

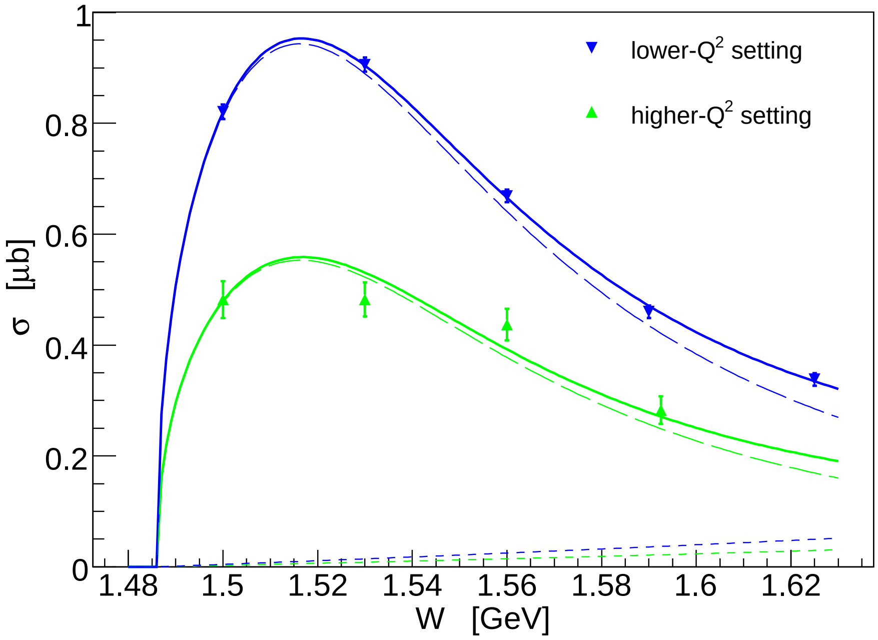

Figure 3.25: (Colour online) A simultaneous fit to the lower-Q^2 and higher-Q^2 data of the sum (solid line) of a relativistic Breit-Wigner (long dash) and non-resonant background term (short dashed line). The data are the total cross section determined from $4\pi\langle d\sigma/d\Omega^*\rangle$. The background was constrained as described in the text.

$A_{1/2}$ do not include uncertainties in W_R, b_η or Γ_R.

Table 3.11 summarises the parameters from the Breit-Wigner fit, the extracted total cross-section at the resonance mass, σ_R, and the extracted helicity amplitude, $A_{1/2}$. As can be seen in Fig. 3.27, the values of $\mathrm{A}_{1/2}$ determined in this work significantly extend the Q^2 range of the world's data. The curves in the figure [102, 65, 103, 104, 105] show a huge variation in the predicted values of $A_{1/2}$.

The magnetic form-factor of the proton G_M^p as published by Arnold *et al.* [39] demonstrates clear scaling behaviour. Naive dimension counting in

			$Q^2(W_R)$ $[\mathrm{GeV}^2/c^2]$	W_R [GeV]	Γ_R [GeV]	σ_R $[\mu b]$	$\mathrm{A}_{1/2}$ $[\times 10^{-3}\ \mathrm{GeV}^{5/2}]$
$\int d\sigma/d\Omega^*\|_{\mathrm{model}}$	indiv.		5.79	1.523 ± 0.001	0.125 ± 0.003	0.976 ± 0.007	23.62 ± 0.09
$4\pi\langle d\sigma/d\Omega^*\rangle$			5.79	1.523 ± 0.001	0.128 ± 0.010	0.977 ± 0.024	23.63 ± 0.30
$4\pi\langle d\sigma/d\Omega^*\rangle$	simul.	Fig. 3.25	5.79	1.522 ± 0.001	0.128 ± 0.009	0.943 ± 0.015	23.22 ± 0.18
$4\pi\langle d\sigma/d\Omega^*\rangle$		Fig. 3.25	7.04			0.553 ± 0.020	17.79 ± 0.33

Table 3.11: Parameters extracted from a relativistic Breit-Wigner fit to the data. The values for $A_{1/2}(Q^2)$ are determined from σ_R, assuming $A_{1/2} \gg S_{1/2}$, with parameters $W_R = 1.53$ GeV, $\Gamma_R = 150$ MeV and $b_\eta = 0.55$.

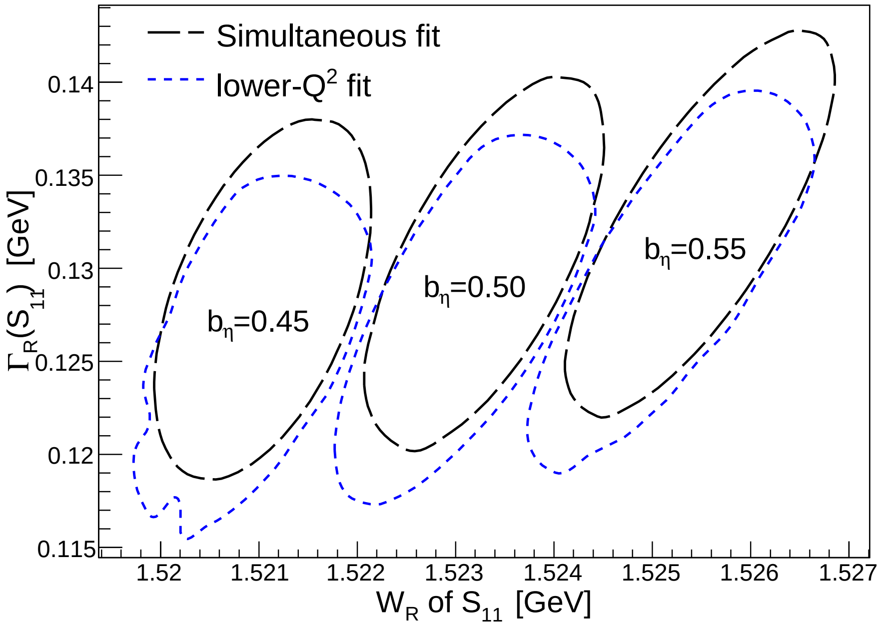

Figure 3.26: (Colour online) Plot of the 1-sigma contours from the various Breit-Wigner fits to the data.

pQCD predicts a falloff of $1/Q^4$ and the quantity of $Q^4G_M^p$ reaches a broad maximum at about $Q^2 \sim 8$ GeV^2 and then decreases in a gentle logarithm due to the running of the strong coupling constant α_s. The same arguments predict that the helicity amplitude for the $S_{11}(1535)$ decreases with $1/Q^3$. Figure 3.28 is a plot of $Q^3A_{1/2}$, showing that the quantity $Q^3A_{1/2}$ appears to begin flattening at a photon momentum transfer broadly within the range of this work, $Q^2 \sim 5-7$ GeV^2, a possible signal of the onset of pQCD scaling. A pQCD calculation by Carlson and Poor [60], of the magnitude of this quantity, is plotted and is a factor of ~ 3 smaller than the data. It has also been pointed out that such scaling may have a non-perturbative explanation [106, 107].

In order to compare the behaviour of $A_{1/2}$ with the approach of G_M^p to

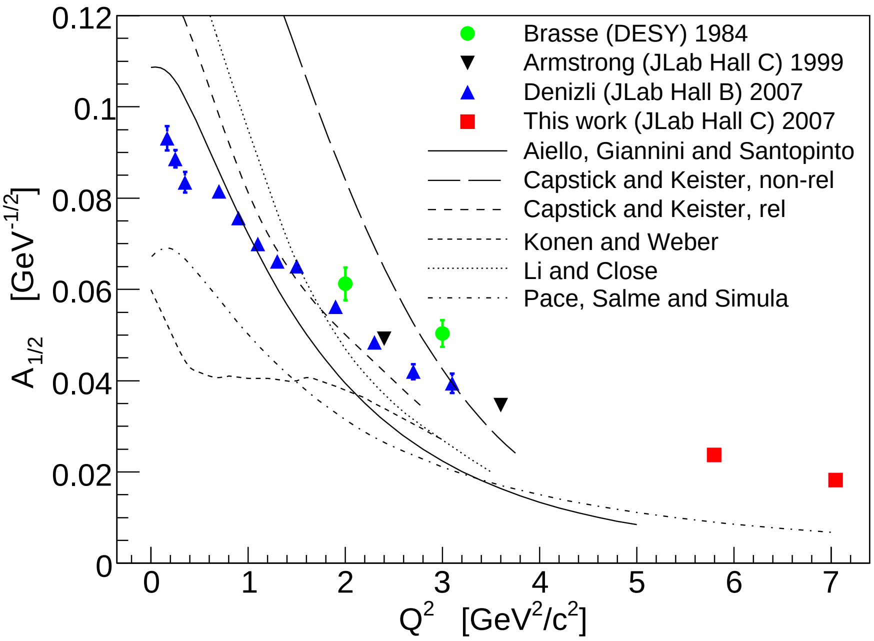

Figure 3.27: (Colour online) Values for $\mathrm{A}_{1/2}(Q^2)$ determined from σ_R for the present and other data [63, 57, 72] (consistently with $W_R = 1.53$ GeV, $\Gamma_R =$ 150 MeV and $b_\eta = 0.55$). The curves are from Refs. [102, 65, 103, 104, 105].

scaling, the quantity $Q^3 A_{1/2}/Q^4 G_M^p$ is plotted in Fig. 3.29. The form of G_M^p is taken from the fit by Bosted [96]. The figure shows that the two quantities do not have the same form at low Q^2, and the data does not go high enough in Q^2 to know whether the two quantities begin behaving equivalently.

3.6 Conclusions

We have presented the results of a precise, high statistics measurement of the differential cross-section for the $ep \rightarrow e'p\eta$ exclusive process. This is done at the highest momentum transfer to date, namely, $Q^2 = 5.8$ and 7.0 $(\mathrm{GeV}/c)^2$ at the S_{11} resonance mass, which is a significant extension from

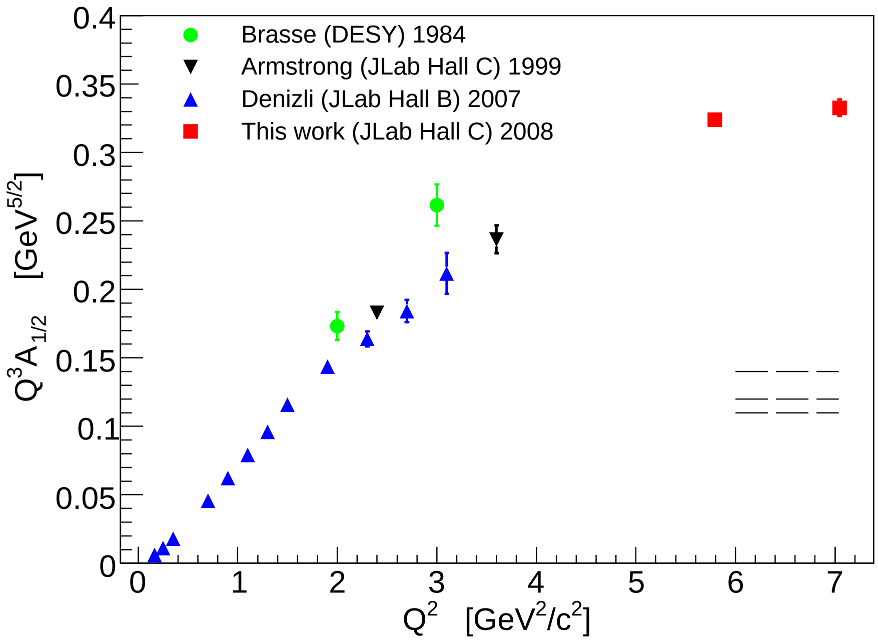

Figure 3.28: (Colour online) The Q^2 dependence of $Q^3A_{1/2}$ for η-production. Scaling in this quantity appears to begin at a photon momentum transfer of $Q^2 \sim 5$ GeV^2. The dashed lines are a high Q^2, pQCD calculation from Carlson and Poor [60] using three different nucleon distribution amplitudes.

the previous highest at $Q^2 = 3.6$ GeV^2. Data were obtained from threshold to $W = 1.8$ GeV, the $S_{11}(1535)$ dominating the channel as expected. In the region from threshold to the $S_{11}(1535)$ resonance mass, the differential cross-section is largely isotropic—consistent with previous measurements.

The interference phenomenon in the linear cosθ^*_η term at W of the $S_{11}(1535)$ resonance mass, seen in lower Q^2 and photoproduction data is observed here with similar strength. The present data does not have sufficient angular coverage at $W \sim 1.7$ GeV to comment meaningfully on the strong presence of a P wave resonance there. The curvature in the cosθ^*_η dependence of the differential cross-section is opposite to that of the data

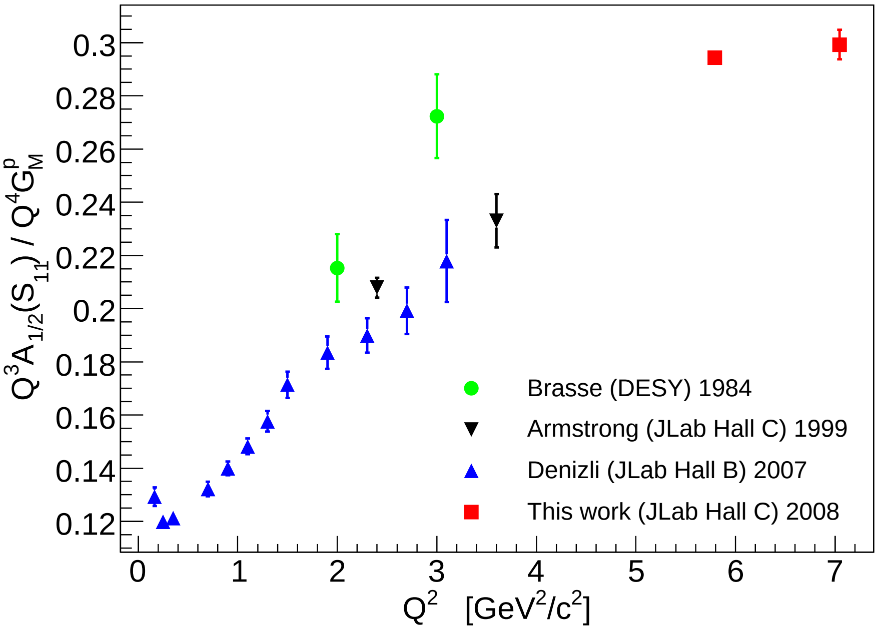

Figure 3.29: (Colour online) The Q^2 dependence of $Q^3A_{1/2}(S_{11})/Q^4G_M^p$ for η-production.

at lower-Q^2. The helicity-conserving transition amplitude $A_{1/2}$, is extracted from the data assuming $A_{1/2} \gg S_{1/2}$. The Q^2 dependence of $Q^3A_{1/2}$ seems to be flattening, consistent with the pQCD prediction, although the range of Q^2 is too small to verify the exact dependence. Even if the data scale as predicted by pQCD, that is not conclusive evidence for the onset of pQCD.

On the theoretical front, the differential cross-section will be incorporated into multi-channel, multi-resonance models, such as those by the MAID and EBAC groups, which should maximize the physics impact coming from these data. Also, the inability for any one calculation to adequately describe the Q^2 dependence of $A_{1/2}$ leaves much to be done in understanding the structure of the $S_{11}(1535)$. On the experimental front, more data are required to further address the questions in this thesis.

It would be nice to fill the data gap in the region between $Q^2 \sim 4$ and 5.8 GeV^2 to analyse the apparent change of differential cross-section shape. Extending the data to Q^2 much higher than 7 GeV^2 will complete the study of the transition to hard-scale scattering. Obtaining LT separated data at high Q^2 will enable checking of the assumption, made in this work and in the literature, that the longitudinal component is negligible. The planned upgrade of the Jefferson Lab accelerator, to energies as high as 11 GeV, will allow exclusive η electroproduction data to be obtained to $Q^2 \sim 14$ GeV^2, and LT separations at least to the Q^2 of this experiment.

Chapter 4

Discussion

4.1 Summary of the Measurement and Discussion of the Data

The differential cross section for the exclusive electroproduction of η mesons from free protons was measured at $Q^2 \sim 5.7$ and 7.0 (GeV/c)^2. The total cross section was determined, and the helicity amplitude for the production of the $S_{11}(1535)$ resonance extracted. This data was taken both with high statistical precision and at the highest Q^2 to date, almost doubling that of the previous highest [63]. This significantly extends our knowledge of these quantities into the region of transition between the hadronic regime of non-perturbative QCD and the the pQCD regime of asymptotically free quarks. This data has been comprehensively compared to data obtained at lower Q^2 and to theoretical predictions both at low Q^2 and made in the pQCD limit of very high Q^2.

Section 3.5.1 shows that the angular dependence of the differential cross section for this data makes a qualitative departure from the data at lower Q^2. The linear part of the $\cos\theta^*_\eta$ dependence behaves similarly to previous data, which is likely an interference phenomenon with a P wave resonance of similar Q^2 dependence located at $W \sim 1.7$ GeV [72]. On the other hand, the quadratic part of the cosθ^*_η dependence has changed sign. This can clearly be seen in Fig. 3.20 where the ETA-MAID model, based on fits to the lower Q^2 data and described in the next section, is concave down while the new data is concave up. Figure 3.24 shows quantitatively this departure. This is a very interesting result, however the full implications of this will only become clear within the context of a multi-channel analysis, such as will be described in the next section. It may, for example, indicate a changing with Q^2 of the relative strengths of the dominant $S_{11}(1535)$ resonance and the non-resonant background and other resonances, such as the $D_{13}(1520)$.

Section 3.5.3 describes how the helicity amplitude $A_{1/2}$ for the production of the $S_{11}(1535)$ resonance is extracted by fitting a single relativistic Breit-Wigner and model background to the total cross section. This approach makes a number of assumptions and only manages to get information about the dominant $S_{11}(1535)$ resonance. This is sufficient for the purposes of this thesis, but the potential of the data has not yet been fully exploited, since it contains small contributions and interference effects from other processes. Extracting this information will require its combination with the rest of the worlds data in fits that include things like complex amplitudes, and other more realistic features. It can be seen that this data will be a part of further contributions to the field.

4.2 Future Analysis of The Data

Here are briefly described two of the theoretical groups that analyse vast data sets, acquired with different probes, through various channels and kinematic regimes, in order to extract more accurate and globally meaningful results from them.

The Institut für Kernphysik, Universität Mainz, produce a unitary isobar model of meson photo- and electroproduction from the nucleon called MAID. Such models exist for π [108], η [79, 100], η' [100], K [109, 110] and $\pi\pi$ [111] production. These models may be "Reggeised" in order to be valid at higher photoproduction energy [112]. The data is used to extract parameters for the resonances, which are are then used to predict observables, a service used during the process of analysing the data in this thesis. The prediction from these models are published on the web, currently up to $Q^2 = 5$ GeV^2, which for η production include the following observables: electromagnetic multipoles, helicity amplitudes, unpolarised differential cross sections, transverse polarization observables and total cross sections. Similar sorts of models are fitted by the SAID group in the Centre for Nuclear Studies, Data Analysis Group at the George Washington University, although not for η electroproduction.

The Excited Baryon Analysis Center (EBAC) [113] is a international research group aiming to extract and interpret quark-gluon substructure of nucleon resonances. This is done by conducting dynamical coupled-channel analyses of the very extensive data on electromagnetic production of pseudoscalar mesons, vector mesons, and two pions, extracting the N^* parameters, and then investigating the reaction mechanisms to map out the quark-gluon substructure of the resonances. Figure 4.1 shows a schematic diagram of the EBAC strategy for connecting the fundamental theory of QCD to meson production via the parameters of N^* resonances.

When subjected to analyses by these groups, the data presented in this thesis will be used not only to extract both more accurate parameters for the dominant $S_{11}(1535)$ resonance, but it will also contribute to extracting

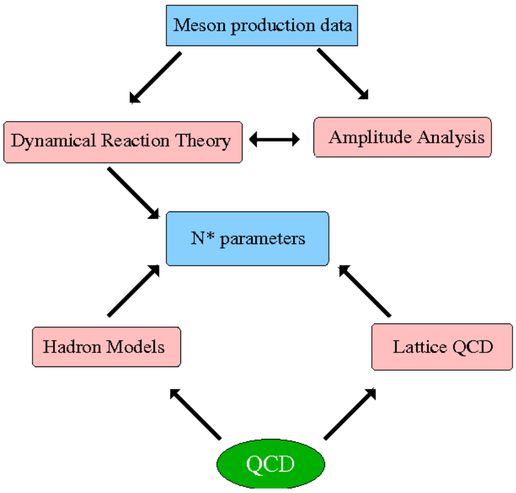

Figure 4.1: Schematic diagram of the EBAC strategy connecting QCD to meson production. Figure from Ref. [113]

information on the much smaller other contributions of the non-resonant background and other resonances.

4.3 Future Related Measurements

The Jefferson Lab 12 GeV Upgrade Hall-C Conceptual Design Report [114] makes it clear that Hall-C at Jefferson Lab, after the upgrade of the CEBAF accelerator to 12 GeV, will be the only facility in the world capable of continuing this work to higher Q^2. With an electron beam of up to 11 GeV in Hall-C and a new spectrometer called the Super HMS (SHMS) which can go to angles as small as 5.5 degrees and up to 11 GeV/c in momentum. The possible program here would provide data at the highest Q^2 on the proton electric and magnetic form factors, the pion form factor and the $N \rightarrow \Delta$ and $N \rightarrow S_{11}$ transitions. Section 2.3 describes the extent to which these measurements have been completed to date. The nucleon elastic and transition form factors may be measured up to $Q^2 \sim 15$ GeV and pion *and* kaon electroproduction up to $Q^2 \sim 10$ GeV including the *LT* separation necessary to extract the form factors. Figures 4.2 and 4.3 gives examples of what data will measurable for elastic form factors with the upgraded equipment. Figure 4.4 gives an example of what will be possible for the $N \rightarrow \Delta$ transition. Similar data for the $S_{11}(1535)$ would be taken concurrently.

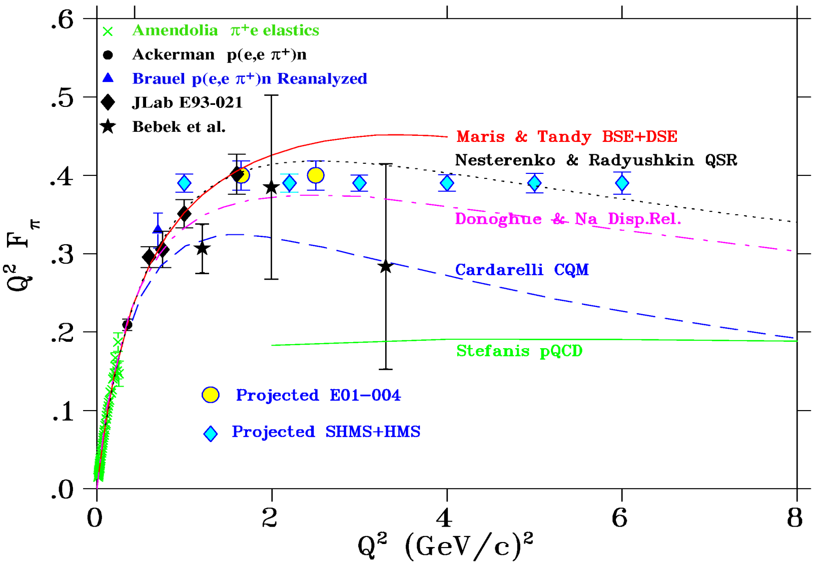

Figure 4.2: Projected future measurements of the pion form factor F_π. Blue diamonds denote the expected Q^2 points from an experiment at an upgraded Jefferson Lab in Hall-C. These data will span the range from confinement-dominated to pQCD-dominated kinematics. Figure from Ref. [114]

These potential new data would go a long way towards completing the measurement of the transition region connecting the confinement region and the region of asymptotic freedom. The form factors and structure functions so measured are intimately connected to our understanding of the three di-

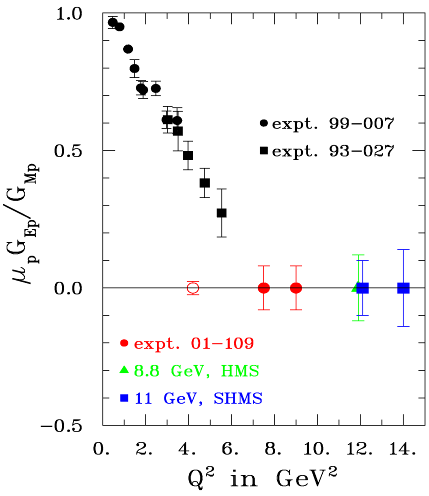

Figure 4.3: Projected future measurements of the proton electric to magnetic form factor ratio G_{Ep}/G_{Mp}. An experiment at an upgraded Jefferson Lab in Hall-C could reach $Q^2 \sim 14$ GeV. Figure from Ref. [114]

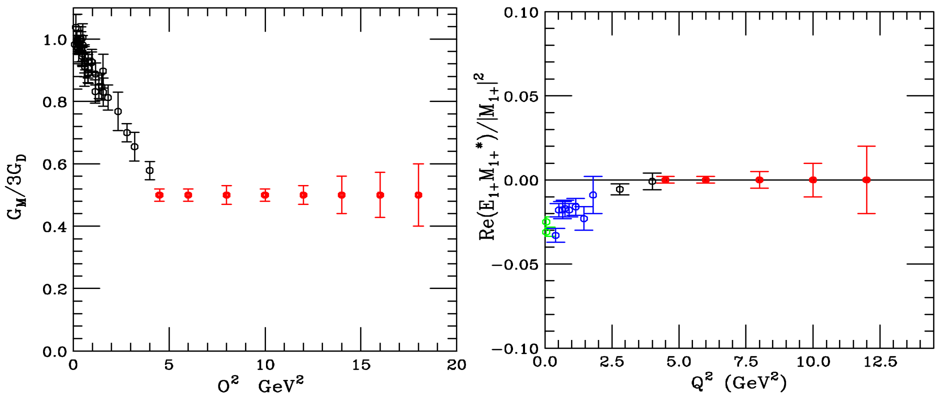

Figure 4.4: Projected future measurements, for the $N \rightarrow \Delta$ transition, of (left) the magnetic form factor and (right) the ratio of the electric quadrupole to magnetic dipole E_{1+}/M_{1+}. Red circles show the anticipated uncertainties from such a measurement at an upgraded Jefferson Lab in Hall-C, which could reach $Q^2 \sim 18$ GeV. Figure from Ref. [114]

mensional internal structure of the nucleon through the GPDs, as described in Section 2.2.4.

In Section 3.6 it was mentioned that there are possible measurements that arise directly from this data. The potential impact of these suggestions can only be assessed once the full implications of the data presented here becomes clear from other analyses. For example, it might be worth making a measurement in the region between $Q^2 \sim 4$ and 5.8 GeV^2 to analyse the apparent change of differential cross-section shape.

As was mentioned in Section 3.2.3, one of the main assumptions used in extracting the helicity conserving amplitude $A_{1/2}$ for the $S_{11}(1535)$ resonance is that the longitudinal contribution to the cross-section is negligible, $A_{1/2} \gg S_{1/2}$. A number of facts seem to support this. There is the *LT* separation of the exclusive η electroproduction cross section, extending up to $Q^2 \sim 1$ GeV^2 and with large uncertainties [71], that shows $R = \sigma_L/\sigma_T$ consistent with zero. There are also *LT* separations of the inclusive cross section [115], from which it is difficult to conclude much, but seem to show that R is smaller in the second resonance region than the surrounds, maybe indicating that the longitudinal component is due to the non-resonant background. Recent η electroproduction data shows $d\sigma_{\mathrm{LT}}/d\Omega^*$ consistent with zero [72] up to $Q^2 = 2.5$ GeV^2, also with large error bars. In pQCD, $F_L \propto \alpha_s$, and thus R is expected to decrease logarithmically with increasing Q^2 [116, 117, 118].

So while it seems like a reasonable assumption, it may still be a good idea to do an *LT* separation at Q^2 comparable to the data presented in this work. No detailed studies of the feasibility of this measurement have been done, but a brief calculation shows that after the upgrade, such a separation may be possible with only one measurement configuration. At a beam energy of 11 GeV, another measurement of the η electroproduction cross-section at $Q^2 \sim 5.8$ GeV^2 could be done with $\epsilon \sim 0.88$. This would be done with the HMS detecting electrons at about 15.5 degrees and momentum near the maximum at about 7.1 GeV, and the SHMS detecting protons. Combined with the lower-Q^2 data in this thesis would allow an LT separation to be done with $\Delta\epsilon \sim 0.45$, which seems reasonable. The same trick could be done with the higher-Q^2 data of this work to give $\Delta\epsilon \sim 0.6$, but this data is not over the full c.m. angles.

4.4 Summary

The avenues available to extend this work offer an exciting realm to learn more about the fundamental theory of QCD. The value of the data presented in this thesis is not limited to the results extracted here, but will form an important part of overarching and global analyses of nucleon structure. The program of mapping out the three dimensional structure of nucleons using GPDs is well under way and new measurements possible at Jefferson Lab after the upgrade may go a large way towards completing this.

Chapter 5

Conclusion

This thesis has presented an important new data set for use in understanding the complexities of nucleon structure. Chapter 1 gave a brief introduction to the problem and described the contribution that this thesis would make towards it's solution. Chapter 2 went on to give a broad overview of nuclear physics and then to locate the endeavours of understanding the fundamental degrees of freedom of QCD within that context. The concept of a form factor was introduced and its ability to connect the short and long distance scale regimes was discussed. This was generalised to transition form factors for producing baryon resonances and the connection to pQCD at high Q^2 was developed.

Chapter 3 presented the data of the thesis. These are the results of a high statistics measurement of the differential cross-section for exclusive η electroproduction, done at the highest momentum transfer to date, which is a significant extension from the previous highest. The $\cos\theta^*_\eta$ dependence of the differential cross-section is consistent with previous data. An interesting change in the $\cos^2\theta^*_\eta$ dependence was observed, when compared to data at lower Q^2. The $S_{11}(1535)$ is still by-far the dominant feature in $p\eta$ the channel. The helicity-conserving transition amplitude $A_{1/2}$ for the production of the $S_{11}(1535)$ was extracted from the data and its Q^2 dependence appears to be approaching that consistent with the pQCD prediction. There currently appears to be no theoretical calculation which adequately describe the Q^2 dependence of $A_{1/2}$ over the full measured range. This result is one of the most significant contributions of this work.

Chapter 4 went on to discuss the data presented earlier. Specific attention was paid to the process through which the data will be put once it is published. More information can be extracted from it than is done here, when it is analysed in conjunction with other data sets, using coupled-channel methods. This will involve a major effort from theoretical groups and is beyond the scope of this thesis. It is illustrative of the impact that the data from this thesis will have in the field. The possibility for future measurements at higher Q^2 was discussed, with specific reference to Jefferson Lab and its Hall-C, which may be the only facility capable of conducting these measurements.

This thesis therefore represents an important contribution to the worlds data in the transition region approaching where pQCD becomes the applicable description of the interaction.

Appendix A

List of Collaborators

M.M. Dalton,[1] G.S. Adams,[2] A. Ahmidouch,[3] T. Angelescu,[4]
J. Arrington,[5] R. Asaturyan,[6] O.K. Baker,[7,8] N. Benmouna,[9]
C. Bertoncini,[10] W.U. Boeglin,[11] P.E. Bosted,[8] H. Breuer,[12] M.E. Christy,[7]
S.H. Connell,[1] Y. Cui,[13] S. Danagoulian,[3] D. Day,[14] T. Dodario,[13]
J.A. Dunne,[15] D. Dutta,[16] N. El Khayari,[13] R. Ent,[8] H.C. Fenker,[8]
V.V. Frolov,[17] L. Gan,[18] D. Gaskell,[8] K. Hafidi,[5] W. Hinton,[7,8] R.J. Holt,[5]
T. Horn,[12] G.M. Huber,[19] E. Hungerford,[13] X. Jiang,[20] M.K. Jones,[8]
K. Joo,[21] N. Kalantarians,[13] J.J. Kelly,[12] C.E. Keppel,[7,8]
V. Kubarovsky,[8,2] Y. Li,[7] Y. Liang,[22] S. Malace,[4] P. Markowitz,[11]
P. McKee,[14] D.G. Meekins,[8] H. Mkrtchyan,[6] B. Moziak,[2] T. Navasardyan,[6]
G. Niculescu,[14] I. Niculescu,[23] A.K. Opper,[22] T. Ostapenko,[24]
P.E. Reimer,[5] J. Reinhold,[11] J. Roche,[8] S.E. Rock,[25] E. Schulte,[5]
E. Segbefia,[7] C. Smith,[14] G.R. Smith,[8] P. Stoler,[2] V. Tadevosyan,[6]
L. Tang,[7,8] V. Tvaskis,[26] M. Ungaro,[21] A. Uzzle,[7] S. Vidakovic,[19]
A. Villano,[2] W.F. Vulcan,[8] M. Wang,[25] G. Warren,[8] F.R. Wesselmann,[14]
B. Wojtsekhowski,[8] S.A. Wood,[8] C. Xu,[19] L. Yuan,[7] X. Zheng,[5] H. Zhu,[14]

[1] *University of the Witwatersrand, Johannesburg, South Africa*

[2] *Rensselaer Polytechnic Institute, Troy, New York 12180*

[3] *North Carolina A & T State University, Greensboro, North Carolina 27411*

[4] *Bucharest University, Bucharest, Romania*

[5] *Argonne National Laboratory, Argonne, Illinois 60439*

[6] *Yerevan Physics Institute, Yerevan, Armenia*

[7] *Hampton University, Hampton, Virginia 23668*

[8] *Thomas Jefferson National Accelerator Facility, Newport News, Virginia 23606*

[9] *The George Washington University, Washington, D.C. 20052*

[10] *Vassar College, Poughkeepsie, New York 12604*

[11] *Florida International University, University Park, Florida 33199*

[12] *University of Maryland, College Park, Maryland 20742*

[13] *University of Houston, Houston, TX 77204*

[14] *University of Virginia, Charlottesville, Virginia 22901*

[15] *Mississippi State University, Mississippi State, Mississippi 39762*

[16] *Triangle Universities Nuclear Laboratory and Duke University, Durham, North Carolina 27708*

[17] *LIGO Livingston Observatory, Livingston, LA 70754*

[18] *University of North Carolina Wilmington, Wilmington, North Carolina 28403*

[19] *University of Regina, Regina, Saskatchewan, Canada, S4S 0A2*

[20] *Rutgers, The State University of New Jersey, Piscataway, New Jersey, 08855*

[21] *University of Connecticut, Storrs, Connecticut 06269*

[22] *Ohio University, Athens, Ohio 45071*

[23] *James Madison University, Harrisonburg, Virginia 22807*

[24] *Gettysburg College, Gettysburg, Pennsylvania 18103*

[25] *University of Massachusetts Amherst, Amherst, Massachusetts 01003*

[26] *Nationaal Instituut voor Subatomaire Fysica, Amsterdam, The Netherlands*

Appendix B

Publication List

B.1 Publications Arising from the Thesis Experiment (submitted and envisaged)

There are currently three publications anticipated to arise from the Jefferson Lab experiment E01-002, listed below.

1. Electroproduction of η Mesons in the $S_{11}(1535)$ Resonance Region at High Momentum Transfer; submitted to *Phys. Rev. C*; Dalton, M. M. *et al.*
2. Electroproduction of π^0 Mesons in the $\Delta(1232)$ Resonance Region at High Momentum Transfer; in prep. for *Phys. Rev. C*; Villano, A. *et al.*
3. Electroproduction of π^+ Mesons at High Momentum Transfer; in prep. for *Phys. Rev. C*

A further Physical Review Letter publication may be considered to herald the results of the $S_{11}(1535)$ Resonance paper after some further analysis has been done by theorists on the results. There may also be a further publication resulting from another channel measured concurrently, that of exclusive electroproduction of ω mesons.

B.2 Other Nuclear Physics Publications (published)

The following four publications arise from experiments at Jefferson Lab on which the author of this thesis is a collaborator.

1. Transverse momentum dependence of semi-inclusive pion production; e-Print: *arXiv:0709.3020 [hep-ph]*, Accepted by *Phys. Lett. B*; Mkrtchyan, H. *et al.*
2. Scaling study of the pion electroproduction cross sections and the pion form factor; e-Print: *arXiv:0707.1794 [nucl-ex]*; Horn, T. *et al.*
3. Measurement of Nuclear Transparency for the A(e,e'π^+) Reaction; *Phys. Rev. Lett.*, 99:242502, 2007; Clasie, B. *et al.*
4. The onset of quark-hadron duality in pion electroproduction; *Phys. Rev. Lett.*, 98:022001, 2007; Navasardyan, T. *et al.*

B.3 Other Publications (published and submitted)

1. On the macroscopic formation length for GeV photons; submitted to *Phys. Lett. B*; H.D. Thomsen, J. Esberg, K. Kirsebom, H. Knudsen, E. Uggerhøj, U.I. Uggerhøj, P. Sona, A. Mangiarotti, T.J. Ketel, A. Dizdar, and M.M. Dalton, S. Ballestrero, S.H. Connell
2. Quantum diffusion of isotropic muonium, MuT, in a 13C diamond; *Diamond and Related Materials, Volume 13, Issues 4-8, April-August 2004, Pages 909-913*; I. Z. Machi, S. H. Connell, M. M. Dalton, M. J. Sithole, K. Bharuth-Ram, S. F. J. Cox and C. Baines

Appendix C

Tables of Differential Cross Sections

C.1 Lower-Q^2 Data

Table C.1: Lower-Q^2 extracted differential cross-section.

W [GeV]	$\cos\theta^*_\eta$	ϕ_η [deg.]	$\langle Q^2_{\text{bin}} \rangle$ $[\frac{\text{GeV}^2}{\text{c}^2}]$	$\langle \epsilon \rangle$	rad. corr.	$\frac{d^2\sigma}{d\Omega^*_\eta}$ $[\frac{n\text{b}}{\text{sr}}]$	δ_{stat} $[\frac{n\text{b}}{\text{sr}}]$	δ_{syst} $[\frac{n\text{b}}{\text{sr}}]$
1.500	-0.917	22.5	5.80	0.427	1.51	60.6	8.3	3.6
1.500	-0.917	67.5	5.80	0.427	1.52	72.8	9.2	6.9
1.500	-0.917	112.5	5.80	0.426	1.49	59.1	8.0	4.6
1.500	-0.917	157.5	5.80	0.427	1.52	72.3	8.9	5.2
1.500	-0.917	202.5	5.80	0.426	1.50	65.1	8.5	5.5
1.500	-0.917	247.5	5.80	0.427	1.52	72.3	8.8	6.0
1.500	-0.917	292.5	5.80	0.426	1.52	67.0	8.4	6.2
1.500	-0.917	337.5	5.80	0.426	1.49	77.8	9.4	7.0
1.500	-0.750	22.5	5.80	0.427	1.53	85.5	9.8	5.2

W [GeV]	$\cos\theta^*_\eta$	ϕ_η [deg.]	$\langle Q^2_{\text{bin}}\rangle$ $[\frac{\text{GeV}^2}{\text{c}^2}]$	$\langle\epsilon\rangle$	rad. corr.	$\frac{d^2\sigma}{d\Omega^*_\eta}$ $[\frac{nb}{\text{sr}}]$	δ_{stat} $[\frac{nb}{\text{sr}}]$	δ_{syst} $[\frac{nb}{\text{sr}}]$
1.500	-0.750	67.5	5.80	0.427	1.53	69.9	8.6	6.5
1.500	-0.750	112.5	5.81	0.426	1.48	59.2	7.9	4.7
1.500	-0.750	157.5	5.81	0.425	1.53	61.5	8.3	6.1
1.500	-0.750	202.5	5.79	0.427	1.52	62.3	8.0	4.5
1.500	-0.750	247.5	5.79	0.428	1.49	67.3	8.1	4.6
1.500	-0.750	292.5	5.80	0.427	1.51	70.8	8.4	3.7
1.500	-0.750	337.5	5.80	0.427	1.55	64.3	8.3	5.0
1.500	-0.583	22.5	5.80	0.427	1.54	57.7	8.4	4.0
1.500	-0.583	67.5	5.79	0.428	1.46	61.9	8.4	5.2
1.500	-0.583	112.5	5.80	0.427	1.53	60.1	8.2	6.3
1.500	-0.583	157.5	5.79	0.428	1.51	76.2	9.3	6.4
1.500	-0.583	202.5	5.78	0.428	1.46	71.0	8.6	3.8
1.500	-0.583	247.5	5.80	0.427	1.52	52.4	7.2	6.0
1.500	-0.583	292.5	5.79	0.428	1.51	66.9	8.7	7.2
1.500	-0.583	337.5	5.80	0.428	1.60	71.4	9.0	3.9
1.500	-0.417	22.5	5.81	0.426	1.53	52.3	8.6	3.1
1.500	-0.417	67.5	5.80	0.426	1.51	63.6	8.7	4.5
1.500	-0.417	112.5	5.80	0.427	1.53	54.9	7.9	5.2
1.500	-0.417	157.5	5.80	0.427	1.49	61.3	8.2	6.1
1.500	-0.417	202.5	5.79	0.428	1.48	58.3	8.1	3.2
1.500	-0.417	247.5	5.80	0.427	1.46	59.1	7.7	3.4
1.500	-0.417	292.5	5.80	0.427	1.51	62.2	7.8	6.8
1.500	-0.417	337.5	5.80	0.426	1.53	57.4	8.4	3.4
1.500	-0.250	22.5	5.81	0.426	1.52	78.5	9.9	6.9
1.500	-0.250	67.5	5.80	0.427	1.51	71.6	9.4	4.6

W [GeV]	$\cos\theta^*_\eta$	ϕ_η [deg.]	$\langle Q^2_{\mathrm{bin}}\rangle$ $[\frac{\mathrm{GeV}^2}{\mathrm{c}^2}]$	$\langle\epsilon\rangle$	rad. corr.	$\frac{d^2\sigma}{d\Omega^*_\eta}$ $[\frac{n\mathrm{b}}{\mathrm{sr}}]$	δ_{stat} $[\frac{n\mathrm{b}}{\mathrm{sr}}]$	δ_{syst} $[\frac{n\mathrm{b}}{\mathrm{sr}}]$
1.500	-0.250	112.5	5.80	0.427	1.48	83.6	9.6	7.3
1.500	-0.250	157.5	5.80	0.427	1.46	77.7	9.7	5.5
1.500	-0.250	202.5	5.79	0.428	1.47	76.3	9.2	6.6
1.500	-0.250	247.5	5.79	0.428	1.46	49.4	7.0	4.1
1.500	-0.250	292.5	5.80	0.428	1.53	42.5	6.7	4.4
1.500	-0.250	337.5	5.80	0.427	1.54	68.7	9.7	6.2
1.500	-0.083	22.5	5.82	0.424	1.56	67.9	10.1	3.7
1.500	-0.083	67.5	5.81	0.425	1.52	59.4	8.5	4.5
1.500	-0.083	112.5	5.81	0.424	1.46	59.1	8.1	4.5
1.500	-0.083	157.5	5.81	0.425	1.50	71.5	9.6	4.2
1.500	-0.083	202.5	5.81	0.425	1.47	76.9	9.7	7.7
1.500	-0.083	247.5	5.80	0.426	1.49	59.1	7.4	4.7
1.500	-0.083	292.5	5.81	0.426	1.49	64.9	8.3	4.9
1.500	-0.083	337.5	5.81	0.426	1.51	64.3	9.6	5.8
1.500	0.083	22.5	5.82	0.424	1.53	82.9	10.8	7.5
1.500	0.083	67.5	5.81	0.426	1.49	60.9	8.7	3.9
1.500	0.083	112.5	5.81	0.426	1.50	74.4	9.3	4.7
1.500	0.083	157.5	5.80	0.426	1.47	81.2	10.5	5.2
1.500	0.083	202.5	5.80	0.427	1.47	64.9	9.3	5.3
1.500	0.083	247.5	5.81	0.426	1.49	65.1	8.1	6.3
1.500	0.083	292.5	5.81	0.425	1.49	58.6	8.4	3.5
1.500	0.083	337.5	5.82	0.424	1.51	54.2	9.2	3.3
1.500	0.250	22.5	5.81	0.427	1.51	68.9	10.4	6.6
1.500	0.250	67.5	5.80	0.428	1.48	57.7	9.0	3.8
1.500	0.250	112.5	5.80	0.427	1.43	70.0	9.5	4.6

W [GeV]	cosθ^*_η	ϕ_η [deg.]	$\langle Q^2_{\mathrm{bin}}\rangle$ $[\frac{\mathrm{GeV}^2}{\mathrm{c}^2}]$	$\langle\epsilon\rangle$	rad. corr.	$\frac{d^2\sigma}{d\Omega^*_\eta}$ $[\frac{n\mathrm{b}}{\mathrm{sr}}]$	δ_{stat} $[\frac{n\mathrm{b}}{\mathrm{sr}}]$	δ_{syst} $[\frac{n\mathrm{b}}{\mathrm{sr}}]$
1.500	0.250	157.5	5.79	0.429	1.46	77.5	10.3	6.5
1.500	0.250	202.5	5.80	0.427	1.47	70.5	9.7	3.4
1.500	0.250	247.5	5.80	0.427	1.48	49.6	7.9	4.5
1.500	0.250	292.5	5.80	0.427	1.49	61.3	9.3	4.6
1.500	0.250	337.5	5.81	0.426	1.51	62.4	10.2	6.3
1.500	0.417	22.5	5.81	0.427	1.52	60.4	10.1	4.2
1.500	0.417	67.5	5.80	0.428	1.50	73.5	10.1	5.9
1.500	0.417	112.5	5.80	0.427	1.47	71.5	8.9	5.6
1.500	0.417	157.5	5.80	0.427	1.45	61.7	9.9	5.4
1.500	0.417	202.5	5.81	0.426	1.43	66.3	9.7	3.6
1.500	0.417	247.5	5.81	0.427	1.49	63.3	8.5	4.9
1.500	0.417	292.5	5.80	0.428	1.48	45.4	8.4	2.9
1.500	0.417	337.5	5.81	0.426	1.51	66.4	10.6	4.4
1.500	0.583	22.5	5.81	0.427	1.50	61.9	10.2	5.6
1.500	0.583	67.5	5.81	0.427	1.47	73.6	9.8	4.4
1.500	0.583	112.5	5.81	0.426	1.45	66.9	9.0	5.1
1.500	0.583	157.5	5.80	0.427	1.45	66.1	9.7	4.3
1.500	0.583	202.5	5.80	0.427	1.46	80.5	10.5	5.2
1.500	0.583	247.5	5.81	0.426	1.47	79.9	9.7	4.0
1.500	0.583	292.5	5.80	0.428	1.47	66.9	9.7	4.1
1.500	0.583	337.5	5.81	0.426	1.48	71.5	10.8	5.0
1.500	0.750	22.5	5.81	0.427	1.43	63.0	10.6	4.6
1.500	0.750	67.5	5.80	0.428	1.47	50.8	8.8	3.7
1.500	0.750	112.5	5.80	0.427	1.42	70.3	9.4	5.8
1.500	0.750	157.5	5.81	0.426	1.43	68.3	9.9	5.2

W [GeV]	cosθ^*_η	ϕ_η [deg.]	$\langle Q^2_{\text{bin}} \rangle$ $[\frac{\text{GeV}^2}{\text{c}^2}]$	$\langle \epsilon \rangle$	rad. corr.	$\frac{d^2\sigma}{d\Omega^*_\eta}$ $[\frac{n\text{b}}{\text{sr}}]$	δ_{stat} $[\frac{n\text{b}}{\text{sr}}]$	δ_{syst} $[\frac{n\text{b}}{\text{sr}}]$
1.500	0.750	202.5	5.81	0.426	1.42	70.6	10.3	5.2
1.500	0.750	247.5	5.81	0.425	1.46	66.5	9.5	4.5
1.500	0.750	292.5	5.80	0.427	1.45	87.3	10.6	5.6
1.500	0.750	337.5	5.80	0.427	1.48	75.8	11.4	4.0
1.500	0.917	22.5	5.79	0.429	1.47	77.5	11.2	4.4
1.500	0.917	67.5	5.81	0.427	1.44	79.6	10.8	5.7
1.500	0.917	112.5	5.81	0.426	1.45	70.1	10.5	4.5
1.500	0.917	157.5	5.81	0.426	1.40	80.2	10.7	6.4
1.500	0.917	202.5	5.81	0.427	1.44	73.0	10.6	4.1
1.500	0.917	247.5	5.81	0.426	1.42	70.4	10.2	5.4
1.500	0.917	292.5	5.80	0.427	1.45	60.6	10.2	4.2
1.500	0.917	337.5	5.80	0.427	1.47	65.8	11.3	4.5
1.530	-0.917	22.5	5.75	0.426	1.44	74.6	7.8	5.4
1.530	-0.917	67.5	5.76	0.425	1.40	62.4	6.9	7.5
1.530	-0.917	112.5	5.76	0.424	1.38	64.0	7.2	4.7
1.530	-0.917	157.5	5.76	0.424	1.41	57.9	6.6	6.5
1.530	-0.917	202.5	5.76	0.424	1.37	62.1	6.9	5.3
1.530	-0.917	247.5	5.76	0.424	1.40	70.1	7.1	4.2
1.530	-0.917	292.5	5.76	0.424	1.42	74.3	7.6	5.0
1.530	-0.917	337.5	5.75	0.425	1.42	70.1	7.5	4.1
1.530	-0.750	22.5	5.77	0.423	1.42	72.1	7.4	5.3
1.530	-0.750	67.5	5.76	0.425	1.42	62.8	7.0	4.1
1.530	-0.750	112.5	5.75	0.424	1.38	78.2	7.6	4.6
1.530	-0.750	157.5	5.75	0.425	1.36	68.8	7.0	5.9
1.530	-0.750	202.5	5.75	0.425	1.34	71.7	7.1	4.4

W	$\cos\theta^*_\eta$	ϕ_η	$\langle Q^2_{\text{bin}}\rangle$	$\langle\epsilon\rangle$	rad. corr.	$\frac{d^2\sigma}{d\Omega^*_\eta}$	δ_{stat}	δ_{syst}
[GeV]		[deg.]	$[\frac{\text{GeV}^2}{\text{c}^2}]$			$[\frac{n\text{b}}{\text{sr}}]$	$[\frac{n\text{b}}{\text{sr}}]$	$[\frac{n\text{b}}{\text{sr}}]$
1.530	-0.750	247.5	5.76	0.424	1.38	51.4	6.0	3.9
1.530	-0.750	292.5	5.76	0.424	1.37	67.9	7.0	3.9
1.530	-0.750	337.5	5.77	0.423	1.41	64.3	6.9	4.8
1.530	-0.583	22.5	5.77	0.422	1.41	74.2	8.1	4.3
1.530	-0.583	67.5	5.76	0.424	1.40	63.9	7.7	4.0
1.530	-0.583	112.5	5.76	0.424	1.38	68.0	7.8	5.5
1.530	-0.583	157.5	5.75	0.425	1.36	74.9	7.5	5.0
1.530	-0.583	202.5	5.75	0.425	1.36	60.9	6.7	4.4
1.530	-0.583	247.5	5.75	0.425	1.34	69.1	7.1	5.9
1.530	-0.583	292.5	5.77	0.423	1.38	69.1	7.5	4.3
1.530	-0.583	337.5	5.77	0.422	1.42	61.9	7.3	4.3
1.530	-0.417	22.5	5.76	0.424	1.40	79.8	8.6	5.4
1.530	-0.417	67.5	5.76	0.423	1.37	60.0	7.7	2.9
1.530	-0.417	112.5	5.76	0.424	1.34	63.7	7.5	6.0
1.530	-0.417	157.5	5.76	0.424	1.36	84.9	8.4	5.7
1.530	-0.417	202.5	5.76	0.424	1.32	77.4	7.7	4.1
1.530	-0.417	247.5	5.75	0.425	1.33	75.3	7.6	4.7
1.530	-0.417	292.5	5.77	0.423	1.33	81.2	8.3	4.4
1.530	-0.417	337.5	5.76	0.423	1.41	70.9	8.0	5.0
1.530	-0.250	22.5	5.75	0.425	1.43	88.8	9.9	5.2
1.530	-0.250	67.5	5.77	0.422	1.38	56.2	7.7	4.6
1.530	-0.250	112.5	5.77	0.422	1.32	68.2	8.3	4.2
1.530	-0.250	157.5	5.76	0.423	1.32	69.0	8.2	4.1
1.530	-0.250	202.5	5.76	0.423	1.35	77.5	8.2	4.9
1.530	-0.250	247.5	5.76	0.424	1.30	70.0	7.8	4.8

W	$\cos\theta_\eta^*$	ϕ_η	$\langle Q^2_{\text{bin}}\rangle$	$\langle\epsilon\rangle$	rad. corr.	$\frac{d^2\sigma}{d\Omega_\eta^*}$	δ_{stat}	δ_{syst}
[GeV]		[deg.]	$[\frac{\text{GeV}^2}{\text{c}^2}]$			$[\frac{n\text{b}}{\text{sr}}]$	$[\frac{n\text{b}}{\text{sr}}]$	$[\frac{n\text{b}}{\text{sr}}]$
1.530	-0.250	292.5	5.77	0.422	1.34	69.2	8.0	3.6
1.530	-0.250	337.5	5.75	0.425	1.44	77.0	9.1	4.6
1.530	-0.083	22.5	5.76	0.424	1.42	69.7	9.9	4.2
1.530	-0.083	67.5	5.78	0.421	1.33	70.4	8.9	4.3
1.530	-0.083	112.5	5.78	0.421	1.30	58.1	7.7	3.3
1.530	-0.083	157.5	5.76	0.423	1.33	93.8	10.0	4.5
1.530	-0.083	202.5	5.76	0.423	1.33	72.1	8.6	3.7
1.530	-0.083	247.5	5.76	0.424	1.31	58.3	7.7	3.8
1.530	-0.083	292.5	5.77	0.423	1.32	62.1	8.1	3.2
1.530	-0.083	337.5	5.76	0.424	1.42	86.4	10.6	6.0
1.530	0.083	22.5	5.76	0.426	1.38	70.9	10.6	3.7
1.530	0.083	67.5	5.77	0.424	1.34	48.5	8.5	2.4
1.530	0.083	112.5	5.76	0.425	1.28	68.4	8.9	4.0
1.530	0.083	157.5	5.76	0.423	1.33	66.5	9.4	4.0
1.530	0.083	202.5	5.77	0.422	1.30	68.4	8.8	5.1
1.530	0.083	247.5	5.77	0.423	1.26	60.9	8.2	3.7
1.530	0.083	292.5	5.77	0.423	1.33	67.5	9.5	3.6
1.530	0.083	337.5	5.77	0.424	1.39	70.4	10.1	4.2
1.530	0.250	22.5	5.76	0.425	1.38	93.6	10.9	5.1
1.530	0.250	67.5	5.77	0.423	1.30	68.2	9.8	4.1
1.530	0.250	112.5	5.77	0.423	1.29	77.7	9.6	4.0
1.530	0.250	157.5	5.76	0.423	1.30	73.4	9.8	3.6
1.530	0.250	202.5	5.76	0.424	1.29	76.9	9.7	3.9
1.530	0.250	247.5	5.77	0.423	1.27	70.3	9.1	3.3
1.530	0.250	292.5	5.77	0.423	1.31	67.2	9.7	3.4

W [GeV]	$\cos\theta^*_\eta$	ϕ_η [deg.]	$\langle Q^2_{\text{bin}}\rangle$ [$\frac{\text{GeV}^2}{\text{c}^2}$]	$\langle\epsilon\rangle$	rad. corr.	$\frac{d^2\sigma}{d\Omega^*_\eta}$ [$\frac{nb}{\text{sr}}$]	δ_{stat} [$\frac{nb}{\text{sr}}$]	δ_{syst} [$\frac{nb}{\text{sr}}$]
1.530	0.250	337.5	5.76	0.425	1.40	81.6	10.4	3.9
1.530	0.417	22.5	5.76	0.425	1.37	72.1	9.4	4.5
1.530	0.417	67.5	5.77	0.423	1.30	59.6	8.7	3.5
1.530	0.417	112.5	5.77	0.423	1.27	68.0	8.6	3.2
1.530	0.417	157.5	5.77	0.423	1.30	95.3	9.9	6.3
1.530	0.417	202.5	5.77	0.423	1.30	91.2	9.6	5.8
1.530	0.417	247.5	5.77	0.422	1.29	75.0	8.5	4.4
1.530	0.417	292.5	5.77	0.423	1.32	84.1	9.7	5.0
1.530	0.417	337.5	5.77	0.424	1.38	94.7	10.3	4.8
1.530	0.583	22.5	5.77	0.423	1.36	77.4	11.2	5.6
1.530	0.583	67.5	5.77	0.423	1.27	81.7	10.4	4.7
1.530	0.583	112.5	5.77	0.422	1.28	63.0	8.8	4.7
1.530	0.583	157.5	5.77	0.422	1.30	84.8	10.5	4.6
1.530	0.583	202.5	5.77	0.423	1.30	95.2	11.1	4.6
1.530	0.583	247.5	5.77	0.423	1.29	94.1	10.2	5.4
1.530	0.583	292.5	5.76	0.424	1.32	84.2	10.8	6.0
1.530	0.583	337.5	5.77	0.423	1.40	72.9	10.5	3.7
1.530	0.750	22.5	5.79	0.421	1.33	87.7	12.3	4.7
1.530	0.750	67.5	5.77	0.423	1.31	73.2	11.0	4.4
1.530	0.750	112.5	5.77	0.423	1.28	75.5	10.6	3.7
1.530	0.750	157.5	5.77	0.422	1.29	93.1	11.7	7.2
1.530	0.750	202.5	5.77	0.423	1.32	77.5	10.8	4.3
1.530	0.750	247.5	5.77	0.423	1.32	82.0	10.1	4.6
1.530	0.750	292.5	5.77	0.423	1.32	68.4	10.8	5.0
1.530	0.750	337.5	5.79	0.421	1.35	78.4	11.3	6.3

W [GeV]	$\cos\theta^*_\eta$	ϕ_η [deg.]	$\langle Q^2_{\text{bin}}\rangle$ $[\frac{\text{GeV}^2}{\text{c}^2}]$	$\langle\epsilon\rangle$	rad. corr.	$\frac{d^2\sigma}{d\Omega^*_\eta}$ $[\frac{nb}{\text{sr}}]$	δ_{stat} $[\frac{nb}{\text{sr}}]$	δ_{syst} $[\frac{nb}{\text{sr}}]$
1.530	0.917	22.5	5.78	0.423	1.31	94.7	12.6	7.5
1.530	0.917	67.5	5.76	0.425	1.31	86.5	11.8	5.7
1.530	0.917	112.5	5.77	0.424	1.31	104.3	11.6	6.2
1.530	0.917	157.5	5.77	0.423	1.30	77.4	10.5	5.2
1.530	0.917	202.5	5.77	0.423	1.31	106.5	11.6	5.9
1.530	0.917	247.5	5.77	0.423	1.31	102.1	11.5	5.1
1.530	0.917	292.5	5.77	0.424	1.31	77.8	11.2	4.6
1.530	0.917	337.5	5.77	0.423	1.31	106.0	12.8	7.4
1.560	-0.917	22.5	5.70	0.421	1.38	67.3	7.1	4.7
1.560	-0.917	67.5	5.70	0.421	1.36	62.2	7.0	3.7
1.560	-0.917	112.5	5.70	0.420	1.35	62.5	7.0	4.4
1.560	-0.917	157.5	5.69	0.422	1.33	67.8	7.0	4.4
1.560	-0.917	202.5	5.69	0.422	1.32	55.5	6.2	3.2
1.560	-0.917	247.5	5.70	0.421	1.34	59.5	6.2	4.3
1.560	-0.917	292.5	5.69	0.422	1.36	54.1	6.1	3.5
1.560	-0.917	337.5	5.70	0.420	1.38	55.7	6.6	3.2
1.560	-0.750	22.5	5.70	0.422	1.34	60.3	6.6	2.9
1.560	-0.750	67.5	5.69	0.422	1.32	53.6	6.3	3.8
1.560	-0.750	112.5	5.69	0.423	1.28	50.0	5.9	4.6
1.560	-0.750	157.5	5.68	0.423	1.25	54.2	6.1	3.8
1.560	-0.750	202.5	5.69	0.422	1.24	50.9	5.6	3.1
1.560	-0.750	247.5	5.69	0.422	1.31	54.6	5.9	2.8
1.560	-0.750	292.5	5.70	0.420	1.32	50.1	5.8	3.1
1.560	-0.750	337.5	5.70	0.421	1.35	52.9	6.1	2.8
1.560	-0.583	22.5	5.69	0.423	1.39	49.3	6.5	2.6

W [GeV]	$\cos\theta^*_\eta$	ϕ_η [deg.]	$\langle Q^2_{\text{bin}}\rangle$ $[\frac{\text{GeV}^2}{\text{c}^2}]$	$\langle\epsilon\rangle$	rad. corr.	$\frac{d^2\sigma}{d\Omega^*_\eta}$ $[\frac{nb}{\text{sr}}]$	δ_{stat} $[\frac{nb}{\text{sr}}]$	δ_{syst} $[\frac{nb}{\text{sr}}]$
1.560	-0.583	67.5	5.71	0.420	1.34	46.8	6.9	2.9
1.560	-0.583	112.5	5.70	0.422	1.24	44.9	6.6	3.9
1.560	-0.583	157.5	5.70	0.421	1.27	49.4	6.1	3.4
1.560	-0.583	202.5	5.69	0.421	1.24	54.0	6.0	2.8
1.560	-0.583	247.5	5.70	0.421	1.26	42.0	5.8	2.5
1.560	-0.583	292.5	5.71	0.419	1.30	55.6	6.8	2.8
1.560	-0.583	337.5	5.69	0.422	1.36	52.5	6.4	2.8
1.560	-0.417	22.5	5.68	0.425	1.33	45.1	7.4	2.8
1.560	-0.417	67.5	5.72	0.419	1.26	49.9	7.7	2.9
1.560	-0.417	112.5	5.70	0.421	1.23	43.7	7.0	2.7
1.560	-0.417	157.5	5.69	0.421	1.26	53.6	6.9	3.0
1.560	-0.417	202.5	5.70	0.420	1.24	57.5	6.8	3.7
1.560	-0.417	247.5	5.69	0.422	1.17	38.6	6.3	3.0
1.560	-0.417	292.5	5.72	0.419	1.24	46.3	6.9	3.1
1.560	-0.417	337.5	5.68	0.425	1.30	52.6	7.5	2.9
1.560	-0.250	22.5	5.68	0.424	1.28	54.9	9.1	2.9
1.560	-0.250	67.5	5.71	0.419	1.20	42.9	7.5	3.1
1.560	-0.250	112.5	5.70	0.420	1.16	40.5	7.2	2.1
1.560	-0.250	157.5	5.69	0.421	1.22	56.5	7.6	2.7
1.560	-0.250	202.5	5.70	0.420	1.23	59.6	7.1	4.3
1.560	-0.250	247.5	5.71	0.419	1.16	51.1	7.2	2.9
1.560	-0.250	292.5	5.72	0.419	1.20	40.8	6.9	4.5
1.560	-0.250	337.5	5.68	0.425	1.30	41.6	8.1	3.1
1.560	-0.083	22.5	5.70	0.422	1.27	54.3	10.3	3.6
1.560	-0.083	67.5	5.73	0.417	1.15	32.9	8.1	2.2

W [GeV]	$\cos\theta^*_\eta$	ϕ_η [deg.]	$\langle Q^2_{\text{bin}}\rangle$ $[\frac{\text{GeV}^2}{\text{c}^2}]$	$\langle\epsilon\rangle$	rad. corr.	$\frac{d^2\sigma}{d\Omega^*_\eta}$ $[\frac{nb}{\text{sr}}]$	δ_{stat} $[\frac{nb}{\text{sr}}]$	δ_{syst} $[\frac{nb}{\text{sr}}]$
1.560	-0.083	112.5	5.72	0.419	1.06	38.8	7.5	4.1
1.560	-0.083	157.5	5.71	0.419	1.21	64.5	8.7	4.1
1.560	-0.083	202.5	5.70	0.420	1.19	57.9	7.9	3.3
1.560	-0.083	247.5	5.72	0.420	1.07	70.5	9.5	3.9
1.560	-0.083	292.5	5.72	0.420	1.17	51.9	8.8	3.4
1.560	-0.083	337.5	5.69	0.423	1.26	41.8	8.8	2.9
1.560	0.083	22.5	5.68	0.426	1.24	61.5	10.1	3.2
1.560	0.083	67.5	5.72	0.420	1.10	48.4	10.5	2.8
1.560	0.083	112.5	5.72	0.419	1.00	50.7	10.3	5.6
1.560	0.083	157.5	5.69	0.421	1.19	56.0	9.2	3.3
1.560	0.083	202.5	5.70	0.420	1.19	60.6	8.7	3.3
1.560	0.083	247.5	5.74	0.418	1.02	44.3	8.9	3.3
1.560	0.083	292.5	5.73	0.419	1.11	54.5	10.2	3.2
1.560	0.083	337.5	5.69	0.424	1.27	56.8	9.7	3.4
1.560	0.250	22.5	5.69	0.424	1.23	44.5	9.0	2.5
1.560	0.250	67.5	5.73	0.419	1.06	30.8	9.7	2.0
1.560	0.250	112.5	5.74	0.417	0.98	47.0	9.9	2.7
1.560	0.250	157.5	5.70	0.420	1.14	43.3	8.8	2.6
1.560	0.250	202.5	5.70	0.421	1.16	48.1	8.4	3.2
1.560	0.250	247.5	5.74	0.417	0.99	51.9	9.4	2.7
1.560	0.250	292.5	5.74	0.418	1.07	55.8	10.8	2.8
1.560	0.250	337.5	5.69	0.424	1.25	47.9	9.1	2.2
1.560	0.417	22.5	5.69	0.424	1.20	49.5	9.5	2.6
1.560	0.417	67.5	5.73	0.418	1.05	49.8	10.7	3.1
1.560	0.417	112.5	5.73	0.418	1.00	48.4	9.4	4.8

W [GeV]	$\cos\theta^*_\eta$	ϕ_η [deg.]	$\langle Q^2_{\text{bin}}\rangle$ $[\frac{\text{GeV}^2}{\text{c}^2}]$	$\langle\epsilon\rangle$	rad. corr.	$\frac{d^2\sigma}{d\Omega^*_\eta}$ $[\frac{n\text{b}}{\text{sr}}]$	δ_{stat} $[\frac{n\text{b}}{\text{sr}}]$	δ_{syst} $[\frac{n\text{b}}{\text{sr}}]$
1.560	0.417	157.5	5.70	0.420	1.13	51.8	9.3	3.1
1.560	0.417	202.5	5.70	0.420	1.13	50.0	8.8	4.8
1.560	0.417	247.5	5.73	0.418	1.01	53.0	9.4	4.1
1.560	0.417	292.5	5.73	0.418	1.10	55.3	10.3	3.6
1.560	0.417	337.5	5.69	0.424	1.25	64.1	9.7	3.7
1.560	0.583	22.5	5.71	0.420	1.17	65.6	11.9	4.3
1.560	0.583	67.5	5.74	0.416	1.05	61.8	11.8	4.0
1.560	0.583	112.5	5.72	0.418	1.03	53.2	10.8	2.9
1.560	0.583	157.5	5.71	0.419	1.11	56.0	11.3	4.5
1.560	0.583	202.5	5.71	0.419	1.13	53.0	10.3	2.5
1.560	0.583	247.5	5.72	0.418	1.05	44.3	10.1	3.8
1.560	0.583	292.5	5.74	0.417	1.08	54.8	11.3	3.4
1.560	0.583	337.5	5.71	0.421	1.21	63.4	11.0	3.3
1.560	0.750	22.5	5.71	0.421	1.12	75.8	14.4	5.6
1.560	0.750	67.5	5.70	0.422	1.09	67.5	13.0	4.2
1.560	0.750	112.5	5.70	0.421	1.08	62.0	11.2	4.2
1.560	0.750	157.5	5.71	0.420	1.14	60.4	10.6	2.8
1.560	0.750	202.5	5.71	0.420	1.15	67.9	10.3	3.5
1.560	0.750	247.5	5.72	0.419	1.12	67.2	10.1	5.5
1.560	0.750	292.5	5.71	0.420	1.13	65.2	11.6	4.2
1.560	0.750	337.5	5.73	0.419	1.12	86.2	13.5	4.0
1.560	0.917	22.5	5.69	0.424	1.19	88.8	14.5	4.3
1.560	0.917	67.5	5.69	0.424	1.17	87.7	13.1	4.9
1.560	0.917	112.5	5.70	0.422	1.17	65.3	11.6	4.4
1.560	0.917	157.5	5.70	0.422	1.18	72.7	11.8	3.6

W [GeV]	$\cos\theta^*_\eta$	ϕ_η [deg.]	$\langle Q^2_{\text{bin}} \rangle$ $[\frac{\text{GeV}^2}{\text{c}^2}]$	$\langle\epsilon\rangle$	rad. corr.	$\frac{d^2\sigma}{d\Omega^*_\eta}$ $[\frac{nb}{\text{sr}}]$	δ_{stat} $[\frac{nb}{\text{sr}}]$	δ_{syst} $[\frac{nb}{\text{sr}}]$
1.560	0.917	202.5	5.70	0.421	1.17	67.3	11.2	3.8
1.560	0.917	247.5	5.70	0.422	1.19	64.9	11.1	4.4
1.560	0.917	292.5	5.69	0.424	1.18	81.9	12.9	4.5
1.560	0.917	337.5	5.69	0.425	1.21	77.9	14.3	4.5
1.590	-0.917	22.5	5.64	0.417	1.41	61.2	6.6	3.9
1.590	-0.917	67.5	5.63	0.418	1.37	46.9	6.2	2.6
1.590	-0.917	112.5	5.63	0.418	1.32	63.8	7.2	5.0
1.590	-0.917	157.5	5.63	0.419	1.33	37.4	5.8	2.9
1.590	-0.917	202.5	5.63	0.419	1.32	45.1	5.8	3.0
1.590	-0.917	247.5	5.63	0.418	1.29	41.3	5.5	2.3
1.590	-0.917	292.5	5.63	0.420	1.34	42.4	5.6	2.7
1.590	-0.917	337.5	5.64	0.417	1.38	42.5	5.5	2.6
1.590	-0.750	22.5	5.62	0.421	1.31	49.0	6.2	2.8
1.590	-0.750	67.5	5.64	0.418	1.29	47.8	6.3	3.2
1.590	-0.750	112.5	5.63	0.418	1.24	49.0	6.3	2.9
1.590	-0.750	157.5	5.63	0.419	1.21	47.4	5.8	2.6
1.590	-0.750	202.5	5.63	0.419	1.22	40.4	5.1	3.1
1.590	-0.750	247.5	5.63	0.419	1.22	29.3	4.8	2.1
1.590	-0.750	292.5	5.64	0.417	1.28	30.0	4.8	1.5
1.590	-0.750	337.5	5.62	0.420	1.32	37.9	5.2	2.3
1.590	-0.583	22.5	5.61	0.422	1.31	45.4	6.8	2.4
1.590	-0.583	67.5	5.64	0.418	1.28	34.8	6.1	2.9
1.590	-0.583	112.5	5.64	0.417	1.25	32.8	5.9	3.5
1.590	-0.583	157.5	5.63	0.418	1.22	38.8	5.5	2.8
1.590	-0.583	202.5	5.63	0.418	1.22	33.6	5.1	2.8

W [GeV]	$\cos\theta^*_\eta$	ϕ_η [deg.]	$\langle Q^2_{\text{bin}} \rangle$ $[\frac{\text{GeV}^2}{\text{c}^2}]$	$\langle \epsilon \rangle$	rad. corr.	$\frac{d^2\sigma}{d\Omega^*_\eta}$ $[\frac{nb}{\text{sr}}]$	δ_{stat} $[\frac{nb}{\text{sr}}]$	δ_{syst} $[\frac{nb}{\text{sr}}]$
1.590	-0.583	247.5	5.63	0.419	1.19	43.3	6.6	3.3
1.590	-0.583	292.5	5.64	0.418	1.24	39.1	6.2	2.6
1.590	-0.583	337.5	5.62	0.421	1.34	39.1	6.3	2.3
1.590	-0.417	22.5	5.62	0.421	1.27	35.5	8.0	3.7
1.590	-0.417	67.5	5.65	0.417	1.15	16.3	5.9	1.8
1.590	-0.417	112.5	5.64	0.418	1.09	23.0	6.0	2.7
1.590	-0.417	157.5	5.63	0.417	1.19	43.1	6.4	3.9
1.590	-0.417	202.5	5.63	0.419	1.19	37.9	6.0	2.8
1.590	-0.417	247.5	5.65	0.416	1.08	36.5	7.2	2.3
1.590	-0.417	292.5	5.65	0.417	1.16	30.9	6.9	1.9
1.590	-0.417	337.5	5.62	0.421	1.29	33.5	7.5	2.4
1.590	-0.250	22.5	5.61	0.423	1.26	32.9	9.6	2.4
1.590	-0.250	67.5	5.66	0.416	1.08	21.6	7.8	2.1
1.590	-0.250	112.5	5.65	0.416	1.06	22.7	7.1	2.9
1.590	-0.250	157.5	5.63	0.418	1.18	35.6	7.0	2.1
1.590	-0.250	202.5	5.62	0.419	1.15	33.2	6.6	2.1
1.590	-0.250	247.5	5.66	0.415	1.01	31.9	7.8	4.0
1.590	-0.250	292.5	5.65	0.417	1.11	38.7	8.7	4.1
1.590	-0.250	337.5	5.61	0.424	1.27	35.7	9.0	2.4
1.590	-0.083	22.5	5.59	0.427	1.18	21.0	9.2	3.2
1.590	-0.083	67.5	5.65	0.417	0.95	19.3	9.2	1.2
1.590	-0.083	112.5	5.68	0.414	0.86	22.3	8.9	2.0
1.590	-0.083	157.5	5.64	0.416	1.13	32.4	7.7	1.9
1.590	-0.083	202.5	5.63	0.418	1.12	40.1	7.2	2.9
1.590	-0.083	247.5	5.67	0.416	0.89	32.8	9.7	4.3

W [GeV]	$\cos\theta^*_\eta$	ϕ_η [deg.]	$\langle Q^2_{\text{bin}} \rangle$ $[\frac{\text{GeV}^2}{\text{c}^2}]$	$\langle \epsilon \rangle$	rad. corr.	$\frac{d^2\sigma}{d\Omega^*_\eta}$ $[\frac{nb}{\text{sr}}]$	δ_{stat} $[\frac{nb}{\text{sr}}]$	δ_{syst} $[\frac{nb}{\text{sr}}]$
1.590	-0.083	292.5	5.67	0.415	0.98	27.1	9.3	5.0
1.590	-0.083	337.5	5.59	0.427	1.21	33.4	9.9	3.1
1.590	0.083	22.5	5.58	0.431	1.15	29.2	9.9	1.9
1.590	0.083	112.5	5.64	0.419	0.75	26.2	11.5	6.0
1.590	0.083	157.5	5.63	0.419	1.12	33.7	8.3	2.3
1.590	0.083	202.5	5.63	0.417	1.11	35.6	8.1	1.9
1.590	0.083	247.5	5.68	0.415	0.79	35.4	13.2	4.7
1.590	0.083	292.5	5.67	0.417	0.88	48.8	14.3	5.7
1.590	0.083	337.5	5.57	0.431	1.16	55.6	11.9	5.3
1.590	0.250	22.5	5.58	0.431	1.07	30.3	11.5	4.6
1.590	0.250	112.5	5.65	0.417	0.66	24.2	13.1	4.1
1.590	0.250	157.5	5.63	0.417	1.05	25.0	8.9	3.7
1.590	0.250	202.5	5.63	0.418	1.06	36.7	8.7	3.3
1.590	0.250	247.5	5.67	0.416	0.70	37.9	13.0	3.8
1.590	0.250	292.5	5.68	0.415	0.87	22.7	11.0	2.2
1.590	0.250	337.5	5.59	0.429	1.08	41.8	11.4	3.9
1.590	0.417	22.5	5.59	0.429	1.09	45.2	13.0	3.1
1.590	0.417	67.5	5.68	0.414	0.77	39.0	14.3	4.0
1.590	0.417	112.5	5.67	0.415	0.68	39.2	13.8	5.5
1.590	0.417	157.5	5.65	0.416	1.05	27.4	9.9	2.4
1.590	0.417	202.5	5.65	0.416	1.07	40.7	9.8	2.5
1.590	0.417	247.5	5.64	0.419	0.75	25.8	12.8	2.4
1.590	0.417	292.5	5.67	0.417	0.86	52.8	14.9	5.9
1.590	0.417	337.5	5.58	0.431	1.06	48.7	12.7	3.7
1.590	0.583	22.5	5.65	0.419	0.92	51.5	17.1	4.5

W	$\cos\theta^*_\eta$	ϕ_η	$\langle Q^2_{\text{bin}} \rangle$	$\langle \epsilon \rangle$	rad. corr.	$\frac{d^2\sigma}{d\Omega^*_\eta}$	δ_{stat}	δ_{syst}
[GeV]		[deg.]	$[\frac{\text{GeV}^2}{\text{c}^2}]$			$[\frac{nb}{\text{sr}}]$	$[\frac{nb}{\text{sr}}]$	$[\frac{nb}{\text{sr}}]$
1.590	0.583	67.5	5.71	0.411	0.71	38.5	16.7	4.7
1.590	0.583	112.5	5.67	0.415	0.67	34.2	14.7	4.9
1.590	0.583	157.5	5.64	0.417	1.00	38.1	11.8	3.5
1.590	0.583	202.5	5.64	0.417	1.02	31.6	10.3	2.1
1.590	0.583	247.5	5.66	0.415	0.76	47.7	14.8	4.0
1.590	0.583	292.5	5.71	0.410	0.81	52.4	17.0	4.1
1.590	0.583	337.5	5.65	0.420	0.95	31.3	13.1	5.4
1.590	0.750	22.5	5.60	0.426	0.92	58.3	22.2	13.0
1.590	0.750	67.5	5.63	0.420	0.85	29.3	15.9	4.1
1.590	0.750	112.5	5.65	0.417	0.89	30.4	11.5	4.0
1.590	0.750	157.5	5.64	0.417	1.05	29.7	11.1	2.8
1.590	0.750	202.5	5.64	0.417	1.05	35.4	10.1	2.6
1.590	0.750	247.5	5.65	0.416	0.94	39.1	11.9	3.1
1.590	0.750	292.5	5.63	0.421	0.92	61.9	16.8	3.5
1.590	0.750	337.5	5.61	0.426	0.91	67.8	20.9	7.2
1.590	0.917	67.5	5.66	0.415	1.03	25.0	14.4	4.0
1.590	0.917	112.5	5.66	0.415	1.03	23.5	12.8	2.4
1.590	0.917	247.5	5.65	0.417	1.05	24.6	12.1	1.6
1.590	0.917	337.5	5.64	0.421	1.05	39.8	18.0	3.0
1.625	-0.917	22.5	5.56	0.414	1.41	33.6	4.7	2.2
1.625	-0.917	67.5	5.56	0.415	1.36	33.2	4.8	3.3
1.625	-0.917	112.5	5.55	0.416	1.34	36.3	5.0	2.1
1.625	-0.917	157.5	5.55	0.415	1.32	24.5	4.4	1.8
1.625	-0.917	202.5	5.55	0.416	1.30	33.9	4.6	2.2
1.625	-0.917	247.5	5.55	0.415	1.32	23.4	4.0	1.7

W [GeV]	$\cos\theta^*_\eta$	ϕ_η [deg.]	$\langle Q^2_{\text{bin}}\rangle$ $[\frac{\text{GeV}^2}{\text{c}^2}]$	$\langle\epsilon\rangle$	rad. corr.	$\frac{d^2\sigma}{d\Omega^*_\eta}$ $[\frac{nb}{\text{sr}}]$	δ_{stat} $[\frac{nb}{\text{sr}}]$	δ_{syst} $[\frac{nb}{\text{sr}}]$
1.625	-0.917	292.5	5.55	0.416	1.33	32.2	4.4	2.0
1.625	-0.917	337.5	5.56	0.415	1.40	28.2	4.3	2.8
1.625	-0.750	22.5	5.54	0.419	1.35	37.2	5.5	2.2
1.625	-0.750	67.5	5.56	0.414	1.30	27.7	4.8	1.7
1.625	-0.750	112.5	5.56	0.415	1.24	37.3	5.5	2.9
1.625	-0.750	157.5	5.55	0.415	1.23	35.4	4.9	2.5
1.625	-0.750	202.5	5.55	0.415	1.21	24.8	4.1	1.3
1.625	-0.750	247.5	5.55	0.416	1.21	36.4	4.9	2.6
1.625	-0.750	292.5	5.57	0.414	1.28	23.5	4.2	1.8
1.625	-0.750	337.5	5.54	0.419	1.33	30.4	4.8	1.7
1.625	-0.583	22.5	5.53	0.420	1.33	35.0	6.3	2.2
1.625	-0.583	67.5	5.57	0.415	1.24	25.6	5.9	3.6
1.625	-0.583	112.5	5.55	0.417	1.17	23.1	5.4	2.3
1.625	-0.583	157.5	5.54	0.417	1.20	34.6	4.9	2.3
1.625	-0.583	202.5	5.55	0.415	1.21	30.9	4.6	1.9
1.625	-0.583	247.5	5.56	0.415	1.13	18.2	4.7	2.2
1.625	-0.583	292.5	5.56	0.416	1.21	18.3	4.9	1.3
1.625	-0.583	337.5	5.54	0.419	1.30	29.5	6.1	2.5
1.625	-0.417	22.5	5.52	0.423	1.25	22.3	7.7	1.7
1.625	-0.417	157.5	5.55	0.415	1.14	28.7	5.6	1.7
1.625	-0.417	202.5	5.55	0.416	1.15	23.3	5.1	1.2
1.625	-0.417	247.5	5.57	0.415	0.93	23.8	6.7	3.1
1.625	-0.417	292.5	5.57	0.414	1.06	14.9	6.5	2.1
1.625	-0.417	337.5	5.52	0.423	1.29	22.7	7.6	1.6
1.625	-0.250	67.5	5.57	0.417	0.90	16.6	8.9	3.2

W [GeV]	$\cos\theta^*_\eta$	ϕ_η [deg.]	$\langle Q^2_{\text{bin}}\rangle$ $[\frac{\text{GeV}^2}{\text{c}^2}]$	$\langle\epsilon\rangle$	rad. corr.	$\frac{d^2\sigma}{d\Omega^*_\eta}$ $[\frac{n\text{b}}{\text{sr}}]$	δ_{stat} $[\frac{n\text{b}}{\text{sr}}]$	δ_{syst} $[\frac{n\text{b}}{\text{sr}}]$
1.625	-0.250	157.5	5.56	0.414	1.15	25.5	6.6	1.4
1.625	-0.250	202.5	5.56	0.414	1.10	23.1	5.8	1.2
1.625	-0.250	247.5	5.56	0.416	0.85	38.6	10.8	5.0
1.625	-0.250	292.5	5.56	0.417	0.96	21.7	9.3	2.5
1.625	-0.083	157.5	5.57	0.412	1.08	15.5	7.1	1.0
1.625	-0.083	202.5	5.57	0.413	1.07	14.4	6.5	1.5
1.625	0.083	157.5	5.56	0.415	1.05	13.5	8.3	1.1
1.625	0.083	202.5	5.56	0.414	1.07	18.8	7.6	1.4
1.625	0.250	157.5	5.56	0.414	1.02	15.9	8.9	2.4
1.625	0.250	202.5	5.56	0.414	1.00	19.2	8.7	1.6
1.625	0.417	202.5	5.57	0.412	0.98	23.7	9.9	2.0
1.625	0.583	202.5	5.57	0.413	0.96	20.3	10.7	1.3
1.625	0.750	112.5	5.62	0.409	0.63	23.3	13.3	1.7
1.665	-0.917	22.5	5.46	0.413	1.39	24.6	4.6	2.0
1.665	-0.917	67.5	5.46	0.412	1.38	20.6	4.7	1.5
1.665	-0.917	112.5	5.45	0.413	1.34	19.3	4.7	2.0
1.665	-0.917	157.5	5.45	0.413	1.32	26.1	4.6	1.7
1.665	-0.917	202.5	5.45	0.413	1.33	15.3	4.0	2.0
1.665	-0.917	247.5	5.45	0.413	1.33	23.9	4.6	1.9
1.665	-0.917	292.5	5.46	0.412	1.35	31.3	4.9	3.4
1.665	-0.917	337.5	5.46	0.413	1.37	21.6	4.3	2.0
1.665	-0.750	22.5	5.45	0.415	1.34	26.5	6.1	1.7
1.665	-0.750	67.5	5.46	0.412	1.31	14.8	4.7	1.7
1.665	-0.750	112.5	5.46	0.412	1.23	17.3	4.7	1.5
1.665	-0.750	157.5	5.46	0.412	1.23	21.8	4.6	1.7

W [GeV]	$\cos\theta^*_\eta$	ϕ_η [deg.]	$\langle Q^2_{\text{bin}} \rangle$ $[\frac{\text{GeV}^2}{\text{c}^2}]$	$\langle \epsilon \rangle$	rad. corr.	$\frac{d^2\sigma}{d\Omega^*_\eta}$ $[\frac{n\text{b}}{\text{sr}}]$	δ_{stat} $[\frac{n\text{b}}{\text{sr}}]$	δ_{syst} $[\frac{n\text{b}}{\text{sr}}]$
1.665	-0.750	202.5	5.46	0.412	1.23	22.2	4.3	1.5
1.665	-0.750	247.5	5.45	0.412	1.20	24.8	4.9	1.9
1.665	-0.750	292.5	5.46	0.412	1.25	25.6	4.8	1.6
1.665	-0.750	337.5	5.44	0.416	1.33	22.7	5.5	2.5
1.665	-0.583	22.5	5.42	0.421	1.31	17.6	7.4	2.8
1.665	-0.583	67.5	5.48	0.412	1.18	16.2	7.2	3.0
1.665	-0.583	112.5	5.48	0.410	1.17	12.7	5.7	2.9
1.665	-0.583	157.5	5.45	0.413	1.21	16.6	5.0	2.0
1.665	-0.583	202.5	5.45	0.413	1.19	18.4	4.7	1.0
1.665	-0.583	247.5	5.49	0.408	1.11	14.0	5.9	1.7
1.665	-0.583	292.5	5.46	0.413	1.19	21.3	7.3	2.0
1.665	-0.583	337.5	5.42	0.420	1.29	17.2	7.4	1.6
1.665	-0.417	157.5	5.46	0.411	1.15	15.2	5.6	1.2
1.665	-0.417	202.5	5.46	0.411	1.16	13.1	5.2	1.1
1.665	-0.250	157.5	5.47	0.409	1.12	11.4	6.4	2.0
1.665	-0.250	202.5	5.47	0.410	1.10	10.4	5.9	2.0
1.705	-0.917	22.5	5.35	0.411	1.39	20.8	5.0	1.4
1.705	-0.917	67.5	5.36	0.409	1.35	18.4	5.1	1.6
1.705	-0.917	112.5	5.36	0.409	1.35	21.2	5.5	1.8
1.705	-0.917	157.5	5.35	0.410	1.33	22.0	4.8	1.5
1.705	-0.917	202.5	5.35	0.410	1.32	21.2	4.6	1.4
1.705	-0.917	247.5	5.35	0.410	1.31	26.5	5.3	2.0
1.705	-0.917	292.5	5.35	0.409	1.33	18.5	4.5	1.2
1.705	-0.917	337.5	5.35	0.411	1.38	24.6	4.8	1.8
1.705	-0.750	22.5	5.34	0.412	1.36	22.7	7.4	1.7

W	$\cos\theta^*_\eta$	ϕ_η	$\langle Q^2_{\text{bin}}\rangle$	$\langle\epsilon\rangle$	rad. corr.	$\frac{d^2\sigma}{d\Omega^*_\eta}$	δ_{stat}	δ_{syst}
[GeV]		[deg.]	$[\frac{\text{GeV}^2}{\text{c}^2}]$			$[\frac{nb}{\text{sr}}]$	$[\frac{nb}{\text{sr}}]$	$[\frac{nb}{\text{sr}}]$
1.705	-0.750	67.5	5.36	0.409	1.27	12.1	5.2	1.6
1.705	-0.750	112.5	5.36	0.408	1.23	15.9	5.3	2.2
1.705	-0.750	157.5	5.35	0.409	1.24	20.6	5.0	1.4
1.705	-0.750	202.5	5.35	0.409	1.24	11.9	4.3	1.5
1.705	-0.750	247.5	5.35	0.409	1.19	17.2	5.3	2.8
1.705	-0.750	292.5	5.35	0.410	1.26	23.2	5.4	1.6
1.705	-0.750	337.5	5.34	0.412	1.35	21.8	6.5	3.1
1.705	-0.583	157.5	5.35	0.410	1.21	13.8	5.8	1.1
1.705	-0.583	202.5	5.35	0.410	1.19	11.9	5.4	1.8
1.745	-0.917	22.5	5.25	0.408	1.41	19.0	5.1	2.1
1.745	-0.917	67.5	5.25	0.407	1.36	16.6	5.3	2.1
1.745	-0.917	112.5	5.25	0.407	1.34	8.2	4.7	1.1
1.745	-0.917	157.5	5.24	0.408	1.32	13.5	4.7	1.3
1.745	-0.917	202.5	5.24	0.407	1.32	13.3	4.6	1.5
1.745	-0.917	247.5	5.25	0.407	1.34	18.7	5.0	2.6
1.745	-0.917	292.5	5.25	0.407	1.37	15.5	4.7	1.2
1.745	-0.917	337.5	5.24	0.409	1.38	17.4	4.8	1.3
1.745	-0.750	22.5	5.22	0.412	1.42	20.9	8.6	4.1
1.745	-0.750	67.5	5.26	0.406	1.29	16.0	5.8	2.2
1.745	-0.750	112.5	5.26	0.407	1.28	12.7	5.5	1.0
1.745	-0.750	157.5	5.25	0.406	1.26	14.1	5.0	1.6
1.745	-0.750	202.5	5.25	0.407	1.24	9.0	4.4	0.7
1.745	-0.750	247.5	5.25	0.407	1.15	9.2	5.2	0.9
1.745	-0.750	292.5	5.25	0.408	1.22	13.7	5.7	2.4
1.745	-0.750	337.5	5.23	0.412	1.33	16.2	8.2	4.7

W [GeV]	$\cos\theta^*_\eta$	ϕ_η [deg.]	$\langle Q^2_{\text{bin}}\rangle$ $[\frac{\text{GeV}^2}{\text{c}^2}]$	$\langle\epsilon\rangle$	rad. corr.	$\frac{d^2\sigma}{d\Omega^*_\eta}$ $[\frac{n\text{b}}{\text{sr}}]$	δ_{stat} $[\frac{n\text{b}}{\text{sr}}]$	δ_{syst} $[\frac{n\text{b}}{\text{sr}}]$
1.785	-0.917	22.5	5.13	0.407	1.37	19.2	5.6	4.4
1.785	-0.917	112.5	5.14	0.405	1.36	11.5	5.4	1.0
1.785	-0.917	247.5	5.14	0.406	1.31	8.8	4.8	0.7
1.785	-0.917	337.5	5.13	0.407	1.38	13.5	5.1	1.9
1.785	-0.750	157.5	5.14	0.404	1.26	14.3	5.4	1.3
1.830	-0.917	22.5	5.02	0.406	1.37	18.4	5.9	1.7
1.830	-0.917	67.5	5.03	0.404	1.37	12.5	5.0	1.4
1.830	-0.917	112.5	5.03	0.404	1.35	17.8	6.2	1.8
1.830	-0.917	247.5	5.02	0.405	1.29	13.4	5.6	1.3
1.830	-0.917	292.5	5.02	0.405	1.35	10.4	5.0	1.2
1.830	-0.917	337.5	5.02	0.405	1.38	9.0	5.1	2.4
1.830	-0.750	157.5	5.03	0.403	1.27	11.4	5.8	0.8

C.2 Higher-Q^2 Data

Table C.2: Higher-Q^2 extracted differential cross-section.

W [GeV]	$\cos\theta^*_\eta$	ϕ_η [deg.]	$\langle Q^2_{\text{bin}}\rangle$ $[\frac{\text{GeV}^2}{\text{c}^2}]$	$\langle\epsilon\rangle$	rad. corr.	$\frac{d^2\sigma}{d\Omega^*_\eta}$ $[\frac{n\text{b}}{\text{sr}}]$	δ_{stat} $[\frac{n\text{b}}{\text{sr}}]$	δ_{syst} $[\frac{n\text{b}}{\text{sr}}]$
1.500	-0.833	36.0	7.04	0.216	1.52	49.4	14.2	3.4
1.500	-0.833	108.0	7.06	0.211	1.56	32.7	7.6	1.5
1.500	-0.833	180.0	7.07	0.210	1.57	36.9	7.8	2.0
1.500	-0.833	252.0	7.06	0.210	1.54	38.9	7.8	2.3
1.500	-0.833	324.0	7.04	0.216	1.53	36.4	12.3	2.0

W [GeV]	$\cos\theta^*_\eta$	ϕ_η [deg.]	$\langle Q^2_{\text{bin}} \rangle$ $[\frac{\text{GeV}^2}{\text{c}^2}]$	$\langle \epsilon \rangle$	rad. corr.	$\frac{d^2\sigma}{d\Omega^*_\eta}$ $[\frac{nb}{\text{sr}}]$	δ_{stat} $[\frac{nb}{\text{sr}}]$	δ_{syst} $[\frac{nb}{\text{sr}}]$
1.500	-0.500	108.0	7.06	0.211	1.53	35.8	8.1	2.0
1.500	-0.500	180.0	7.07	0.210	1.53	36.5	7.8	1.8
1.500	-0.500	252.0	7.06	0.211	1.53	42.6	7.9	2.1
1.500	-0.167	108.0	7.07	0.210	1.52	33.8	9.0	1.9
1.500	-0.167	180.0	7.08	0.208	1.50	40.8	10.5	2.5
1.500	-0.167	252.0	7.07	0.209	1.52	50.0	10.0	3.3
1.500	0.167	180.0	7.07	0.209	1.45	38.0	15.3	2.7
1.500	0.167	252.0	7.06	0.212	1.48	38.5	13.6	2.2
1.530	-0.833	36.0	6.97	0.216	1.30	24.2	11.3	2.1
1.530	-0.833	108.0	7.01	0.209	1.40	38.5	6.6	2.3
1.530	-0.833	180.0	7.01	0.208	1.37	42.6	6.5	2.3
1.530	-0.833	252.0	7.01	0.209	1.38	55.2	7.4	2.7
1.530	-0.833	324.0	6.97	0.216	1.31	43.4	14.2	2.9
1.530	-0.500	108.0	7.00	0.210	1.38	43.1	7.8	1.9
1.530	-0.500	180.0	7.01	0.208	1.36	34.8	6.7	1.9
1.530	-0.500	252.0	7.01	0.210	1.37	31.6	6.3	1.5
1.530	-0.167	108.0	7.02	0.208	1.38	37.4	8.5	1.8
1.530	-0.167	180.0	7.05	0.204	1.33	47.1	10.5	2.3
1.530	-0.167	252.0	7.02	0.208	1.37	28.7	7.3	1.7
1.560	-0.833	108.0	6.93	0.208	1.27	34.5	6.0	1.6
1.560	-0.833	180.0	6.94	0.207	1.26	42.4	6.0	2.1
1.560	-0.833	252.0	6.93	0.208	1.26	37.9	5.8	1.9
1.560	-0.500	108.0	6.94	0.207	1.25	35.6	6.5	1.7
1.560	-0.500	180.0	6.95	0.206	1.24	37.5	6.2	1.7
1.560	-0.500	252.0	6.94	0.208	1.22	40.9	6.6	1.9

W [GeV]	$\cos\theta_\eta^*$	ϕ_η [deg.]	$\langle Q^2_{\mathrm{bin}}\rangle$ $[\frac{\mathrm{GeV}^2}{\mathrm{c}^2}]$	$\langle\epsilon\rangle$	rad. corr.	$\frac{d^2\sigma}{d\Omega_\eta^*}$ $[\frac{n\mathrm{b}}{\mathrm{sr}}]$	δ_{stat} $[\frac{n\mathrm{b}}{\mathrm{sr}}]$	δ_{syst} $[\frac{n\mathrm{b}}{\mathrm{sr}}]$
1.560	-0.167	108.0	6.95	0.205	1.22	21.8	7.4	1.2
1.560	-0.167	180.0	6.96	0.204	1.25	33.0	10.9	2.1
1.560	-0.167	252.0	6.96	0.205	1.24	22.3	6.8	1.1
1.560	0.167	252.0	6.97	0.203	1.03	50.8	19.5	9.1
1.592	-0.833	108.0	6.85	0.207	1.18	19.3	4.5	1.3
1.592	-0.833	180.0	6.86	0.206	1.16	27.5	4.6	1.2
1.592	-0.833	252.0	6.85	0.207	1.17	20.5	4.3	0.9
1.592	-0.500	108.0	6.86	0.205	1.19	19.8	5.1	1.0
1.592	-0.500	180.0	6.87	0.204	1.19	24.1	5.1	1.2
1.592	-0.500	252.0	6.86	0.205	1.16	22.6	5.7	1.4
1.592	-0.167	108.0	6.89	0.202	1.05	29.5	10.1	1.5
1.635	-0.833	108.0	6.74	0.205	1.15	28.0	5.4	1.5
1.635	-0.833	180.0	6.75	0.203	1.15	21.8	4.3	1.1
1.635	-0.833	252.0	6.74	0.205	1.17	16.9	4.2	0.9
1.635	-0.500	108.0	6.76	0.203	1.13	16.5	5.3	0.9
1.635	-0.500	180.0	6.75	0.203	1.18	10.3	4.6	0.6
1.685	-0.833	108.0	6.60	0.203	1.26	11.8	5.6	0.7
1.685	-0.833	252.0	6.60	0.203	1.27	12.0	4.9	0.9
1.685	-0.500	180.0	6.60	0.202	1.19	15.8	4.9	0.7
1.740	-0.833	180.0	6.46	0.201	1.30	18.3	4.7	1.0

Bibliography

[1] Anthony Villano. *Neutral π electroproduction in the Δ resonance region.* PhD thesis, Rensselaer Polytechnic Institute, 2007.

[2] DOE/NSF Nuclear Science Advisory Committee. Overview of opportunities in nuclear science: A long-range plan for the next decade. Technical report, U.S. Department of Energy and National Science Foundation, June 2007.

[3] Xiangdong Ji and Zein-Eddine Meziani. APS DNP Town Meeting on Hadronic Physics, Rutgers University, January 12-14, 2007. 2007. http://www.er.doe.gov/np/nsac/docs/2007_lrpwp_hadronic.pdf.

[4] B. Krusche and S. Schadmand. Study of non-strange baryon resonances with meson photoproduction. *Prog. Part. Nucl. Phys.*, 51:399–485, 2003.

[5] V. D. Burkert and T. S. H. Lee. Electromagnetic meson production in the nucleon resonance region. *Int. J. Mod. Phys.*, E13:1035–1112, 2004.

[6] J. Ashman et al. A measurement of the spin asymmetry and determination of the structure function g(1) in deep inelastic muon proton scattering. *Phys. Lett.*, B206:364, 1988.

[7] R. G. Edwards et al. Nucleon structure in the chiral regime with domain wall fermions on an improved staggered sea. *PoS*, LAT2006:121, 2006.

[8] A. Airapetian et al. Precise determination of the spin structure function g(1) of the proton, deuteron and neutron. *Phys. Rev.*, D75:012007, 2007.

[9] A. W. Thomas. Interplay of Spin and Orbital Angular Momentum in the Proton. 2008.

[10] R. S. Towell et al. Improved measurement of the anti-d/anti-u asymmetry in the nucleon sea. *Phys. Rev.*, D64:052002, 2001.

[11] C. A. Gagliardi. Transverse spin studies with STAR at RHIC. 2006.

[12] A. Airapetian et al. Single-spin asymmetries in semi-inclusive deep-inelastic scattering on a transversely polarized hydrogen target. *Phys. Rev. Lett.*, 94:012002, 2005.

[13] Jian-wei Qiu and George Sterman. Single transverse-spin asymmetries in hadronic pion production. *Phys. Rev.*, D59:014004, 1999.

[14] Vincenzo Barone, Alessandro Drago, and Philip G. Ratcliffe. Transverse polarisation of quarks in hadrons. *Phys. Rept.*, 359:1–168, 2002.

[15] Dennis Sivers. Single-spin observables and orbital structures in hadronic distributions. *Phys. Rev.*, D74:094008, 2006.

[16] J. Collins. *Nucl. Phys.*, B396:161, 1993.

[17] Mauro Anselmino, Enrico Predazzi, Svante Ekelin, Sverker Fredriksson, and D. B. Lichtenberg. Diquarks. *Rev. Mod. Phys.*, 65:1199–1234, 1993.

[18] Simon Capstick and W. Roberts. Quark models of baryon masses and decays. *Prog. Part. Nucl. Phys.*, 45:S241–S331, 2000.

[19] R. G. Edwards et al. The nucleon axial charge in full lattice QCD. *Phys. Rev. Lett.*, 96:052001, 2006.

[20] Xiang-Dong Ji. Deeply-virtual Compton scattering. *Phys. Rev.*, D55:7114–7125, 1997.

[21] Xiang-Dong Ji. Gauge invariant decomposition of nucleon spin. *Phys. Rev. Lett.*, 78:610–613, 1997.

[22] Y. Chen et al. Glueball spectrum and matrix elements on anisotropic lattices. *Phys. Rev.*, D73:014516, 2006.

[23] S. Basak et al. Group-theoretical construction of extended baryon operators in lattice QCD. *Phys. Rev.*, D72:094506, 2005.

[24] Subhasish Basak et al. Clebsch-Gordan construction of lattice interpolating fields for excited baryons. *Phys. Rev.*, D72:074501, 2005.

[25] N. Mathur et al. Roper resonance and S(11)(1535) from lattice QCD. *Phys. Lett.*, B605:137–143, 2005.

[26] Jozef J. Dudek, Robert G. Edwards, and David G. Richards. Radiative transitions in charmonium from lattice QCD. *Phys. Rev.*, D73:074507, 2006.

[27] Jozef J. Dudek and Robert G. Edwards. Two photon decays of charmonia from lattice QCD. *Phys. Rev. Lett.*, 97:172001, 2006.

[28] S. R. Beane, P. F. Bedaque, K. Orginos, and M. J. Savage. Nucleon nucleon scattering from fully-dynamical lattice QCD. *Phys. Rev. Lett.*, 97:012001, 2006.

[29] M. Luscher. Volume Dependence of the Energy Spectrum in Massive Quantum Field Theories. 2. Scattering States. *Commun. Math. Phys.*, 105:153–188, 1986.

[30] Silas R. Beane, Paulo F. Bedaque, Kostas Orginos, and Martin J. Savage. I = 2 pi pi scattering from fully-dynamical mixed-action lattice QCD. *Phys. Rev.*, D73:054503, 2006.

[31] Silas R. Beane et al. Hyperon nucleon scattering from fully-dynamical lattice QCD. *Nucl. Phys.*, A794:62–72, 2007.

[32] John C. Collins, Leonid Frankfurt, and Mark Strikman. Factorization for hard exclusive electroproduction of mesons in QCD. *Phys. Rev.*, D56:2982–3006, 1997.

[33] A. V. Radyushkin. Scaling Limit of Deeply Virtual Compton Scattering. *Phys. Lett.*, B380:417–425, 1996.

[34] V. Frolov, J.W. Price, P. Stoler, et al. Baryon Resonance Electroproduction at High Momentum Transfer. 2001. Proposal for Jefferson Lab Experiment E01-002.

[35] Andrei V. Belitsky, Dieter Mueller, and A. Kirchner. Theory of deeply virtual Compton scattering on the nucleon. *Nucl. Phys.*, B629:323–392, 2002.

[36] B. Jager, A. Schafer, M. Stratmann, and W. Vogelsang. Next-to-leading order QCD corrections to high-p(T) pion production in longitudinally polarized p p collisions. *Phys. Rev.*, D67:054005, 2003.

[37] F. Halzen and Alan D. Martin. *QUARKS AND LEPTONS: AN INTRODUCTORY COURSE IN MODERN PARTICLE PHYSICS.* New York, USA: Wiley, 1984.

[38] M. N. Rosenbluth. High Energy Elastic Scattering of Electrons on Protons. *Phys. Rev.*, 79:615–619, 1950.

[39] R. G. Arnold et al. Measurement of Elastic electron Scattering from the Proton at High Momentum Transfer. *Phys. Rev. Lett.*, 57:174, 1986.

[40] J. Arrington, C. D. Roberts, and J. M. Zanotti. Nucleon electromagnetic form factors. *J. Phys.*, G34:S23–S52, 2007.

[41] T. Horn et al. Scaling study of the pion electroproduction cross sections and the pion form factor. 2007.

[42] T. Horn. *The pion charge form factor through pion electroproduction.* PhD thesis, University of Maryland, 2006.

[43] A. De Rujula, Howard Georgi, and S. L. Glashow. Vector Model of the Weak Interactions. *Phys. Rev.*, D12:3589, 1975.

[44] William A. Bardeen, Michael S. Chanowitz, S. D. Drell, Marvin Weinstein, and Tung-Mow Yan. Heavy Quarks and Strong Binding: A Field Theory of Hadron Structure. *Phys. Rev.*, D11:1094, 1975.

[45] Lay-Nam Chang and A. Chodos. Geometrical realization of scalar electrodynamics. *Phys. Rev.*, D9:355–364, 1974.

[46] Thomas A. DeGrand, R. L. Jaffe, K. Johnson, and J. E. Kiskis. Masses and Other Parameters of the Light Hadrons. *Phys. Rev.*, D12:2060, 1975.

[47] Thomas A. DeGrand and R. L. Jaffe. Excited States of Confined Quarks. *Ann. Phys.*, 100:425, 1976.

[48] S. Theberge, Anthony William Thomas, and Gerald A. Miller. The Cloudy Bag Model. 1. The (3,3) Resonance. *Phys. Rev.*, D22:2838, 1980.

[49] Elizabeth Ellen Jenkins. Baryon masses in chiral perturbation theory. *Nucl. Phys.*, B368:190–203, 1992.

[50] Elizabeth Ellen Jenkins. Baryon hyperfine mass splittings in large N QCD. *Phys. Lett.*, B315:441–446, 1993.

[51] F. X. Lee, D. B. Leinweber, L. Zhou, James M. Zanotti, and S. Choe. N* masses from an anisotropic lattice QCD action. *Nucl. Phys. Proc. Suppl.*, 106:248–250, 2002.

[52] Frank X. Lee and Derek B. Leinweber. Negative-parity baryon spectroscopy. *Nucl. Phys. Proc. Suppl.*, 73:258–260, 1999.

[53] Shoichi Sasaki, Tom Blum, Shigemi Ohta, and Kostas Orginos. Nucleon axial charge from quenched lattice QCD with domain wall fermions and improved gauge action. *Nucl. Phys. Proc. Suppl.*, 106:302–304, 2002.

[54] D. G. Richards. N* spectrum using an O(a)-improved fermion action. *Nucl. Phys. Proc. Suppl.*, 94:269–272, 2001.

[55] Ioana Niculescu. *Inclusive Resonance Electroproduction Data from Hydrogen and Deuterium and Studies of Quark-Hadron Duality.* PhD thesis, Hampton University, 1998.

[56] C.S. Armstrong. *Electroproduction of the* S_{11}*(1535) Resonance at High Momentum Transfer.* PhD thesis, College of William and Mary, 1998.

[57] F. W. Brasse et al. Electroproduction of η mesons in the region of the resonance $S_{11}(1535)$ at momentum transfers of 2-GeV^2 and 3-GeV^2. *Z. Phys.*, C22:33–38, 1984.

[58] Jerome I. Friedman and Henry W. Kendall. Deep inelastic electron scattering. *Ann. Rev. Nucl. Part. Sci.*, 22:203–254, 1972.

[59] G. Peter Lepage and Stanley J. Brodsky. Exclusive Processes in Perturbative Quantum Chromodynamics. *Phys. Rev.*, D22:2157, 1980.

[60] Carl E. Carlson and J. L. Poor. Distribution amplitudes and electroproduction of the delta and other low lying resonances. *Phys. Rev.*, D38:2758, 1988.

[61] P. Stoler. Form-factors of excited baryons at high Q^2 and the transition to perturbative QCD. 2. *Phys. Rev.*, D44:73–80, 1991.

[62] Carl E. Carlson. Electromagnetic N - delta transition at high Q^2. *Phys. Rev.*, D34:2704, 1986.

[63] C. S. Armstrong, P. Stoler, et al. Electroproduction of the $S_{11}(1535)$ resonance at high momentum transfer. *Phys. Rev.*, D60(5):052004–+, September 1999.

[64] P. Stoler. Form-factors of excited baryons at high Q^2 and the transition to perturbative QCD. *Phys. Rev. Lett.*, 66:1003–1006, 1991.

[65] Simon Capstick and B. D. Keister. Baryon current matrix elements in a light front framework. *Phys. Rev.*, D51:3598–3612, 1995.

[66] I. G. Aznauryan. Electroexcitation of the Roper resonance in the relativistic quark models. *Phys. Rev.*, C76:025212, 2007.

[67] I. G. Aznauryan, V. D. Burkert, G. V. Fedotov, B. S. Ishkhanov, and V. I. Mokeev. Electroexcitation of nucleon resonances at $Q^2 = 0.65$ (GeV/c)^2 from a combined analysis of single- and double- pion electroproduction data. *Phys. Rev.*, C72:045201, 2005.

[68] I. G. Aznauryan et al. Electroexcitation of the P33(1232), P11(1440), D13(1520), S11(1535) at $Q^2 = 0.4$ (GeV/c)^2 and 0.65 (GeV/c)^2. *Phys. Rev.*, C71:015201, 2005.

[69] K. Park et al. Cross sections and beam asymmetries for $ep \rightarrow en\pi^+$ in the nucleon resonance region for $1.7 \leq Q^2 \leq 4.5(GeV)^2$. *Phys. Rev.*, C77:015208, 2008.

[70] W. M. Yao et al. Review of particle physics. *J. Phys.*, G33:1–1232, 2006.

[71] F. W. Brasse et al. Separation of σ_L and σ_T in η - electroproduction at the resonance $S_{11}(1535)$. *Nucl. Phys.*, B139:37, 1978.

[72] H. Denizli et al. Q^2 dependence of the $S_{11}(1535)$ photocoupling and evidence for a P-wave resonance in η electroproduction. *Phys. Rev.*, C76:015204, 2007.

[73] P. S. Kummer et al. Measurement of the electromagnetic-transition form-factor for the $S_{11}(1535)$ resonance. *Phys. Rev. Lett.*, 30:873–875, 1973.

[74] U. Beck et al. Electroproduction of eta-mesons at the s(11)(1535) resonance. *Phys. Lett.*, B51:103–105, 1974.

[75] J. C. Alder et al. Electroproduction of eta Mesons in the Region of the Resonance S11 (1535). *Nucl. Phys.*, B91:386, 1975.

[76] L. N. Hand. Experimental investigation of pion electroproduction. *Phys. Rev.*, 129:1834–1846, 1963.

[77] R. L. Walker. Phenomenological analysis of single pion photoproduction. *Phys. Rev.*, 182:1729–1748, 1969.

[78] M. Warns, H. Schroder, W. Pfeil, and H. Rollnik. Calculations of electromagnetic nucleon form-factors and electroexcitation amplitudes of isobars. *Z. Phys.*, C45:627, 1990.

[79] G. Knochlein, D. Drechsel, and L. Tiator. Photoproduction and electroproduction of η mesons. *Z. Phys.*, A352:327–343, 1995.

[80] D. Drechsel and L. Tiator. Threshold pion photoproduction on nucleons. *J. Phys.*, G18:449–497, 1992.

[81] Particle Data Group. Positron-proton scattering. *Rev. Mod. Phys.*, 48:S157, 1976.

[82] B. Krusche et al. Near Threshold Photoproduction of η Mesons off the Proton. *Phys. Rev. Lett.*, 74:3736–3739, May 1995.

[83] H. Breuker et al. Determination of $r = \sigma_L/\sigma_T$ from η electroproduction at the $S_{11}(1535)$ resonance. *Phys. Lett.*, B74:409–412, 1978.

[84] Richard Matthew Mohring. *A Comparison of longitudinal and transverse cross-sections in the $p(e, e\ K+)\Lambda$ and $p(e, e'K+)\Sigma^0$ reactions.* PhD thesis, University of Maryland, 1999. UMI-99-57190.

[85] John Robert Arrington. *Inclusive electron scattering from nuclei at $x > 1$ and high Q^2.* PhD thesis, California Institute of Technology, 1998.

[86] C. W. Leemann, D. R. Douglas, and G. A. Krafft. The Continuous Electron Beam Accelerator Facility: CEBAF at the Jefferson Laboratory. *Ann. Rev. Nucl. Part. Sci.*, 51:413–450, 2001.

[87] H.P. Blok et al. *in preparation for Phys.Rev.C*, 2008.

[88] J. Arrington. *Hall C in house publication,*, A-B-SIMC, 2001.

[89] K. Makino and M. Berz. COSY INFINITY Version 9. *Nucl. Instrum. Meth.*, A558:346–350, 2006.

[90] M. E. Christy and P. B. Bosted. Empirical fit to precision inclusive electron-proton cross sections in the resonance region. 2007.

[91] P. Corvisiero et al. Simulation of photon nucleon interactions. 1: An event generator from the pion threshold up to 4-GeV. *Nucl. Instrum. Meth.*, A346:433–440, 1994.

[92] V. I. Mokeev et al. Phenomenological model for describing pion pair production on a proton by virtual photons in the energy region of nucleon resonance excitation. *Phys. Atom. Nucl.*, 64:1292–1298, 2001.

[93] M. Ripani et al. Measurement of $ep \to e^{'} p \pi^+ \pi^-$ and baryon resonance analysis. *Phys. Rev. Lett.*, 91(2):022002, Jul 2003.

[94] F. James and M. Roos. Minuit: A system for function minimization and analysis of the parameter errors and correlations. *Comput. Phys. Commun.*, 10:343–367, 1975.

[95] R. Ent et al. Radiative corrections for $(e, e'p)$ reactions at GeV energies. *Phys. Rev.*, C64:054610, 2001.

[96] Peter E. Bosted. An empirical fit to the nucleon electromagnetic formfactors. *Phys. Rev.*, C51:409–411, 1995.

[97] S. Malace. *Measurements of inclusive resonance cross sections for quark-hadron duality studies.* PhD thesis, Hampton University, 2006.

[98] Luke W. Mo and Yung-Su Tsai. Radiative corrections to elastic and inelastic ep and μp scattering. *Rev. Mod. Phys.*, 41:205–235, 1969.

[99] M. E. Christy et al. Measurements of electron proton elastic cross sections for 0.4 $(\mathrm{GeV/c})^2 < Q^2 < 5.5$ $(\mathrm{GeV/c})^2$. *Phys. Rev.*, C70:015206, 2004.

[100] Wen-Tai Chiang, Shin-Nan Yang, Lothar Tiator, and Dieter Drechsel. An isobar model for eta photo- and electroproduction on the nucleon. *Nucl. Phys.*, A700:429–453, 2002.

[101] F. Renard et al. Differential cross-section measurement of η photoproduction on the proton from threshold to 1100-MeV. *Phys. Lett.*, B528:215–220, 2002.

[102] M. Aiello, M. M. Giannini, and E. Santopinto. Electromagnetic transition form factors of negative parity nucleon resonances. *J. Phys.*, G24:753–762, 1998.

[103] Zhen-ping Li and Frank E. Close. QCD mixing effects in a gauge invariant quark model for photoproduction and electroproduction of baryon resonances. *Phys. Rev.*, D42:2207–2214, 1990.

[104] W. Konen and H. J. Weber. Electromagnetic N $\rightarrow$ N* (1535) transition in the relativistic constituent quark model. *Phys. Rev.*, D41:2201, 1990.

[105] E. Pace, G. Salme, and S. Simula. Investigation of N-N* electromagnetic form factors within a front-form CQM. *Few Body Syst. Suppl.*, 10:407–410, 1999.

[106] A. V. Radyushkin. Exclusive processes in perturbative QCD. *Nucl. Phys.*, A527:153c–163c, 1991.

[107] Nathan Isgur and C. H. Llewellyn Smith. Asymptopia in high Q^2 exclusive processes in QCD. *Phys. Rev. Lett.*, 52:1080, 1984.

[108] D. Drechsel, O. Hanstein, S. S. Kamalov, and L. Tiator. A unitary isobar model for pion photo- and electroproduction on the proton up to 1-GeV. *Nucl. Phys.*, A645:145–174, 1999.

[109] F. X. Lee, T. Mart, C. Bennhold, and L. E. Wright. Quasifree kaon photoproduction on nuclei. *Nucl. Phys.*, A695:237–272, 2001.

[110] C. Bennhold, H. Haberzettl, and T. Mart. A new resonance in K+ Lambda electroproduction: The D(13)(1895) and its electromagnetic form factors. 1999.

[111] A. Fix and H. Arenhovel. Double pion photoproduction on nucleon and deuteron. *Eur. Phys. J.*, A25:115–135, 2005.

[112] Wen-Tai Chiang, Shin Nan Yang, L. Tiator, M. Vanderhaeghen, and D. Drechsel. A reggeized model for eta and eta' photoproduction. *Phys. Rev.*, C68:045202, 2003.

[113] Jefferson Lab Theory Centre. http://ebac-theory.jlab.org/.

[114] J.R. Arrington et al. Jefferson Lab 12 GeV Upgrade Hall-C Conceptual Design Report. 2005. http://www.jlab.org/Hall-C/upgrade/cdr.pdf.

[115] Y. Liang et al. Measurement of R = sigma(L)/sigma(T) and the separated longitudinal and transverse structure functions in the nucleon resonance region. 2004.

[116] Guido Altarelli and G. Martinelli. Transverse Momentum of Jets in Electroproduction from Quantum Chromodynamics. *Phys. Lett.*, B76:89, 1978.

[117] R. Keith Ellis, W. Furmanski, and R. Petronzio. Power Corrections to the Parton Model in QCD. *Nucl. Phys.*, B207:1, 1982.

[118] R. Keith Ellis, W. Furmanski, and R. Petronzio. Unraveling Higher Twists. *Nucl. Phys.*, B212:29, 1983.